

Medical Image Registration and 3D Object Matching



Waleed Mohamed

A Thesis
in
The Department
of
Electrical and Computer Engineering
Concordia University

Presented in Partial Fulfillment of the Requirements
for the Degree of Doctor of Philosophy at
Concordia University
Montréal, Québec, Canada

March 2012



© Waleed Mohamed, 2012

CONCORDIA UNIVERSITY
SCHOOL OF GRADUATE STUDIES

This is to certify that the thesis prepared

By: Waleed Mohamed

Entitled: Medical Image Registration and 3D Object Matching

and submitted in partial fulfillment of the requirements for the degree of

DOCTOR OF PHILOSOPHY (Electrical & Computer Engineering)

complies with the regulations of the University and meets the accepted standards with respect to originality and quality.

Signed by the final examining committee:

_____ Chair
Dr. L. Kadem

_____ External Examiner
Dr. E. Paquette

_____ External to Program
Dr. S. Narayanswamy

_____ Examiner
Dr. N. Bouguila

_____ Examiner
Dr. Y. Zeng

_____ Supervisor
Dr. A. Ben Hamza

Approved by _____
Dr. J.X. Zhang, Graduate Program Director

March 20, 2012

Dr. Robin A.L. Drew, Dean
Faculty of Engineering & Computer Science

ABSTRACT

Medical Image Registration and 3D Object Matching

Waleed Mohamed

The great challenge in image registration and 3D object matching is to devise computationally efficient algorithms for aligning images so that their details overlap accurately and retrieving similar shapes from large databases of 3D models. The first problem addressed in this thesis is medical image registration, which we formulate as an optimization problem in the information-theoretic framework. We introduce a viable and practical image registration method by maximizing an entropic divergence measure using a modified simultaneous perturbation stochastic approximation algorithm. The feasibility of the proposed image registration approach is demonstrated through extensive experiments.

The rest of the thesis is devoted to a joint exploitation of geometry and topology of 3D objects for as parsimonious as possible representation of models and its subsequent application in 3D object representation, matching, and retrieval problems. More precisely, we introduce a skeletal graph for topological 3D shape representation using Morse theory. The proposed skeletonization algorithm encodes a 3D shape into a topological Reeb graph using a normalized mixture distance function. We also propose a novel graph matching algorithm by comparing the relative shortest paths between the skeleton endpoints. Moreover, we describe a skeletal graph for 3D object matching and retrieval. This skeleton is constructed from the second eigenfunction of the Laplace-Beltrami operator defined on the surface of the 3D object. Using the generalized eigenvalue decomposition, a matrix computational framework based on the finite element method is presented to compute the spectrum of the Laplace-Beltrami operator. Illustrating experiments on two standard 3D shape benchmarks are provided to demonstrate the feasibility and the much improved performance of the proposed skeletal graphs as shape descriptors for 3D object matching and retrieval.

TABLE OF CONTENTS

TITLE PAGE	i
TABLE OF CONTENTS	iv
LIST OF TABLES	vii
LIST OF FIGURES	viii

— CHAPTER —

INTRODUCTION	1
1.1 FRAMEWORK AND MOTIVATION	1
1.2 PROBLEM STATEMENT	2
1.2.1 IMAGE REGISTRATION	2
1.2.2 3D OBJECT MATCHING	3
1.3 OBJECTIVES	5
1.4 BACKGROUND	5
1.5 MORSE THEORY FOR TOPOLOGICAL MODELING	5
1.6 THESIS OVERVIEW	9

— CHAPTER —

IMAGE REGISTRATION USING STOCHASTIC OPTIMIZATION	10
2.1 INTRODUCTION	10
2.2 PROBLEM FORMULATION	11
2.2.1 JENSEN-TSALLIS DIVERGENCE	12

2.2.2	PROPERTIES OF THE JENSEN-TSALLIS DIVERGENCE	15
2.2.3	MODIFIED SPSA OPTIMIZATION ALGORITHM	16
2.3	PROPOSED METHOD	17
2.4	EXPERIMENTAL RESULTS	18
2.4.1	EFFECT OF WEIGHT ON THE JENSEN-TSALLIS DIVERGENCE	20
2.4.2	EFFECT OF α ON THE JENSEN-TSALLIS DIVERGENCE	21

— CHAPTER —

	REEB GRAPH PATH DISSIMILARITY FOR 3D OBJECT MATCHING AND RETRIEVAL	29
3.1	INTRODUCTION	29
3.2	PROPOSED REEB GRAPH APPROACH	32
3.2.1	MIXTURE DISTANCE FUNCTION	34
3.2.2	MORSE-THEORETIC ANALYSIS OF THE MIXTURE DISTANCE FUNCTION	34
3.2.3	PROPERTIES OF THE MIXTURE DISTANCE FUNCTION	35
3.2.4	NORMALIZED MIXTURE DISTANCE FUNCTION	36
3.2.5	PROPOSED SKELETONIZATION ALGORITHM	36
3.3	REEB GRAPH MATCHING	37
3.3.1	INDEXING	40
3.3.2	ENDPOINTS CORRESPONDENCE	41
3.3.3	MATCHING ENDPOINTS USING SKELETON PATHS	41
3.4	EXPERIMENTAL RESULTS	44
3.4.1	ROBUSTNESS TO NOISE	45
3.4.2	ROBUSTNESS TO MESH DECIMATION	46
3.4.3	INVARIANCE TO ROTATION, TRANSLATION, AND SCALING	47
3.4.4	MATCHING AND RETRIEVAL RESULTS	47

— CHAPTER —

	SPECTRAL SKELETON FOR 3D OBJECT MATCHING AND RETRIEVAL	53
4.1	INTRODUCTION	53
4.2	SPECTRAL REEB GRAPH	57
4.2.1	LAPLACE-BELTRAMI OPERATOR	57
4.2.2	DISCRETIZATION USING FINITE ELEMENT METHOD	59

4.2.3	SPECTRAL SKELETON	60
4.3	SPECTRAL REEB GRAPH MATCHING	62
4.4	EXPERIMENTAL RESULTS	65

— CHAPTER —

CONCLUSIONS AND FUTURE WORK		72
5.1	THESIS CONTRIBUTIONS	72
5.1.1	IMAGE REGISTRATION USING STOCHASTIC OPTIMIZATION	72
5.1.2	REEB GRAPH PATH DISSIMILARITY FOR 3D OBJECT MATCHING AND RETRIEVAL	73
5.1.3	SPECTRAL SKELETON FOR 3D OBJECT MATCHING AND RETRIEVAL	73
5.2	FUTURE RESEARCH DIRECTIONS	73
5.2.1	3D PARTIAL SHAPE MATCHING	73
5.2.2	STOCHASTIC ANALYSIS OF LAPLACE-BELTRAMI SPECTRA	73
5.2.3	IMAGE REGISTRATION USING PRIORS	74
REFERENCES		75

LIST OF TABLES

3.1	Matching results using proposed Reeb graph path dissimilarity (RGPD). Each object in the database is matched against all the other objects in the database. Each cell shows the dissimilarity measure between two objects selected from the database. The smallest value corresponds to the correct match.	50
3.2	Retrieval results using the McGill Shape Benchmark. The query shapes are shown in the second row. The top ten retrieved objects (top-to-bottom) using spherical harmonics (SH) and our proposed Reeb graph path dissimilarity (RGPD) are shown in rows 5 to 14.	51
3.3	Retrieval results using the Princeton Shape Benchmark. The query shapes are shown in the second row. The top five retrieved objects (top-to-bottom) using spherical harmonics (SH) and our proposed Reeb graph path dissimilarity (RGPD) are shown in rows 5 to 9.	52
4.1	Matching results using proposed approach. Each database object is matched against all the other objects in the database. Each cell shows the dissimilarity measure between two objects selected from the database. The smallest value corresponds to the correct match.	66
4.2	Retrieval results using the McGill Shape Benchmark. The query shapes are shown in the second row. The top ten retrieved objects (top-to-bottom) using spherical harmonics (SH), Reeb graph path dissimilarity (RGPD), and our proposed approach (SRG) are shown in rows 5 to 14.	70
4.3	Retrieval results using Princeton 3D dataset Benchmark. The query shapes are shown in the second row. The top five retrieved objects (top-to-bottom) of our proposed approach (SRG).	71

LIST OF FIGURES

1.1 (A) REFERENCE IMAGE I ; (B) TARGET IMAGE J	3
1.2 3D OBJECT MATCHING DIAGRAM.	4
1.3 ILLUSTRATION OF THE 3D MATCHING PROBLEM.	4
1.4 ILLUSTRATION OF A VERTEX NEIGHBORHOOD \mathbf{p}_i^*	6
1.5 NONDEGENERATE SINGULAR POINTS OF A MORSE HEIGHT FUNCTION: MINIMUM (BLUE), SADDLE (GREEN), MAXIMUM (RED).	6
1.6 ILLUSTRATION OF THE TANGENT SPACE.	7
1.7 ILLUSTRATION OF: (A) LEVEL CURVE L_a , (B) SUBSURFACE \mathbb{M}_a , (C) SUBSURFACE AND LEVEL CURVE.	7
1.8 EVOLUTION OF \mathbb{M}_a AS a CHANGES.	8
1.9 REEB GRAPH REPRESENTATION	8
2.1 (A) REFERENCE IMAGE I_1 . (B) TARGET IMAGE I_2	12
2.2 TSALLIS ENTROPY $H_\alpha(\mathbf{p})$ OF A BERNOULLI DISTRIBUTION $\mathbf{p} = (p, 1 - p)$ FOR DIFFERENT VALUES OF α	14
2.3 SURFACE/CONTOUR PLOTS OF JENSEN-TSALLIS DIVERGENCE BETWEEN TWO BERNOULLI DISTRIBUTIONS $\mathbf{p} = (p, 1 - p)$ AND $\mathbf{q} = (q, 1 - q)$, AND WITH EQUAL WEIGHTS $\omega_1 = \omega_2 =$ $1/2$. FIRST ROW: $\alpha = 0.3$. SECOND ROW: $\alpha = 1.2$	15
2.4 3D PLOTS OF CONDITIONAL PROBABILITY DISTRIBUTIONS FOR DIFFERENT TRANSFORMA- TION VECTORS.	18
2.5 CONDITIONAL PROBABILITY DISTRIBUTIONS.	19

2.6	BAR PLOTS OF OPTIMAL REGISTRATION PARAMETER VECTOR $\ell^* = (t_x^*, t_y^*, \theta^*)$ WITH ERRORS $\ell - \ell^*$, USING (A) PROPOSED METHOD, (B) JENSEN-RÉNYI DIVERGENCE, (C) MUTUAL INFORMATION, AND (D) TSALLIS MUTUAL INFORMATION.	20
2.7	BAR PLOTS OF OPTIMAL REGISTRATION PARAMETER VECTOR $\ell^* = (t_x^*, t_y^*, \theta^*)$ WITH ERRORS $\ell - \ell^*$, USING (A) PROPOSED METHOD, (B) JENSEN-RÉNYI DIVERGENCE, (C) MUTUAL INFORMATION, AND (D) TSALLIS MUTUAL INFORMATION.	21
2.8	BAR PLOTS OF OPTIMAL REGISTRATION PARAMETER VECTOR $\ell^* = (t_x^*, t_y^*, \theta^*)$ WITH ERRORS $\ell - \ell^*$, USING (A) PROPOSED METHOD, (B) JENSEN-RÉNYI DIVERGENCE, (C) MUTUAL INFORMATION, AND (D) TSALLIS MUTUAL INFORMATION.	22
2.9	JENSEN-TSALLIS DIVERGENCE WITH UNIFORM WEIGHT.	23
2.10	JENSEN-RÉNYI DIVERGENCE WITH UNIFORM WEIGHT.	24
2.11	JENSEN-TSALLIS DIVERGENCE WITH NORMALIZED HISTOGRAM WEIGHT.	25
2.12	JENSEN-RÉNYI DIVERGENCE WITH NORMALIZED HISTOGRAM WEIGHT.	26
2.13	(A) MRI 3D VOLUME. (B) REFERENCE AND TARGET IMAGES FOR TESTING THE EFFECT OF THE ENTROPIC INDEX.	27
2.14	DIVERGENCE VALUES WITH UNIFORM WEIGHT ω_j	27
2.15	DIVERGENCE VALUES WITH NORMALIZED HISTOGRAM WEIGHT ω_j	28
3.1	LEVEL SETS OF THE (A) EUCLIDEAN AND (B) AFFINE INVARIANT DISTANCES.	34
3.2	MIXTURE DISTANCE-BASED REEB GRAPH EXTRACTION AT VARIOUS STEPS $k = 1, \dots, 13$	38
3.3	(A) CONNECTED COMPONENTS AND (B) SKELETAL GRAPH OF A DOUBLE TORUS.	39
3.4	THE 3D COW'S REEB GRAPH AND ITS SKELETON ENDPOINTS (RED COLOR).	39
3.5	(A) CAMEL'S REEB GRAPH. (B) SHORTEST PATHS BETWEEN PAIRS OF ENDPOINTS ON THE SKELETON.	42
3.6	SHORTEST PATHS BETWEEN THE MESH CENTROID AND AN ENDPOINT ON THE SKELETON.	43
3.7	SKELETAL GRAPHS USING AFFINE AND MIXTURE DISTANCE FUNCTIONS.	45
3.8	MIXTURE DISTANCE-BASED REEB GRAPHS OF DIFFERENT 3D MODELS.	46
3.9	(A) NOISY DOUBLE TORUS AND ITS (B) MIXTURE DISTANCE-BASED REEB GRAPH.	46
3.10	MIXTURE DISTANCE-BASED REEB GRAPH UNDER MESH DECIMATION.	47
3.11	ILLUSTRATION OF SKELETAL REEB GRAPH INVARIANCE TO ROTATION AND SCALING.	48

3.12	SAMPLE SHAPES FROM MCGILL ARTICULATED SHAPE DATABASE. ONLY TWO SHAPES FOR EACH OF THE 10 CLASSES ARE SHOWN.	48
3.13	PRECISION VS. RECALL CURVES FOR SPHERICAL HARMONICS (SH), MEDIAL SURFACES (MS), AND PROPOSED RGPD APPROACH USING THE MCGILL SHAPE BENCHMARK [71].	49
4.1	ILLUSTRATION OF A VERTEX NEIGHBORHOOD v_i^*	59
4.2	ILLUSTRATION OF $\text{area}(t)$ AND $n(t)$	60
4.3	(A) 3D TOOTH MODEL; (B) SPARSITY PATTERN PLOT OF THE COTANGENT MATRIX Q ; (C) SPARSITY PATTERN PLOT OF THE AREA MATRIX K	61
4.4	(A) 3D TOOTH MODEL COLORED BY φ_1 ; (B) TOOTH MODEL COLORED BY φ_2 ; (C) LEVEL SETS OF φ_2	62
4.5	(A) 3D HORSE MODEL COLORED BY φ_2 ; (B) LEVEL SETS OF φ_2 ; (C) SPECTRAL REEB GRAPH.	63
4.6	SPECTRAL REEB GRAPH OF 3D OCTOPUS MODEL AND ITS SKELETON ENDPOINTS SHOWN IN BLUE COLOR.	64
4.7	(A) HORSE'S REEB GRAPH. (B) SHORTEST PATHS BETWEEN PAIRS OF ENDPOINTS ON THE SPECTRAL SKELETON.	67
4.8	SHORTEST PATHS BETWEEN THE MESH CENTROID AND AN ENDPOINT ON THE SPECTRAL SKELETON.	68
4.9	ROBUSTNESS OF SPECTRAL REEB GRAPH TO NOISE.	69
4.10	PRECISION VS. RECALL CURVES FOR REEB GRAPH PATH DISSIMILARITY, SPHERICAL HARMONICS, MEDIAL SURFACES, REEB GRAPH PATH DISSIMILARITY, AND PROPOSED APPROACH USING THE MCGILL SHAPE BENCHMARK [71].	69

LIST OF ACRONYMS

SH Spherical Harmonics

MS Medial Surfaces

RGPD Reeb Graph Path Dissimilarity

SRG Spectral Reeb Graph

INTRODUCTION

In this Chapter, we present the framework and motivation behind this work, followed by the problem statement, objectives, and a brief overview of essential concepts and definitions which we will refer to throughout the thesis. We also present a short summary of background material relevant to 3D object matching in the topological framework.

1.1 FRAMEWORK AND MOTIVATION

Recent advances in medical imaging have resulted in the development of many imaging techniques that capture various aspects of the patient's anatomy and metabolism [1, 2]. Image registration is among the most challenging problems in medical imaging, and it is of paramount importance in medical diagnosis and computer aided surgery [1, 2]. Image registration or alignment refers to the process of aligning two or more images of the same scene so that their details overlap accurately [1, 2, 3]. Typically, one image, called the fixed or reference image, is considered the reference to which the other images, called moving or target images, are compared. A wide range of image registration techniques have been recently developed for many different types of applications and data, such as mean squared alignment, correlation registration, moment invariant matching, and entropic alignment [1, 2, 3]. The latter problem will be the primary focus in Chapter 2. Our focus on the entropic approach is inspired by the successful application of the mutual information measure to medical image registration [2].

In the same vein, recent technological advancements in computing power and capability coupled with the availability of freely-distributed 3D databases on the Internet have led to a flurry of research activity in the area of 3D object recognition. The importance of 3D shape recognition is irrupting due to the difficulty in

processing information expeditiously without its recognition. With the increasing use of 3D scanners and as a result of emerging multimedia computing technologies, vast databases of 3D models are distributed freely or commercially on the World Wide Web. The availability and widespread usage of such large databases coupled with the need to explore 3D models in depth as well as in breadth has sparked the need to organize and search these vast data collections, retrieve the most relevant selections, and permit them to be effectively reused. 3D objects consist of geometric and topological information, and their compact representation is an important step towards a variety of computer vision applications, particularly matching and retrieval in a database of 3D models. The first step in 3D object matching usually involves finding a reliable shape descriptor or skeletal graph which will encode efficiently the 3D shape information. The skeleton-based approach for 3D object matching and retrieval will be the focus of the thesis in Chapters 3 and 4.

1.2 PROBLEM STATEMENT

1.2.1 IMAGE REGISTRATION

Image registration is of paramount importance in the field of medical imaging and has sparked a flurry of research interest in many other applications of image analysis such as remote sensing, movie editing, and archeology. The objective of image registration is to bring the target image into alignment with the reference image by applying a spatial transformation to the target image. Images are usually registered for the purpose of combining or comparing them, enabling the fusion of information in the images. Roughly speaking, the image alignment problem may be formulated as a two-step process: the first step is to define a distance measure that quantifies the quality of spatial alignment between the reference image and the spatially transformed target image, and the second step is to develop an efficient optimization algorithm for optimizing this distance measure iteratively in order to find the optimal transformation parameters.

More precisely, given two misaligned images, the reference image I and the target image J as depicted in Figure 1.1, the image alignment or registration problem may be formulated as an optimization problem

$$\ell^* = \arg \max_{\ell} D(I(\mathbf{x}), J(\Phi_{\ell}(\mathbf{x}))), \quad (1.1)$$

where $D(\cdot, \cdot)$ is a dissimilarity measure that quantifies the discrepancy between the reference image and the transformed target image; and $\Phi_{\ell} : \Omega \leftarrow \Omega$ is a spatial transformation mapping parameterized by a parameter vector ℓ .

The goal of image registration is to align the target image to the reference image by maximizing the dissimilarity measure $D(I(\mathbf{x}), J(\Phi_{\ell}(\mathbf{x})))$ using an optimization scheme in order to find the optimal spatial

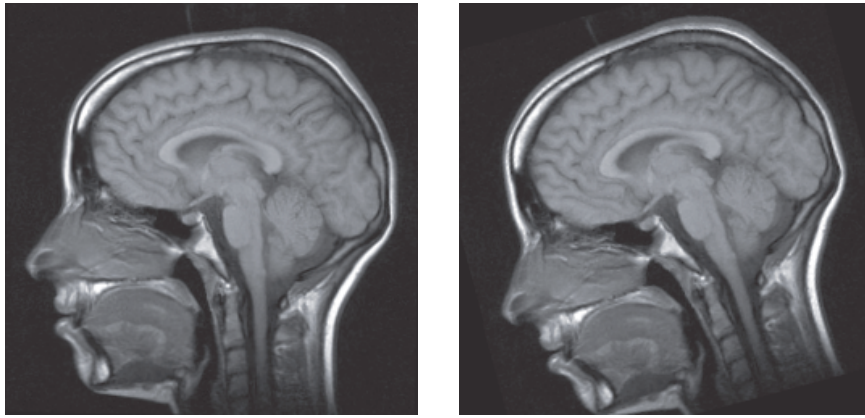


FIGURE 1.1: (a) Reference image I ; (b) Target image J .

transformation parameters. Note that since the image pixel values are integers, a bilinear interpolation may be used to determine the values of $J(\Phi_{\ell}(x))$ when $\Phi_{\ell}(x)$ is not an integer.

1.2.2 3D OBJECT MATCHING

In recent years, the 3D object recognition problem has become very important in the field of computer graphics, computer vision and many related application areas due to the difficulty in processing information efficiently without its recognition. There are two major techniques for 3D object recognition: feature-based and global methods as illustrated in Figure 1.2. Most 3D shape matching techniques proposed in the literature of computer graphics, computer vision and computer-aided design are based on geometric representations which represent the features of an object in such a way that the shape dissimilarity problem reduces to the problem of comparing two such object representations. Feature-based methods require that features be extracted and described before two objects can be compared. An alternative to feature-based representations is global methods. The idea here is to represent an object by a global measure or shape distribution defined on the surface of the object. The shape matching problem is then performed by computing a dissimilarity measure between the shape distributions of two arbitrary objects.

The goal of 3D object matching may be described as follows: Given two 3D objects \mathbb{M}_1 and \mathbb{M}_2 to be matched, find their respective global measures or shape descriptors \hat{p}_1 and \hat{p}_2 , and calculate how dissimilar these objects are using a dissimilarity measure $D(\hat{p}_1, \hat{p}_2)$ that has to be quantified. The basic idea behind the shape descriptor is to characterize a 3D object with a skeleton graph that will help discriminate between objects in a database of 3D models. The 3D object matching problem is depicted in Figure 1.3.

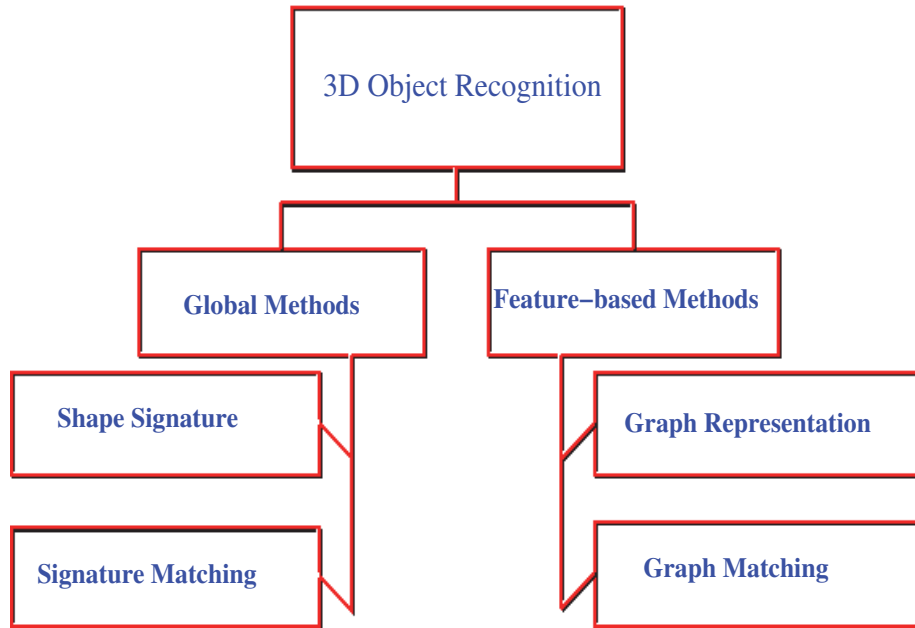


FIGURE 1.2: 3D object matching diagram.

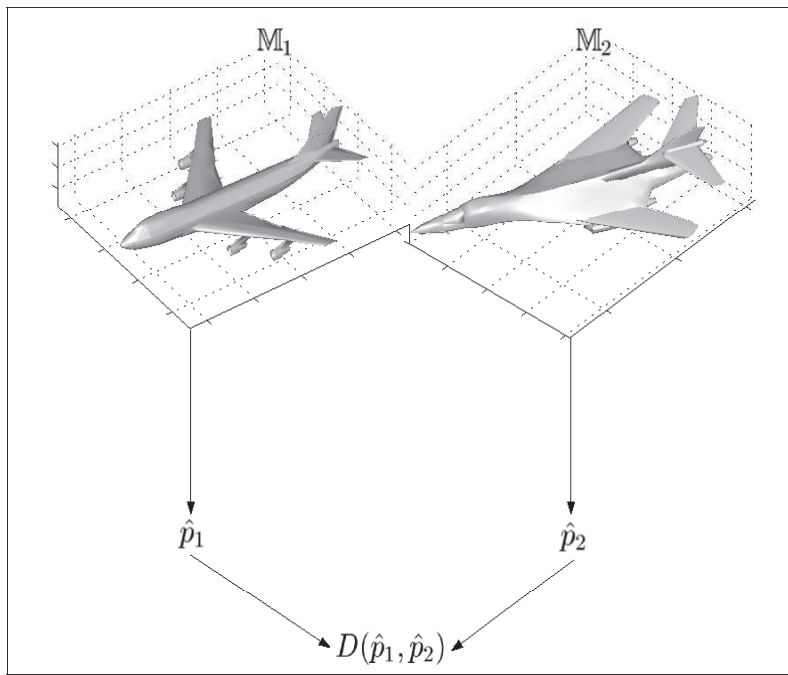


FIGURE 1.3: Illustration of the 3D matching problem.

1.3 OBJECTIVES

Our main objectives may be summarized as follows:

- Develop an efficient image registration algorithm for aligning medical images so that their details overlap accurately, and perform an experimental comparative study with the state-of-the-art registration techniques.
- Develop a novel skeletal graph for topological 3D shape recognition using Morse theory, and devise an efficient graph matching algorithm.
- Construct a spectral skeleton from the second eigenfunction of the Laplace-Beltrami operator defined on the surface of the 3D object, and design a practical 3D object matching and retrieval technique.

1.4 BACKGROUND

In computer graphics and geometric-aided design, 3D objects are usually represented as polygonal or triangle meshes. A triangle mesh \mathbb{M} is usually denoted by $\mathbb{M} = (\mathcal{V}, \mathcal{T})$, where $\mathcal{V} = \{\mathbf{p}_1, \dots, \mathbf{p}_m\}$ is the set of vertices and $\mathcal{T} = \{\mathbf{t}_1, \dots, \mathbf{t}_n\}$ is the set of triangles. Two distinct vertices $\mathbf{p}_i, \mathbf{p}_j \in \mathcal{V}$ are adjacent (denoted by $\mathbf{p}_i \bowtie \mathbf{p}_j$) if they are connected by an edge. The neighborhood of a vertex \mathbf{p}_i is the set $\mathbf{p}_i^* = \{\mathbf{p}_j \in \mathcal{V} : \mathbf{p}_i \bowtie \mathbf{p}_j\}$ as shown in Figure 1.4. We define the area of a vertex \mathbf{p}_i as $area(\mathbf{p}_i) = \sum_{\mathbf{t}_j \in \mathcal{T}(\mathbf{p}_i^*)} area(\mathbf{t}_j)$, where $\mathcal{T}(\mathbf{p}_i^*)$ is the set of triangles of the vertex neighborhood. Consider a triangle \mathbf{t}_j with sides of lengths a, b and c . Then, according to Heron's formula, $area(\mathbf{t}_j)$ is equal to

$$\frac{1}{4} \sqrt{(a + (b + c))(a + (b - c))(c + (a - b))(c - (a - b))}, \quad (1.2)$$

where these lengths are arranged such that $a \geq b \geq c$.

The following section briefly describes the basic concepts of Morse theory, followed by a short description of the Reeb graph representation for 3D topological modeling.

1.5 MORSE THEORY FOR TOPOLOGICAL MODELING

Morse theory explains the presence and the stability of singular points in terms of the topology of the underlying smooth manifold. Topology is the study of the “shape” of curves and surfaces [4], while geometry determines where, in a given coordinate system, each part is located [5]. The basic principle is that the

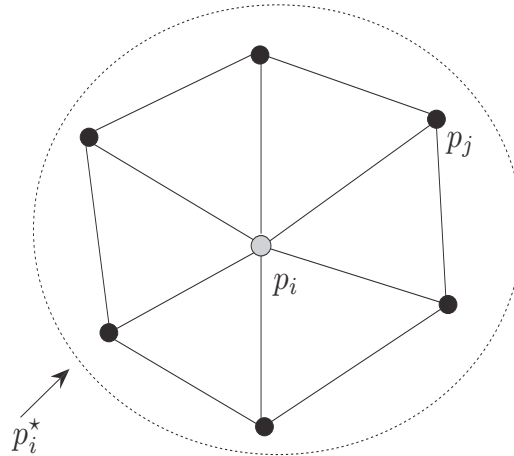


FIGURE 1.4: Illustration of a vertex neighborhood p_i^* .

topology of a manifold is very closely related to the singular points of a smooth function defined on that manifold [6]. A smooth function $f : \mathbb{M} \rightarrow \mathbb{R}$ on a smooth manifold \mathbb{M} is called a *Morse function* if all its singular points are nondegenerate, i.e. the Hessian matrix is nonsingular at every singular point. The only nondegenerate singularities are the minimum, maximum and saddle points as depicted in Figure 1.5.

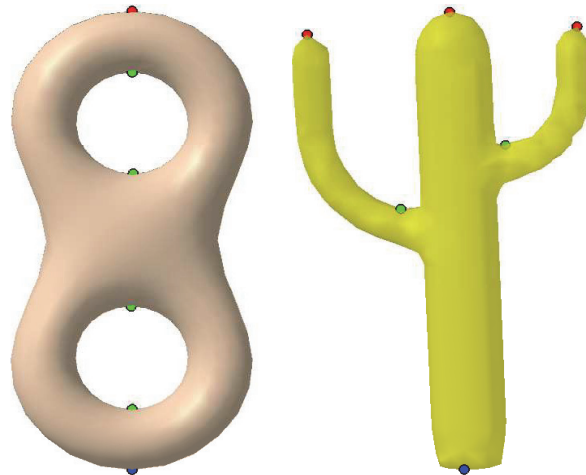


FIGURE 1.5: Nondegenerate singular points of a Morse height function: minimum (blue), saddle (green), maximum (red).

A point p is called a *regular point* of f if the differential $df : T_p\mathbb{M} \rightarrow \mathbb{R}$ is *surjective*, that is, the Jacobian matrix (3×1 in the case of a 2-manifold) has rank equal to $\dim(\mathbb{R}) = 1$, where $T_p\mathbb{M}$ is the tangent plane to \mathbb{M} at p as shown in Figure 1.6. Otherwise, the point p is called a *critical point*. Nondegenerate

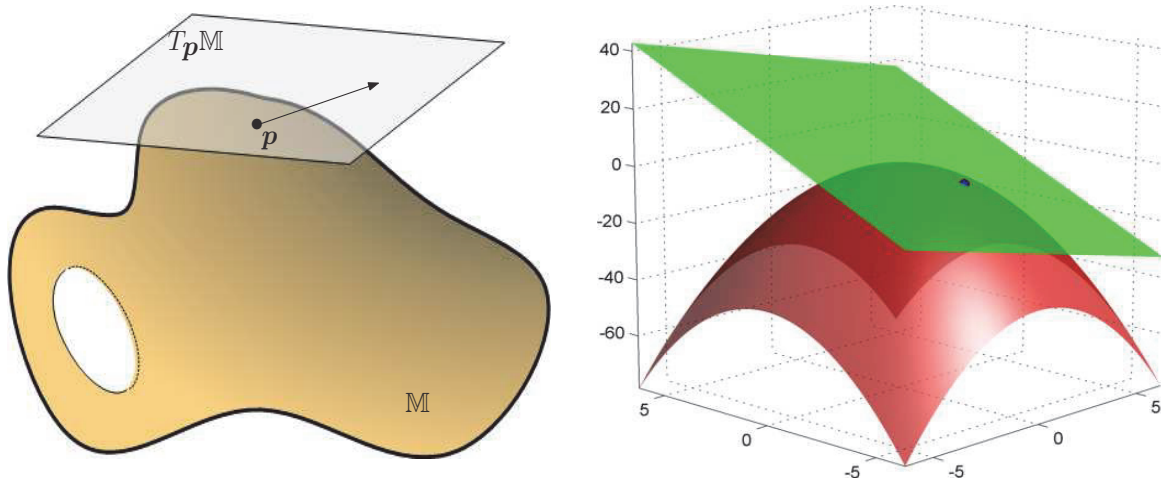


FIGURE 1.6: Illustration of the tangent space.

singularities are isolated, that is, there cannot be a sequence of nondegenerate singularities converging to a nondegenerate singularity $\mathbf{p} \in \mathbb{M}$. A *level set* $f^{-1}(a)$ of f at a value a may be composed of one or many connected components. Morse deformation lemma states that if no critical points exist between two level sets of f , then the two level sets are topologically equivalent and can be deformed onto one another [7]. In particular, they consist of the same number of connected components. Furthermore, Morse theory implies that topological changes on the level sets occur only at critical points. This property can be illustrated by considering the sub-surface \mathbb{M}_a consisting of all points at which f takes values less than or equal to a real number a

$$\mathbb{M}_a = \{\mathbf{p} \in \mathbb{M} : f(\mathbf{p}) \leq a\}. \quad (1.3)$$

Denote by L_a the set of points where the value of f is exactly a , that is $L_a = f^{-1}(a)$. Note that when a is a regular value, the set L_a is a smooth curve of \mathbb{M} and it is the boundary of \mathbb{M}_a as illustrated in Figure 1.7.

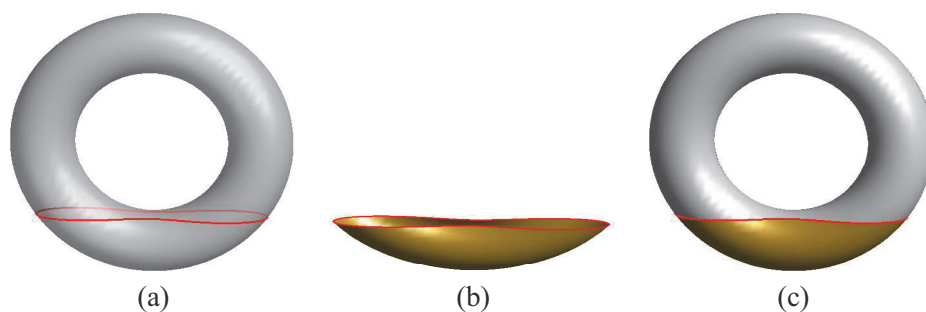


FIGURE 1.7: Illustration of: (a) Level curve L_a , (b) Subsurface \mathbb{M}_a , (c) Subsurface and Level curve.

Figure 1.8 shows the evolution of the subsurface \mathbb{M}_a as a changes, when f is a height function. If $a < \min_{\mathbf{p} \in \mathbb{M}} \{f(\mathbf{p})\}$, then $\mathbb{M}_a = \emptyset$. And as we increase the parameter a , the subsurface \mathbb{M}_a changes until it covers the entire surface \mathbb{M} .

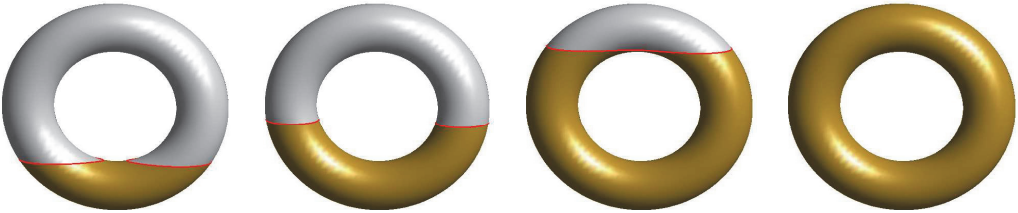


FIGURE 1.8: Evolution of \mathbb{M}_a as a changes.

An interesting concept related to Morse theory and very useful to analyze a surface topology is the Reeb graph. The latter is defined as a quotient space \mathbb{M}/\sim with the equivalence relation given by $\mathbf{p} \sim \mathbf{q}$ if and only if $f(\mathbf{p}) = f(\mathbf{q})$ and \mathbf{p}, \mathbf{q} belong to the same connected component of $f^{-1}(f(\mathbf{p}))$. An equivalence class is defined as $[\mathbf{p}] = \{\mathbf{q} \in \mathbb{M} : \mathbf{p} \sim \mathbf{q}\}$. Intuitively, \mathbb{M}/\sim is a space created by taking the space \mathbb{M} and gluing \mathbf{p} to any \mathbf{q} that satisfies $\mathbf{q} \sim \mathbf{p}$. The classes $[\mathbf{p}]$ are the connected components for the Reeb graph, and being in the same component is an equivalence relation:

$$\mathbf{q} \sim \mathbf{p} \iff f(\mathbf{q}) = f(\mathbf{p}) \text{ and } \mathbf{p}, \mathbf{q} \in \mathcal{C}, \tag{1.4}$$

where \mathcal{C} denotes the connected component of $f^{-1}(f(\mathbf{p}))$. In a Reeb graph representation of the height function, each connected component of a contour (i.e. $h^{-1}(z)$ where $z = h(x, y, z)$) corresponds to a point as shown in Figure 1.9.

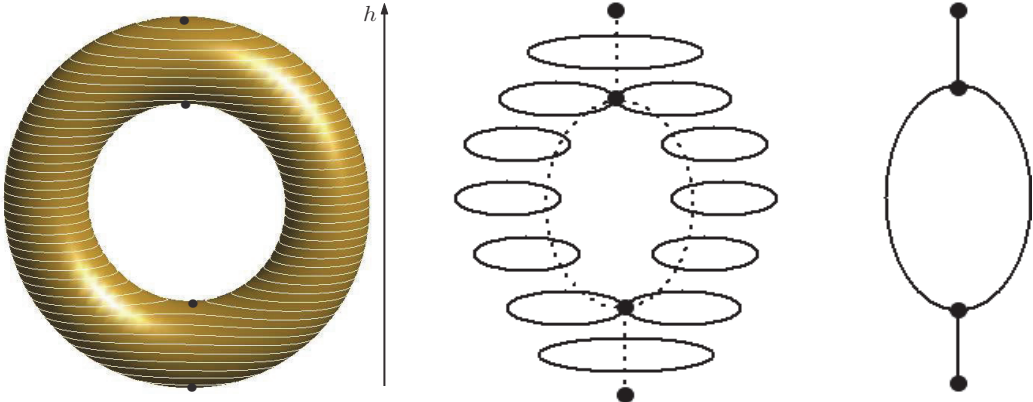


FIGURE 1.9: Reeb graph representation of a torus.

1.6 THESIS OVERVIEW

The organization of this thesis is as follows:

- In Chapter 2, we propose an image registration method by maximizing a Tsallis entropy-based divergence using a modified simultaneous perturbation stochastic approximation algorithm.
- In Chapter 3, we introduce a skeletal graph for topological 3D shape representation using Morse theory. The proposed skeletonization algorithm encodes a 3D shape into a topological Reeb graph using a normalized mixture distance function.
- In Chapter 4, we describe a skeletal graph for 3D object matching and retrieval. This skeleton is constructed from the second eigenfunction of the Laplace-Beltrami operator defined on the surface of the 3D object.
- In Chapter 5, we summarize the contributions in this thesis and propose some future research directions.

IMAGE REGISTRATION USING STOCHASTIC OPTIMIZATION

In this Chapter, we propose an image registration method by maximizing a Tsallis entropy-based divergence using a modified simultaneous perturbation stochastic approximation algorithm. Due to its convexity property, this divergence measure attains its maximum value when the conditional intensity probabilities between the reference image and the transformed target image are degenerate distributions. Experimental results are provided to demonstrate the registration accuracy of the proposed approach in comparison to existing entropic image alignment techniques.

2.1 INTRODUCTION

Image registration or alignment refers to the process of aligning images so that their details overlap accurately [2, 3]. Images are usually registered for the purpose of combining or comparing them, enabling the fusion of information in the images. Roughly speaking, the image alignment problem may be formulated as a two-step process: the first step is to define a dissimilarity measure that quantifies the quality of spatial alignment between the reference image and the spatially transformed target image, and the second step is to develop an efficient optimization algorithm for maximizing this dissimilarity measure in order to find the optimal transformation parameters. Recently, much attention has been paid to the image registration problem due to its importance in a variety of tasks including data fusion, navigation, motion detection, and clinical studies [2, 3]. A wide range of image registration techniques have been developed for many different types of applications and data, such as mean squared alignment, correlation registration, moment invariant matching, and entropic alignment [8, 9, 10, 11]. The latter will be the focus of this chapter. Inspired by the successful application of the mutual information measure [8, 9], and looking to address its limitations in

often difficult imagery, we proposed in [12] an information-theoretic approach to ISAR image registration by estimating the target motion during the imaging time, and it was accomplished using the Jensen-Rényi divergence. This generalized entropic measure enjoys appealing mathematical properties affording a great flexibility in a number of applications [13, 14, 15, 16].

In recent years, there has been a concerted research effort in statistical physics to explore the properties of Tsallis entropy, leading to a statistical mechanics that satisfies many of the properties of the standard theory [17]. In [18], a Tsallis entropy-based image mutual information approach, combined with a stochastic optimization algorithm, was proposed leading to accurate image registration results compared to the classical mutual information [8, 9].

In this chapter, we propose an entropic image alignment approach by maximizing the Jensen-Tsallis divergence [19] using a simultaneous perturbation stochastic approximation-based algorithm [20]. The main contributions in this chapter may be summarized as follows: (i) explore the use of the Jensen-Tsallis divergence as an alignment measure, (ii) develop an efficient optimization algorithm to maximize this divergence measure, and (iii) perform an experimental comparative study of the proposed approach with existing entropic image registration methods.

The rest of this chapter is organized as follows. Section 2.2 is devoted to the problem formulation, followed by a theoretical analysis of the Jensen-Tsallis divergence and a derivation of its upper bound. Then, we develop a modified simultaneous perturbation stochastic approximation algorithm to maximize the divergence measure. In Section 2.3, we describe the proposed image alignment method and discuss its most important algorithmic steps in more details. In Section 2.4, we provide experimental results to show the effectiveness and the registration accuracy of the proposed approach.

2.2 PROBLEM FORMULATION

In the continuous domain, an image is defined as a real-valued function $I : \Omega \rightarrow \mathbb{R}$, and Ω is a nonempty, bounded, open set in \mathbb{R}^2 (usually Ω is a rectangle in \mathbb{R}^2). Throughout, we denote by $\boldsymbol{x} = (x_1, x_2)$ a pixel location in Ω . Given two misaligned images, the reference image I_1 and the target image I_2 as depicted in Figure 2.1, the image alignment or registration problem may be formulated as an optimization problem

$$\boldsymbol{\ell}^* = \arg \max_{\boldsymbol{\ell}} D(I_1(\boldsymbol{x}), I_2(\Phi_{\boldsymbol{\ell}}(\boldsymbol{x}))) \quad (2.1)$$

where $D(\cdot, \cdot)$ is a dissimilarity measure that quantifies the discrepancy between the reference image and the transformed target image; and $\Phi_{\boldsymbol{\ell}} : \Omega \leftarrow \Omega$ is a spatial transformation parameterized by a parameter vector

ℓ . An example of such a mapping is a Euclidean transformation with a parameter vector $\ell = (\mathbf{t}, \theta, \mathbf{s})$, where $\mathbf{t} = (t_x, t_y)$ is a translational parameter vector, θ is a rotational parameter, and $\mathbf{s} = (s_x, s_y)$ is a scaling parameter vector.

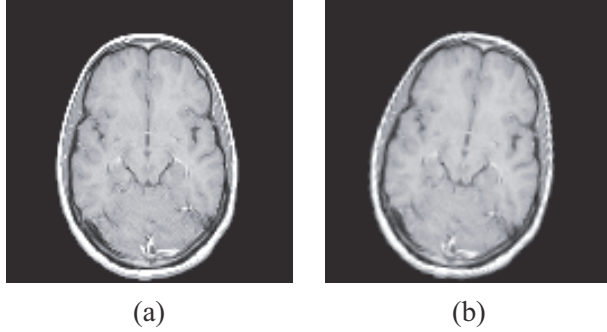


FIGURE 2.1: (a) Reference image I_1 . (b) Target image I_2 .

The goal of image registration is to align the target image to the reference image by maximizing the dissimilarity measure $D(I_1(\mathbf{x}), I_2(\Phi_\ell(\mathbf{x})))$ using an optimization scheme in order to find the optimal spatial transformation parameters. Note that since the image pixel values are integers, a bilinear interpolation may be used to determine the values of $I_2(\Phi_\ell(\mathbf{x}))$ when $\Phi_\ell(\mathbf{x})$ is not an integer. In this chapter, we use the Jensen-Tsallis divergence as a dissimilarity measure [19], and a modified simultaneous perturbation stochastic approximation (SPSA) approach as an optimization algorithm [20].

2.2.1 JENSEN-TSALLIS DIVERGENCE

Let $X = \{x_1, x_2, \dots, x_k\}$ be a finite set with a probability distribution $\mathbf{p} = (p_1, p_2, \dots, p_k)$ where $k > 1$. Shannon's entropy is defined as $H(\mathbf{p}) = -\sum_{j=1}^k p_j \log(p_j)$, and it is a measure of uncertainty, dispersion, information, and randomness. The maximum uncertainty or equivalently minimum information is achieved by the uniform distribution. Hence, we can think of the entropy as a measure of uniformity of a probability distribution. Consequently, when uncertainty is higher it becomes more difficult to predict the outcome of a draw from a probability distribution. A generalization of Shannon entropy is Rényi entropy [21] given by

$$R_\alpha(\mathbf{p}) = \frac{1}{1-\alpha} \log \sum_{j=1}^k p_j^\alpha, \quad \alpha \in (0, 1) \cup (1, \infty). \quad (2.2)$$

Another important generalization of Shannon entropy is Tsallis entropy [22, 23, 17] given by

$$H_\alpha(\mathbf{p}) = \frac{1}{1-\alpha} \left(\sum_{j=1}^k p_j^\alpha - 1 \right) = -\sum_{j=1}^k p_j^\alpha \log_\alpha(p_j), \quad (2.3)$$

where \log_α is the α -logarithm function defined as $\log_\alpha(x) = (1 - \alpha)^{-1}(x^{1-\alpha} - 1)$ for $x > 0$. This generalized entropy was first introduced by Havrda and Charvát in [22], who were primarily interested in providing another measure of entropy. Tsallis, however, appears to have been principally responsible for investigating and popularizing the widespread physics applications of this entropy which is referred to nowadays as Tsallis entropy [17]. It is worth noting that for $\alpha \in (0, 1]$, Rényi and Tsallis entropies are both concave functions; and for $\alpha > 1$ Tsallis entropy is also concave, but Rényi entropy is neither concave nor convex. Furthermore, both entropies tend to Shannon entropy $H(\mathbf{p})$ as $\alpha \rightarrow 1$, and are related by

$$H_\alpha(\mathbf{p}) = \frac{1}{1 - \alpha} [\exp\{(1 - \alpha)R_\alpha(\mathbf{p})\} - 1]. \quad (2.4)$$

For $x, y > 0$, the α -logarithm function satisfies the following property

$$\log_\alpha(xy) = \log_\alpha x + \log_\alpha y + (\alpha - 1) \log_\alpha x \log_\alpha y. \quad (2.5)$$

If we consider that a physical system can be decomposed in two statistical independent subsystems with probability distributions \mathbf{p} and \mathbf{q} , then using Eq. (2.5) it can be shown that the joint Tsallis entropy is pseudo-additive

$$H_\alpha(\mathbf{p}, \mathbf{q}) = H_\alpha(\mathbf{p}) + H_\alpha(\mathbf{q}) + (1 - \alpha)H_\alpha(\mathbf{p})H_\alpha(\mathbf{q}), \quad (2.6)$$

whereas the joint Shannon and Rényi entropies satisfy the additivity property: $H(\mathbf{p}, \mathbf{q}) = H(\mathbf{p}) + H(\mathbf{q})$, and $R_\alpha(\mathbf{p}, \mathbf{q}) = R_\alpha(\mathbf{p}) + R_\alpha(\mathbf{q})$.

The pseudo-additivity property implies that Tsallis entropy has a nonextensive property for statistical independent systems, whereas Shannon and Rényi entropies have the extensive property (i.e. additivity). Furthermore, standard thermodynamics is extensive because of the short-range nature of the interaction between subsystems of a composite system. In other words, when a system is composed of two statistically independent subsystems, then the Boltzman-Gibbs entropy of the composite system is just the sum of entropies of the individual systems, and hence the correlations between the subsystems are not accounted for. Tsallis entropy, however, does take into account these correlations due to its pseudo-additivity property. Furthermore, many objects in nature interact through long-range interactions such as gravitational or unscreened Coulomb forces. Therefore the property of additivity is very often violated, and consequently the use of a nonextensive entropy is more suitable for real-world applications. Figure 2.2 depicts Tsallis entropy of a Bernoulli distribution $\mathbf{p} = (p, 1 - p)$, with different values of the parameter α . As illustrated in Figure 2.2, the measure of uncertainty is at a minimum when Shannon entropy is used, and for $\alpha \geq 1$ it

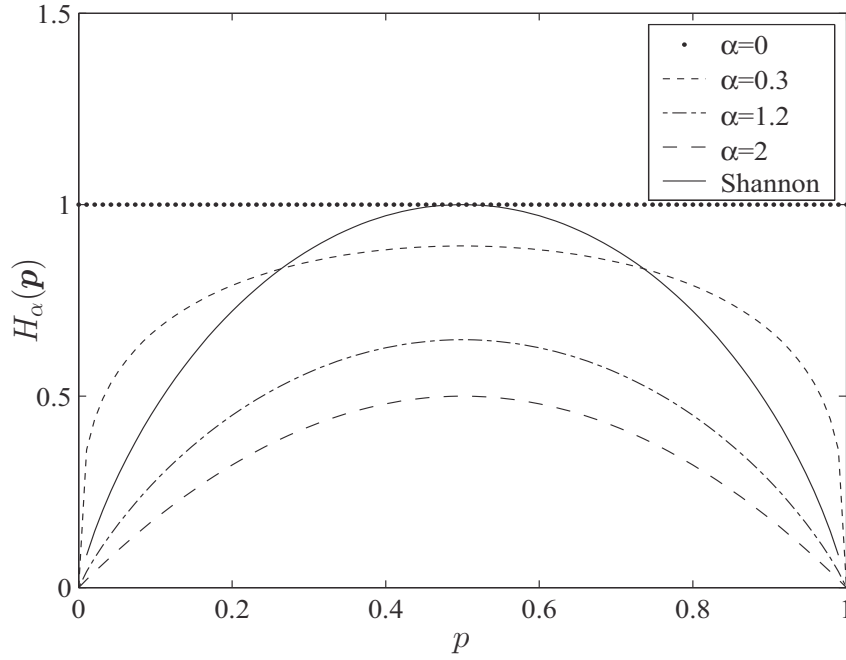


FIGURE 2.2: Tsallis entropy $H_\alpha(\mathbf{p})$ of a Bernoulli distribution $\mathbf{p} = (p, 1 - p)$ for different values of α .

decreases as the parameter α increases. Furthermore, Tsallis entropy attains a maximum uncertainty when its exponential order α is equal to zero.

Definition 2.2.1 Let $\mathbf{p}_1, \mathbf{p}_2, \dots, \mathbf{p}_n$ be n probability distributions. The Jensen-Tsallis divergence is defined as

$$D_\alpha^\omega(\mathbf{p}_1, \dots, \mathbf{p}_n) = H_\alpha\left(\sum_{i=1}^n \omega_i \mathbf{p}_i\right) - \sum_{i=1}^n \omega_i H_\alpha(\mathbf{p}_i), \quad (2.7)$$

where $H_\alpha(\mathbf{p})$ is Tsallis entropy, and $\omega = (\omega_1, \omega_2, \dots, \omega_n)$ is a weight vector such that $\sum_{i=1}^n \omega_i = 1$ and $\omega_i \geq 0$.

Using the Jensen inequality, it is easy to check that the Jensen-Tsallis divergence is nonnegative for $\alpha > 0$. It is also symmetric and vanishes if and only if the probability distributions $\mathbf{p}_1, \mathbf{p}_2, \dots, \mathbf{p}_n$ are equal, for all $\alpha > 0$. Note that the Jensen-Shannon divergence [24] is a limiting case of the Jensen-Tsallis divergence when $\alpha \rightarrow 1$.

Unlike other entropy-based divergence measures such as the Kullback-Leibler divergence, the Jensen-Tsallis divergence has the advantage of being symmetric and generalizable to any arbitrary number of probability distributions or data sets, with a possibility of assigning weights to these distributions. Fig-

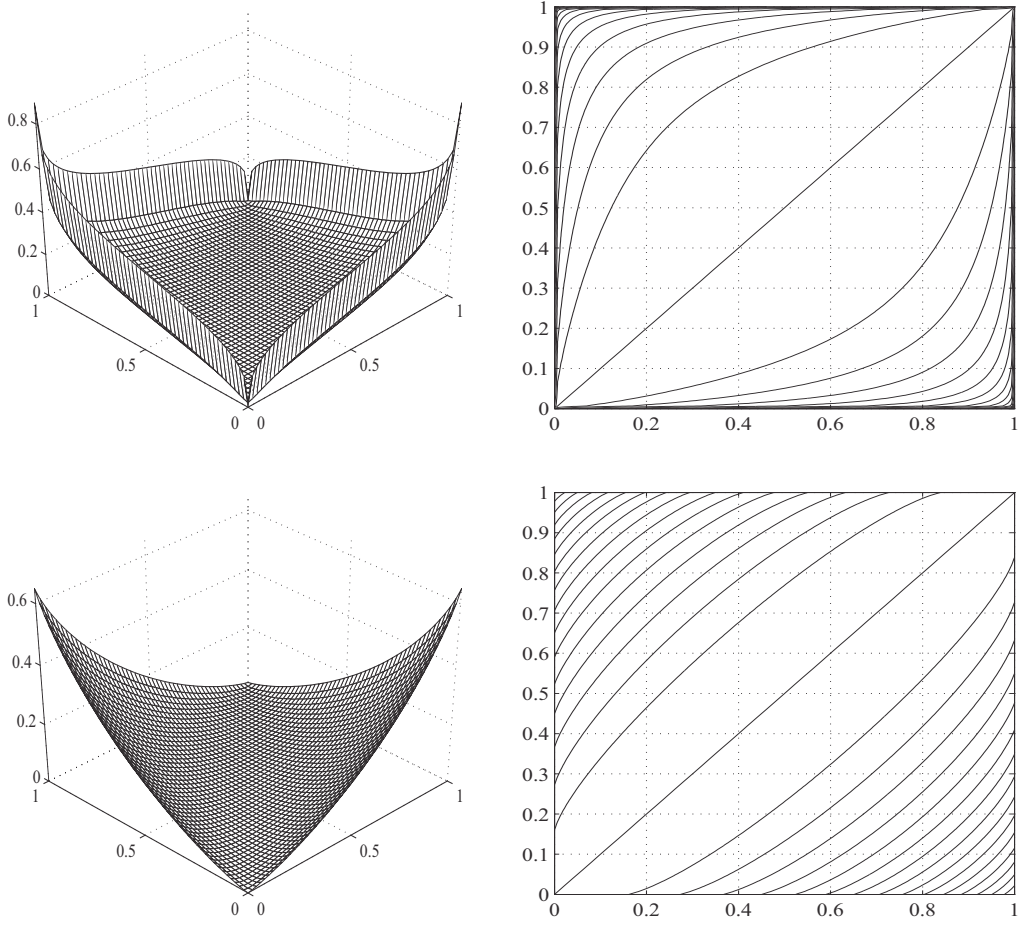


FIGURE 2.3: Surface/contour plots of Jensen-Tsallis divergence between two Bernoulli distributions $\mathbf{p} = (p, 1 - p)$ and $\mathbf{q} = (q, 1 - q)$, and with equal weights $\omega_1 = \omega_2 = 1/2$. First row: $\alpha = 0.3$. Second row: $\alpha = 1.2$.

Figure 2.3 shows three-dimensional representations and contour plots of the Jensen-Tsallis divergence with equal weights between two Bernoulli distributions $\mathbf{p} = (p, 1 - p)$ and $\mathbf{q} = (q, 1 - q)$, for $\alpha \in (0, 1)$ and also for $\alpha \in (1, \infty)$.

2.2.2 PROPERTIES OF THE JENSEN-TSALLIS DIVERGENCE

The following result establishes the convexity of the Jensen-Tsallis divergence of a set of probability distributions [23].

Proposition 2.2.2 For $\alpha \in [1, 2]$, the Jensen-Tsallis divergence D_α^ω is a convex function of $\mathbf{p}_1, \mathbf{p}_2, \dots, \mathbf{p}_n$.

In the sequel, we will restrict $\alpha \in [1, 2]$, unless specified otherwise. In addition to its convexity property, the Jensen-Tsallis divergence is an adapted measure of disparity among n probability distributions as shown in the next result.

Proposition 2.2.3 *The Jensen-Tsallis divergence D_α^ω achieves its maximum value when $\mathbf{p}_1, \mathbf{p}_2, \dots, \mathbf{p}_n$ are degenerate distributions, that is $\mathbf{p}_i = (\delta_{ij})$, where $\delta_{ij} = 1$ if $i = j$ and 0 otherwise.*

Proof: The domain of the Jensen-Tsallis divergence is a convex polytope in which the vertices are degenerate probability distributions. That is, the maximum value of the Jensen-Tsallis divergence occurs at one of the extreme points which are the degenerate distributions. ■

2.2.3 MODIFIED SPSA OPTIMIZATION ALGORITHM

The implementation of SPSA depends on a simple “simultaneous perturbation” approximation to the gradient [20]. It uses only two measurements of the loss function in each iteration independent of the number of the problem dimension. In contrast, the standard stochastic approximation method like finite difference stochastic approximation varies the variables one at a time. If the number of terms being optimized is equal to ν , then the finite-difference method takes 2ν measurements of the objective function at each iteration.

Next we propose a modified SPSA algorithm that maximizes a real-valued loss function $\mathcal{L}(\ell)$, where ℓ denotes a ν -dimensional transformation parameter vector that needs to be optimally found by maximizing $\mathcal{L}(\ell)$. The proposed SPSA algorithm starts from an initial guess of ℓ , where the iteration process depends on the above-mentioned highly efficient “simultaneous perturbation” approximation to the gradient $g(\ell) \equiv \nabla \mathcal{L}(\ell)$. It is assumed that $\mathcal{L}(\ell)$ is a differentiable function of ℓ and that the maximum point ℓ^* corresponds to a zero point of the gradient, i.e.,

$$g(\ell^*) = \nabla \mathcal{L}(\ell^*) = 0. \quad (2.8)$$

Let $y(\ell) = \mathcal{L}(\ell) + \text{noise}$, and $\hat{\ell}$ be the estimate of ℓ . Then the gradient estimate $\hat{g}(\hat{\ell})$ in the k -th iteration is given by

$$\hat{g}_k(\hat{\ell}_k) = \frac{y(\hat{\ell}_k + c_k \boldsymbol{\varepsilon}_k) - y(\hat{\ell}_k - c_k \boldsymbol{\varepsilon}_k)}{2c_k \boldsymbol{\varepsilon}_k} \quad (2.9)$$

where c_k is the perturbation coefficient, and ε_k is the ν -dimensional simultaneous perturbation vector that is Monte Carlo-generated. At the end of each iteration, the $\hat{\ell}_k$ estimate is updated using the standard stochastic approximation form

$$\hat{\ell}_{k+1} = \hat{\ell}_k + a_k \hat{g}_k(\hat{\ell}_k). \quad (2.10)$$

Note that the choice of the gain sequences a_k and c_k should satisfy some typical stochastic approximation conditions [20].

2.3 PROPOSED METHOD

Our proposed approach may now be described as follows: Given two images that need to be registered, we first compute their conditional intensity probabilities and the Jensen-Tsallis divergence between them. Then we optimize this divergence measure using the modified SPSA algorithm.

Without loss of generality, we consider a Euclidean transformation Φ_{ℓ} with a parameter vector $\ell = (\mathbf{t}, \theta)$, i.e. a transformation with translation parameter vector $\mathbf{t} = (t_x, t_y)$, and a rotation parameter θ . In other words, for an image pixel location $\mathbf{x} = (x, y)$ the Euclidean transformation is defined as $\Phi_{\ell}(\mathbf{x}) = R\mathbf{x} + \mathbf{t}$, where R is a rotation matrix given by

$$R = \begin{pmatrix} \cos \theta & \sin \theta \\ -\sin \theta & \cos \theta \end{pmatrix}. \quad (2.11)$$

Denote by $\mathcal{X} = \{x_1, x_2, \dots, x_n\}$ and $\mathcal{Y} = \{y_1, y_2, \dots, y_n\}$ the sets of pixel intensity values of the reference image $I_1(\mathbf{x})$ and the transformed target image $I_2(\Phi_{\ell}(\mathbf{x}))$ respectively. Let X and Y be two random variables taking values in \mathcal{X} and \mathcal{Y} .

The proposed approach consists of the following main steps:

- (i) Find the conditional intensity probabilities

$$\mathbf{p}_i = \mathbf{p}_i(I_2(\Phi_{\ell}(\mathbf{x}))|I_1(\mathbf{x})) = (p_{ij})_{j=1, \dots, n}, \quad \forall i = 1, \dots, n, \quad (2.12)$$

where $p_{ij} = P(Y = y_j | X = x_i)$, $j = 1, \dots, n$.

- (ii) Find the optimal parameter vector $\ell^* = (\mathbf{t}^*, \theta^*)$ of the Jensen-Tsallis objective function

$$\ell^* = \arg \max_{\ell} D_{\alpha}^{\omega}(\mathbf{p}_1, \dots, \mathbf{p}_n) \quad (2.13)$$

using the modified SPSA optimization algorithm.

Note that if the images I_1 and I_2 are exactly matched, then $p_i = (\delta_{ij})$ and by Proposition 2.2.3, the Jensen-Tsallis divergence is therefore maximized. Figure 2.5(1)-(2) show two MRI images in which the misalignment corresponds to a clockwise rotation with an angle $\theta = 10^\circ$. The conditional probability distributions $\{p_i\}$ are crisp, as shown in Figure 2.5(3), when the two images are aligned, and dispersed, as depicted in Figure 2.5(4), when they are not matched.

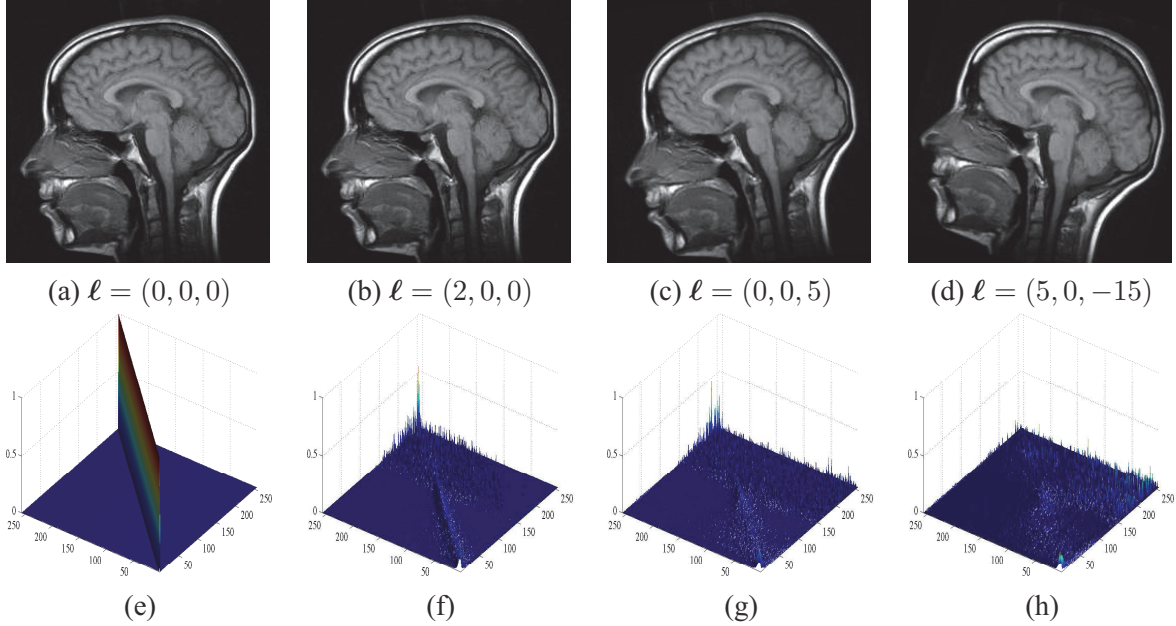


FIGURE 2.4: 3D plots of conditional probability distributions for different transformation vectors.

Also, it is worth pointing out that if $\alpha = 1$ and $\omega_i = P(X = x_i)$ then the Jensen-Tsallis divergence becomes mutual information, indicating that the Jensen-Tsallis divergence induces a dissimilarity measure that provides a more general framework for the image registration problem.

2.4 EXPERIMENTAL RESULTS

We tested the performance of the proposed entropic image registration method on a variety of images. In all experiments we used an entropic index $\alpha = 2$ and the normalized histogram as the weight vector ω for the Jensen-Tsallis divergence. In our first experiment, we applied a Euclidean transformation Φ_ℓ with different values of the parameter vector $\ell = (t_x, t_y, \theta)$ to the three reference medical images shown in Figure 2.6 through Figure 2.8. And, we used the modified SPSA algorithm to find the optimal parameter vector $\ell^* = (t_x^*, t_y^*, \theta^*)$. We also compared the image alignment results of the proposed approach to existing image registration techniques based on the mutual information [8], Tsallis mutual information [18], and Jensen-

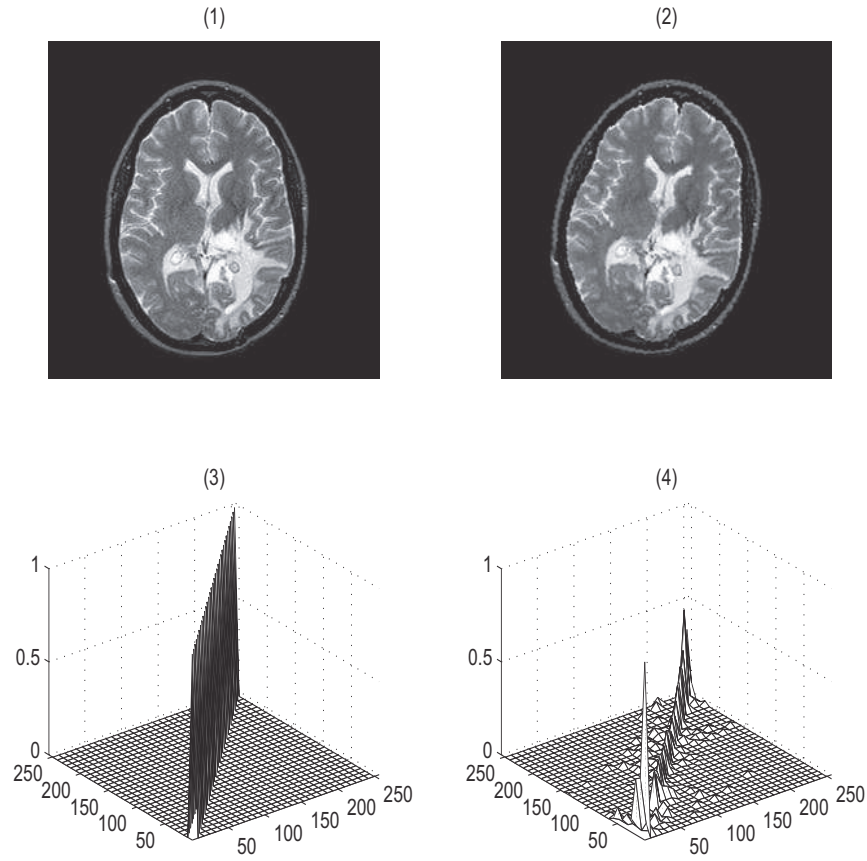


FIGURE 2.5: Conditional probability distributions.

Rényi divergence [12]. The output registration results are shown in Figure 2.6 through Figure 2.8, where the absolute differences $|t_x - t_x^*|$, $|t_y - t_y^*|$, and $|\theta - \theta^*|$ between the true and the estimated transformation parameters are also displayed as error bars for three different transformation parameter vectors $\ell = (5, 5, 5)$, $\ell = (5, 10, 15)$, and $\ell = (10, 20, 20)$. From these figures, it is clear that the estimated values of the transformation parameters indicate the effectiveness and the registration accuracy of the proposed algorithm. Amongst the other methods, we noticed that the Tsallis mutual information approach performs relatively well at higher values of the rotation angle, but poorly at higher values of the translation parameters compared to the proposed approach. Moreover, the much better performance of our method is in fact consistent with a variety of images used for experimentation.

In the next experiments, we examine the effects of the values of the weight vector ω and the entropic index α on the performance of the proposed image registration approach.

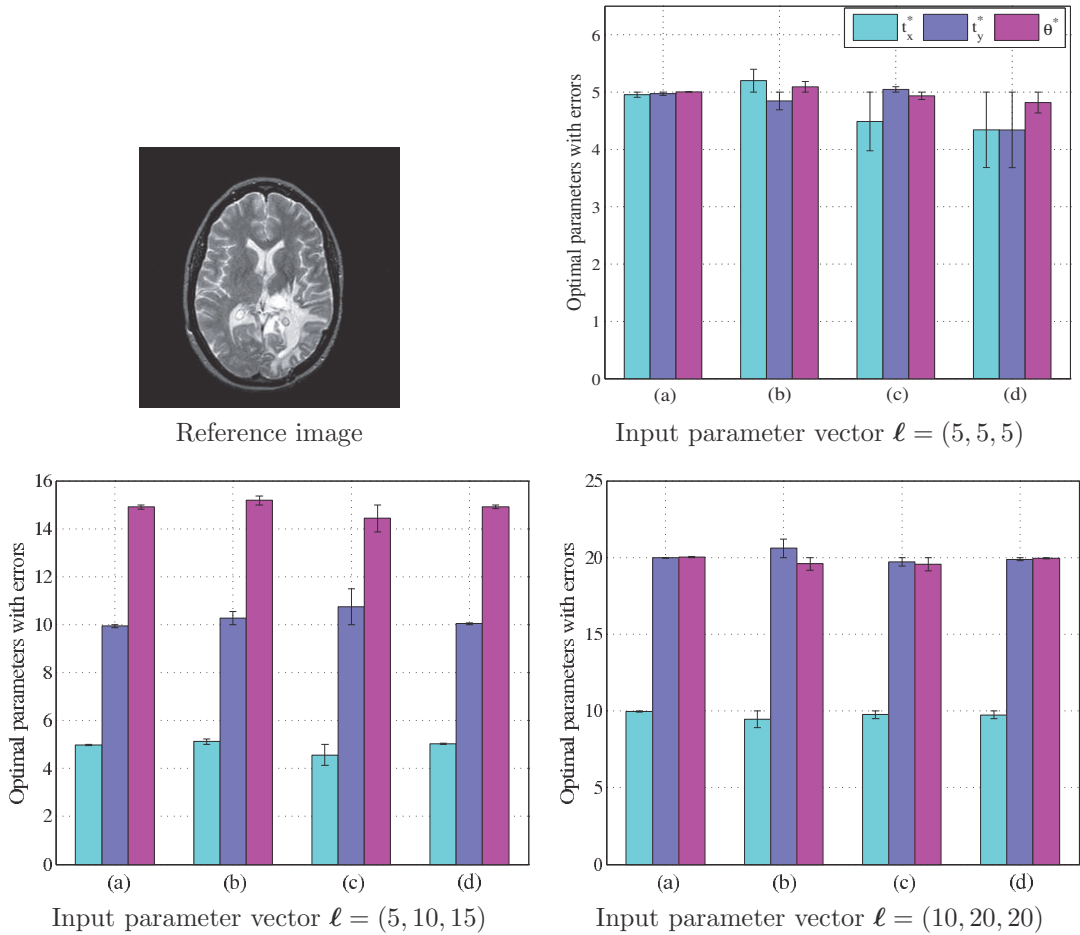


FIGURE 2.6: Bar plots of optimal registration parameter vector $\ell^* = (t_x^*, t_y^*, \theta^*)$ with errors $\ell - \ell^*$, using (a) proposed method, (b) Jensen-Rényi divergence, (c) mutual information, and (d) Tsallis mutual information.

2.4.1 EFFECT OF WEIGHT ON THE JENSEN-TSALLIS DIVERGENCE

Figure 2.9 and Figure 2.10 show the plots for the divergence values of Jensen-Tsallis and Jensen-Rényi respectively, in the case of a uniform weight $\omega_i = 1/n$. As shown in Figure 2.10, the Jensen-Rényi divergence has the same maximum value given different values of α , whereas the maximum value of the Jensen-Tsallis divergence drops significantly when the value of α increases. Also, it is worth noting that the output of the Jensen-Tsallis divergence shows a sharp impulse located at where the images are aligned, and a uniform value anywhere else if a uniform weight $\omega_i = 1/n$ is used and also if α is larger than 1. This property indicates a dramatic change of the gradient. Indeed, through extensive experiments we noticed that the modified SPSA algorithm experiences difficulty in converging to the optimal solution when the initial guess of ℓ is not in a small range where a noticeable gradient change is observed. To circumvent this problem,

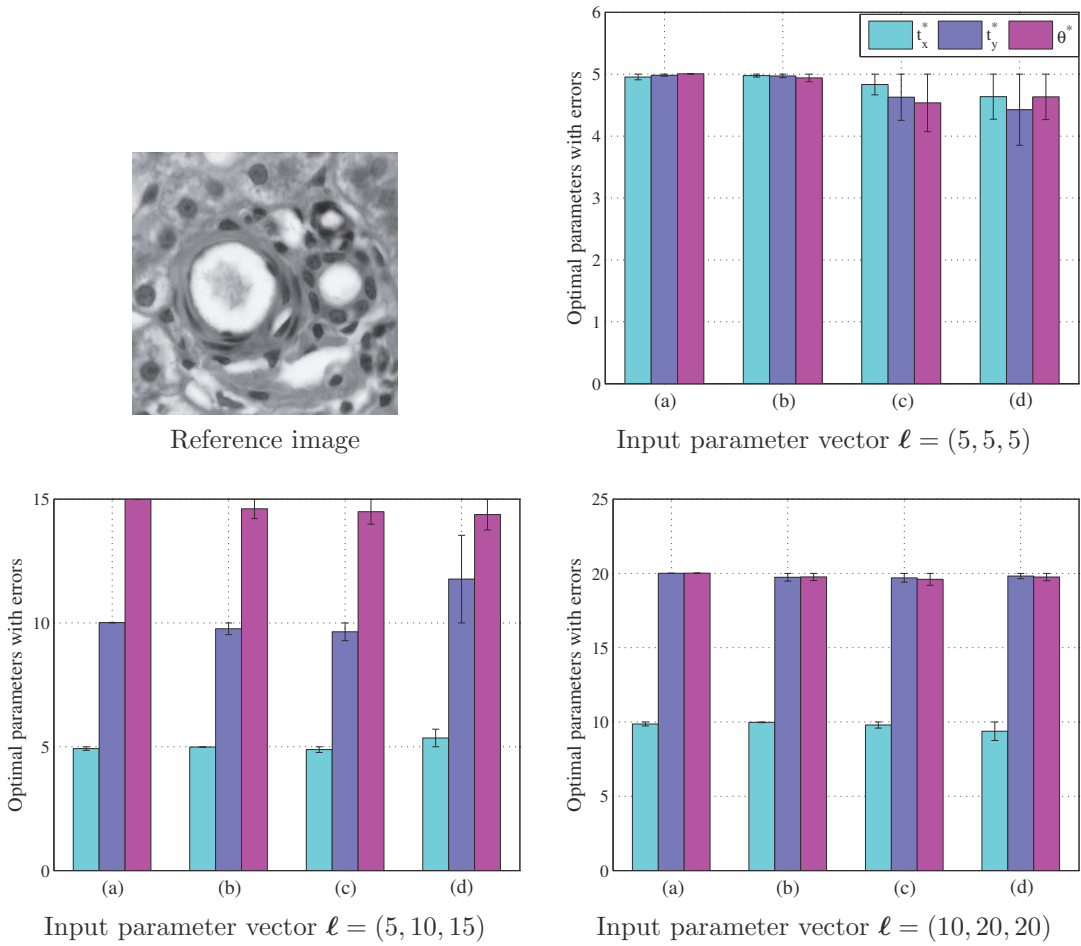
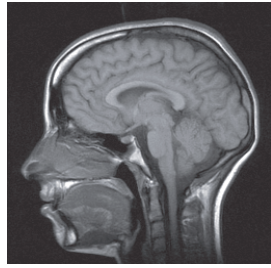


FIGURE 2.7: Bar plots of optimal registration parameter vector $\ell^* = (t_x^*, t_y^*, \theta^*)$ with errors $\ell - \ell^*$, using (a) proposed method, (b) Jensen-Rényi divergence, (c) mutual information, and (d) Tsallis mutual information.

we used the normalized histogram of the reference image I_1 as the weight vector ω instead of a uniform weight. The Jensen-Tsallis and Jensen-Rényi divergences with the normalized histogram weights are shown in Figure 2.11 and Figure 2.12 respectively.

2.4.2 EFFECT OF α ON THE JENSEN-TSALLIS DIVERGENCE

Most medical imaging methods, for instance, produce a full three-dimensional (3D) volume, and the medical scans are viewed as a series of superposed two-dimensional (2D) slices of their full 3D volume. The MRI 3D volume of a healthy patient, shown in Figure 2.13(a), consists of 27 horizontal slices and each slice is 128×128 pixels. To examine the effect of the entropic index α , we applied the proposed approach to two horizontal slices of this MRI 3D volume: the reference image and the misaligned image, which are



Reference image

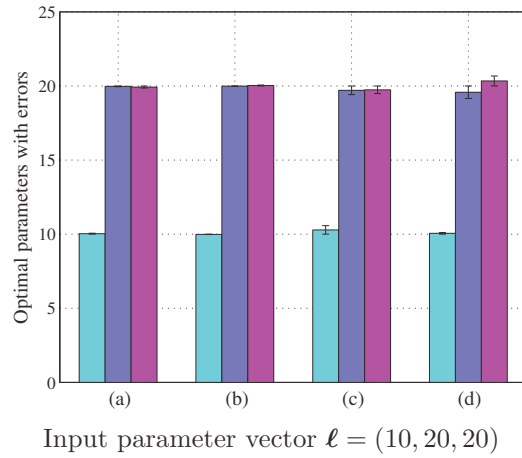
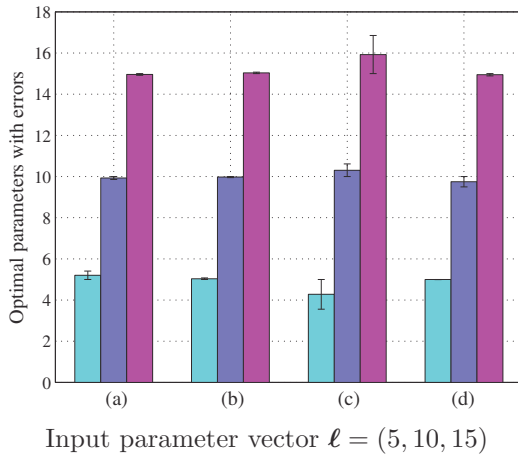
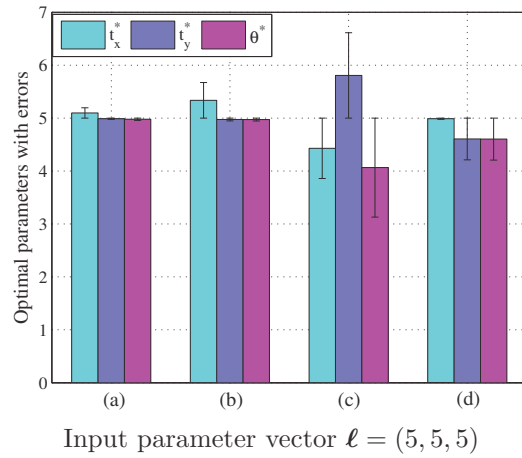
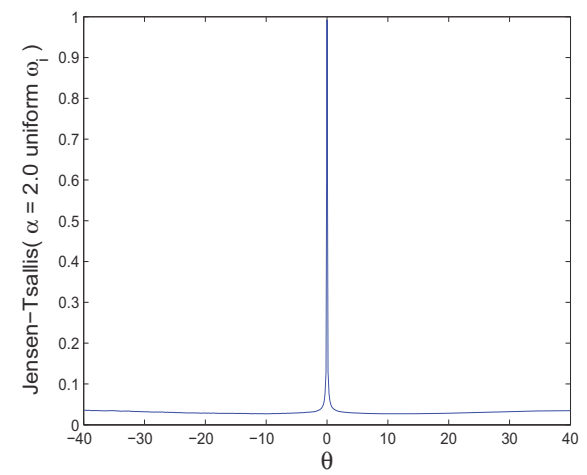
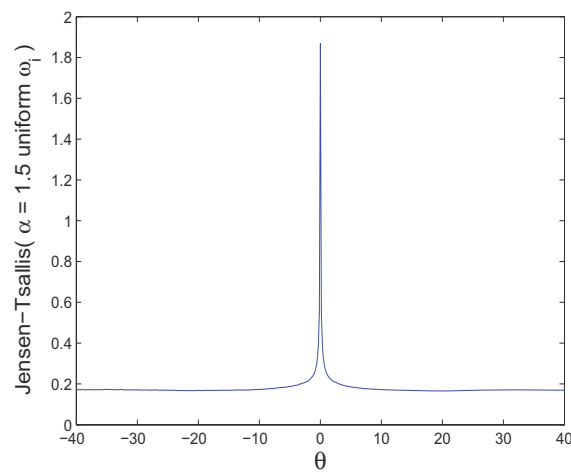
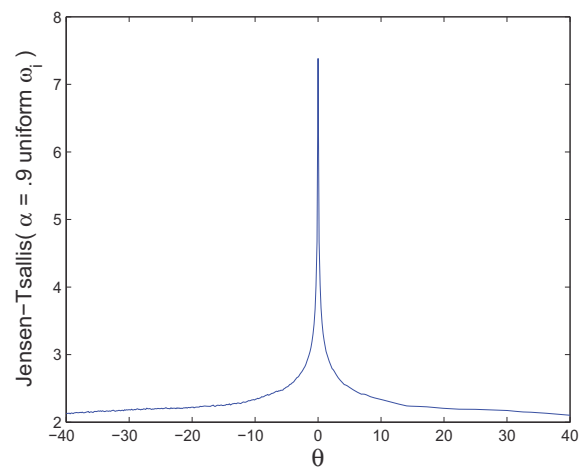
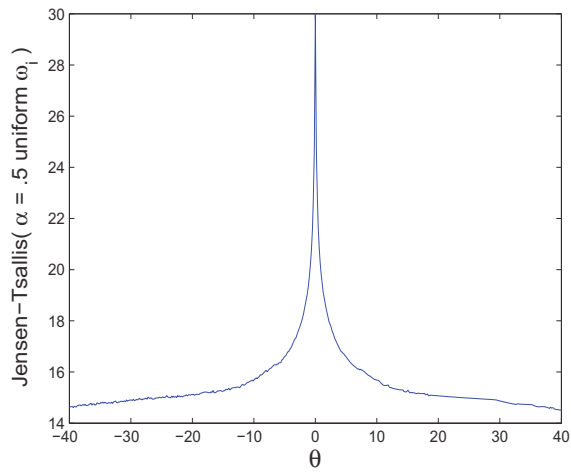


FIGURE 2.8: Bar plots of optimal registration parameter vector $\ell^* = (t_x^*, t_y^*, \theta^*)$ with errors $\ell - \ell^*$, using (a) proposed method, (b) Jensen-Rényi divergence, (c) mutual information, and (d) Tsallis mutual information.

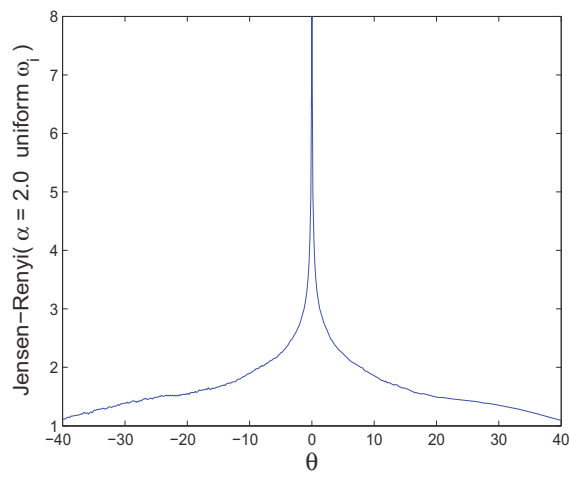
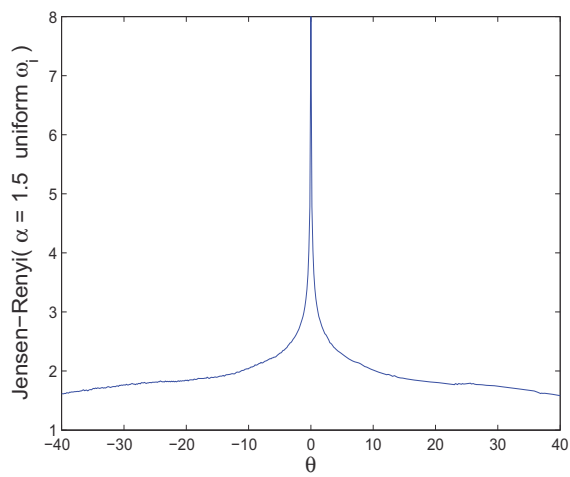
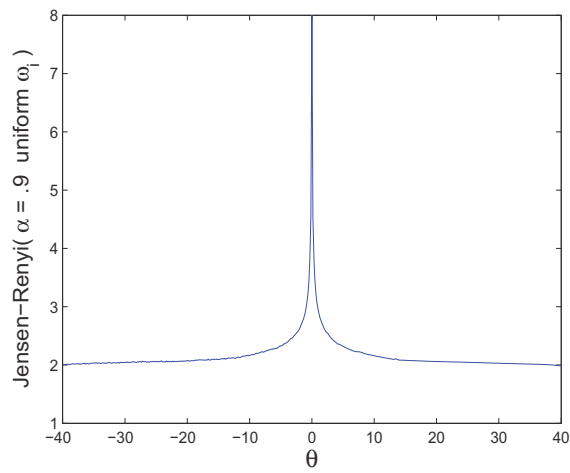
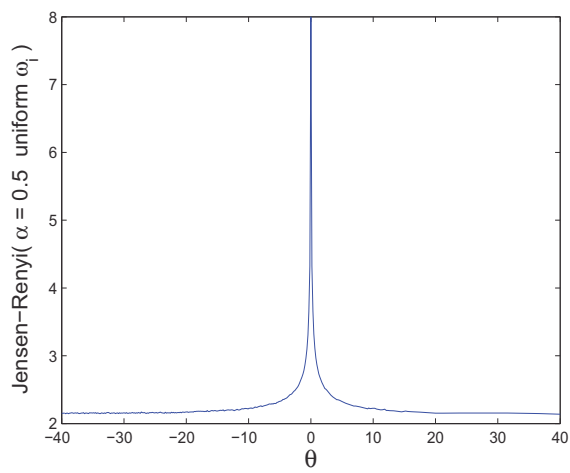
shown on the left and right-hand sides of Figure 2.13(b) respectively. Figure 2.14 and Figure 2.15 display the output results of Jensen-Rényi and Jensen-Tsallis divergences with uniform weight and also with normalized histogram weight.



(c)

(d)

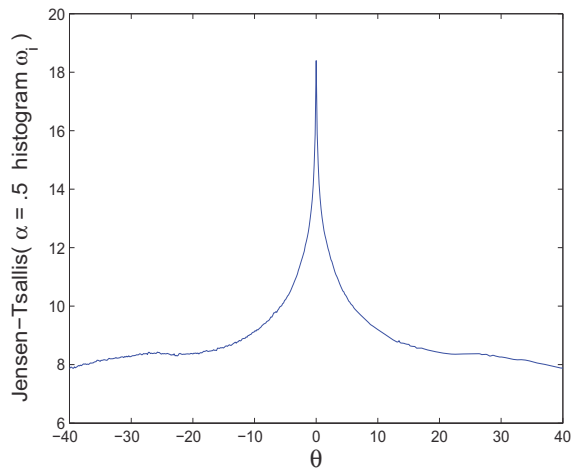
FIGURE 2.9: Jensen-Tsallis divergence with uniform weight.



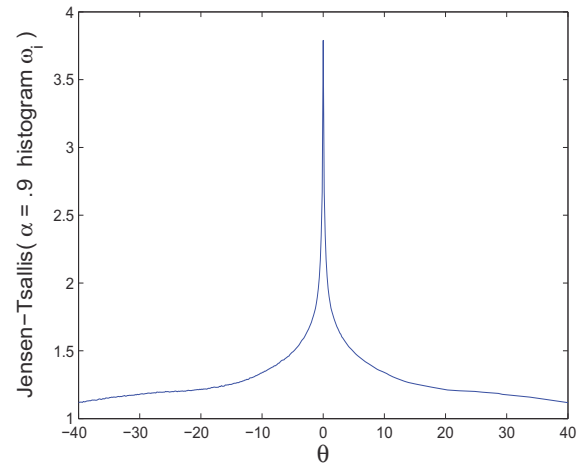
(c)

(d)

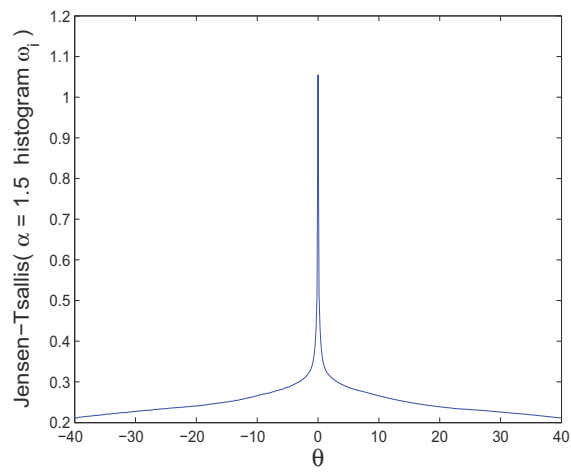
FIGURE 2.10: Jensen-Rényi divergence with uniform weight.



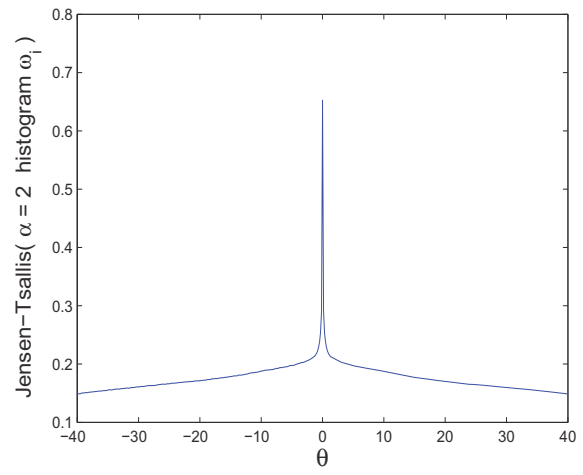
(a)



(b)

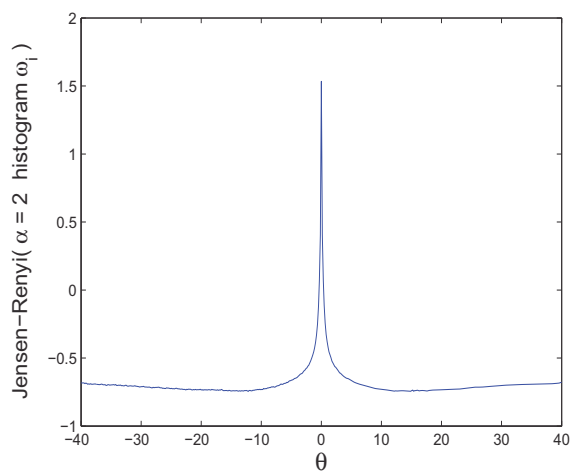
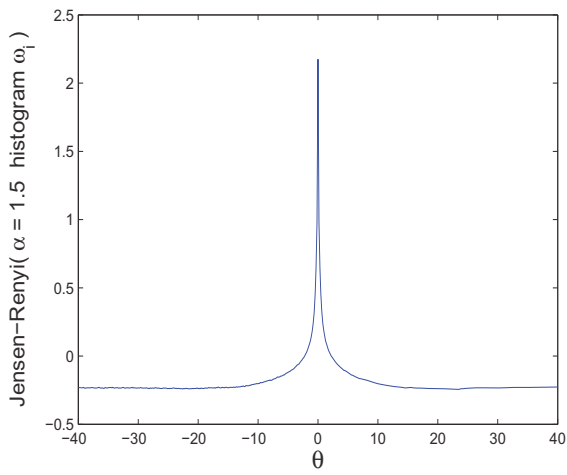
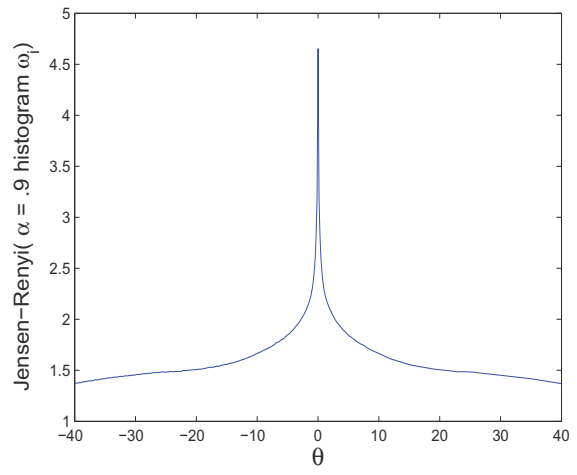
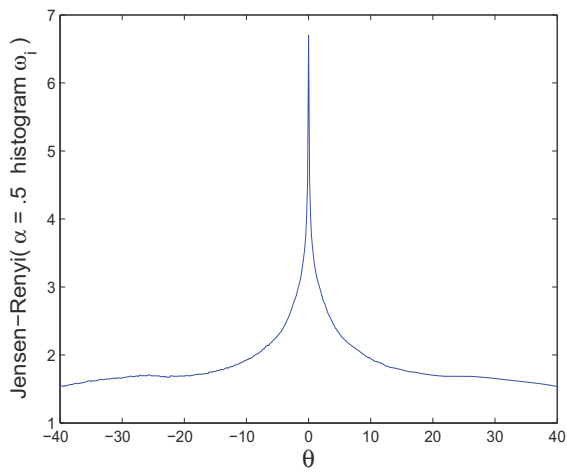


(c)



(d)

FIGURE 2.11: Jensen-Tsallis divergence with normalized histogram weight.



(c)

(d)

FIGURE 2.12: Jensen-Rényi divergence with normalized histogram weight.

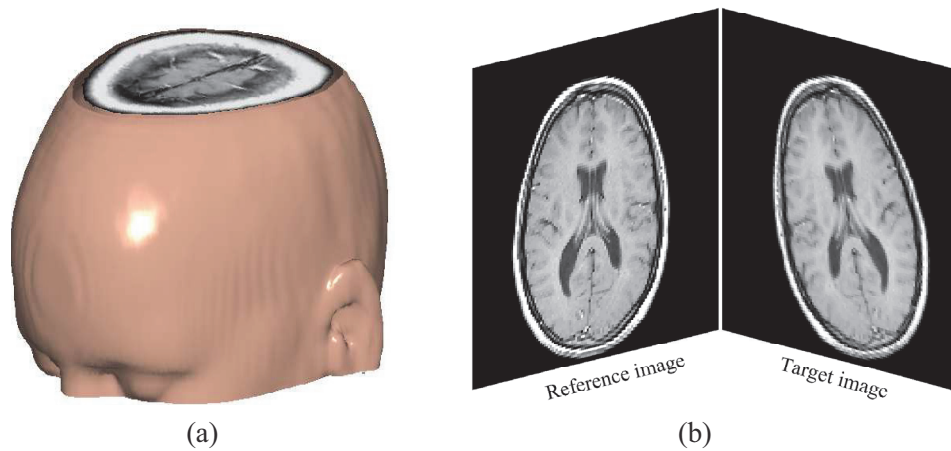


FIGURE 2.13: (a) MRI 3D volume. (b) Reference and target images for testing the effect of the entropic index.

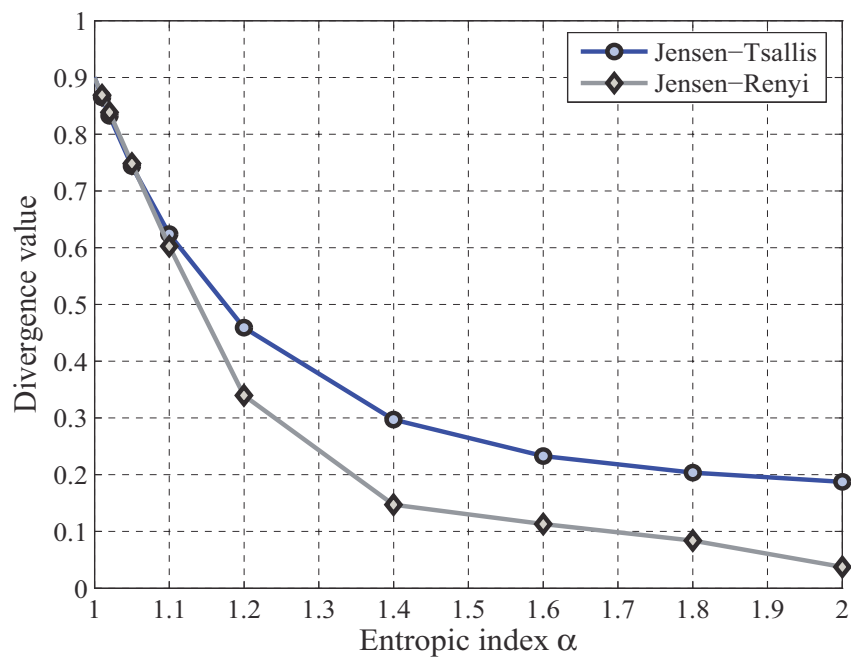


FIGURE 2.14: Divergence values with uniform weight ω_i .

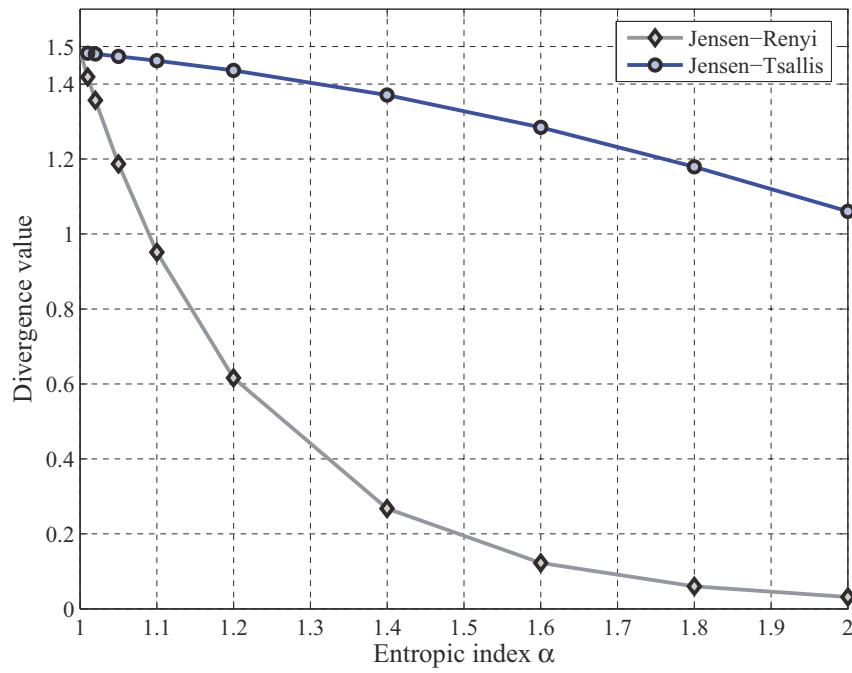


FIGURE 2.15: Divergence values with normalized histogram weight ω_i .

REEB GRAPH PATH DISSIMILARITY FOR 3D OBJECT MATCHING AND RETRIEVAL

In this Chapter, we introduce a skeletal graph for topological 3D shape representation using Morse theory. The proposed skeletonization algorithm encodes a 3D shape into a topological Reeb graph using a normalized mixture distance function. We also propose a novel graph matching algorithm by comparing the relative shortest paths between the skeleton endpoints. Experimental results demonstrate the feasibility of the proposed topological Reeb graph as a shape signature for 3D object matching and retrieval.

3.1 INTRODUCTION

The importance of 3D shape recognition is increasing rapidly in the field of computer graphics and multimedia communication due to the difficulty in processing information efficiently without its recognition. With the increasing use of scanners to create 3D models which are usually represented as triangle meshes in computer graphics and geometric-aided design, shape recognition of 3D objects has become an active research field with the recent developments in solid modeling and visualization [7]. These 3D scanners are used extensively by the entertainment industry in the production of movies and 3D games. Other common applications of the 3D technology include healthcare, airport security, archaeology, manufacturing, and quality assurance. Nowadays, vast amounts of 3D models are being developed and are distributed freely or commercially on the Internet. 3D objects consist of geometric and topological information, and their compact representation is an important step towards a variety of computer vision applications, particularly matching and retrieval in a database of 3D models. The first step in 3D object matching usually involves

finding a reliable shape descriptor or skeletal graph which will encode efficiently the 3D shape information. Skeletonization aims at reducing the dimensionality of a 3D shape while preserving its topology [7, 27].

Most 3D shape representation techniques proposed in the literature of computer graphics and computer vision are based on geometric and topological representations which represent the features of an object [30, 31, 28, 29]. For example, Siddiqi *et al.* [28] introduced a shock detection approach based on singularity theory to generate a skeletal shape model. Also, Siddiqi *et al.* [32] recently proposed a directed acyclic graph representation for 3D retrieval using medial surfaces. This approach uses the geometric information associated with each graph node along with an eigenvalue labeling of the adjacency matrix of the subgraph rooted at that node. Damon [33] presented an elegant algorithm for decomposing the medial axis into irreducible medial components which are attached to each other along fin curves. The mathematical and algorithmic aspects of medial representations are further explored in [34]. Cornea *et al.* [35] devised a 3D matching framework for 3D volumetric objects using a many-to-many matching algorithm. This algorithm is based on establishing correspondences among two skeletal representations via distribution-based matching in metric spaces. Hassouna *et al.* [36] proposed a level set based framework for robust centerline extraction of 2D shapes and 3D volumetric objects. This approach is based on the gradient vector flow and uses a wave propagation technique, which identifies the curve skeletons as the wave points of maximum positive curvatures. Tagliasacchi *et al.* [37] introduced a curve skeleton extraction algorithm from imperfect point clouds. A major drawback of curve skeletons is that they cannot capture general shape features, such as surface ridges, and are essentially restricted to objects which resemble connected tubular forms.

An alternative to feature-based representations is global methods, which represent a 3D object by a global measure or shape distribution defined on the surface of the object [38, 39, 40]. Ankerst *et al.* [38] uses shape histograms to analyze the similarity of 3D molecular surfaces. These histograms are built from uniformly distributed surface points taken from the molecular surfaces, and are defined on concentric shells and sectors around the centroid of the surface. Osada *et al.* [39] proposed a global approach for computing shape signatures of arbitrary 3D models. The key idea is to represent an object by a global histogram based on the Euclidean distance defined on the surface of an object. Kazhdan *et al.* [40] proposed a rotation invariant spherical harmonic representation that transforms rotation dependent shape descriptors into rotation independent ones. Chen *et al.* [41] presented a lightfield descriptor for 3D object retrieval by comparing ten silhouettes of the 3D shape obtained from ten viewing angles distributed uniformly on the viewing enclosing sphere. The dissimilarity of two shapes is computed as the minimal distance obtained by rotating the viewing sphere of one lightfield descriptor relative to the other lightfield descriptor. The computation of this

descriptor is, however, significantly time consuming compared to spherical harmonics [42].

The approach proposed in this chapter aims at representing 3D objects with topological coding. Topology represents the connectedness of a shape and enables parts of shapes, which are connected, to be mapped and drawn equivalently. One of the key mathematical tools used to study the topology of spaces is Morse theory which is the study of the relationship between functions on a space and the shape of the space. Morse studies the properties of a Morse function which has only nondegenerate singular points [7], and it describes the topology changes of the level sets of this function at those singularities. Regular or noncritical points do not affect the number or genus of the components of the level sets. It can be shown that Morse functions are dense and stable in the set of all smooth functions, that is the structure of nondegenerate singularities does not change under small perturbations [7]. A Morse theoretic representation that captures topological properties of objects is the so-called Reeb graph representation proposed in [30]. The vertices of the Reeb graph are the singular points of a Morse function defined on the surface of a 3D object [7, 30]. The height function-based approach may lead to the extraction of an unbounded number of critical points, except in the case of triangle meshes where the number of critical points is bounded by the number of mesh vertices. This limitation has been addressed in [60] by introducing a fair Morse function that produces the least possible number of critical points. Since the level sets of the height function are horizontal planes perpendicular to the height axis, the weakness of such Reeb graphs is that they are not invariant to rotation. Lazarus *et al.* [31] used the geodesic distance from a manually chosen source point as a Morse function to compute their extracted graphs which they referred to as *level set diagrams*. Hilaga *et al.* [29] used the geodesic distance from point to point on a surface to overcome the problem of automatic extraction of the source point. The geodesic integral is, however, computed using a selected (typically small) random subset of points on the surface, which may lead to inaccuracies in terms of effectively capturing the topological structure of the surface. Moreover, another disadvantage of using the geodesic distance is its sensitivity to topological changes. That is, modifying the shape connectivity may significantly alter the shortest paths between feature points, resulting in significant changes of the geodesic distance. Tierny *et al.* [61] presented a structural oriented Reeb graph based method for partial 3D shape retrieval. Partial similarity between two shapes is then evaluated by computing a variant of their maximum common sub-graph. Gebal *et al.* [44] proposed a surface signature based on the heat kernel and applied it to mesh skeletonization and segmentation. Aouada *et al.* [45] proposed a topological Reeb graph skeleton using an intrinsic global geodesic function defined on the surface of a 3D object. This approach decomposes a shape into primitives, and then a detailed geometric information is added by tracking the evolution of Morse's function level curves along each primitive. A

detailed overview of the mathematical properties of Reeb graphs and their applications to shape analysis is presented in [46]. Pascucci *et al.* [47] introduced a robust method for fast Reeb graph computation that is able to handle non-manifold meshes. Also, Patane *et al.* [48] proposed an efficient Reeb graph computation algorithm by studying the evolution of the level sets only at the saddle points of a Morse function. More recently, Reuter [64] introduced a Morse-theoretic method for shape segmentation and registration using the topological features of Laplace-Beltrami eigenfunctions. These eigenfunctions are computed with a cubic finite element method on triangular meshes. Moreover, the level curves of the first eigenfunction may be used to extract the skeletal Reeb graph of a 3D mesh.

In this chapter, we propose an invariant skeletal Reeb graph for 3D object representation using a normalized mixture distance function. The key idea is to identify and encode regions of topological interest of a 3D object in the Morse-theoretic framework [6, 51]. The main motivation behind using the distance function is its rotational invariance, which makes it more adapted to object recognition than the Morse height function. Using this skeletal graph as a shape signature, we also extend to 3D the idea of path similarity skeleton graph matching by comparing the relative shortest paths between the skeleton endpoints.

The rest of this chapter is organized as follows. In Section 3.2, we propose a normalized mixture distance function-based approach to construct invariant skeletal Reeb graphs of 3D objects. Section 3.3 introduces a 3D extension of the idea of path similarity skeleton graph matching by comparing the relative shortest paths between the skeleton endpoints. In Section 3.4, we present experimental results for topological coding using the mixture distance function-based skeletal graph, and show its robustness to noise, mesh decimation, and invariance to rigid motion transformations. Then, we demonstrate the feasibility of the proposed skeletal Reeb graph as a shape signature for 3D object matching and retrieval.

3.2 PROPOSED REEB GRAPH APPROACH

The concept of distance is of paramount importance to topology, with the actual numeric values being of less importance. In fact, topologists often use a distance function, but the attributed numerical values have only secondary meaning. To illustrate this, suppose we are given an object in the ordinary 3D space, and a point outside the object, and the question is: does the object come arbitrarily close to this reference point? this may be stated as: is the point a boundary point of the object? “Arbitrarily close” means that if one imagines a ball around the reference point, then the ball contains some points belonging to the object no matter how small the ball is.

Denote by $\mathbf{V} = (\mathbf{p}_1 \ \mathbf{p}_2 \ \dots \ \mathbf{p}_m)^T$ the $m \times 3$ mesh vertex matrix having as rows the coordinates of the

mesh vertices

$$\mathbf{V} = \begin{pmatrix} x_1 & y_1 & z_1 \\ x_2 & y_2 & z_2 \\ \vdots & \vdots & \vdots \\ x_m & y_m & z_m \end{pmatrix} \in \mathbb{R}^{m \times 3}, \quad (3.1)$$

where $\mathbf{p}_i = (x_i, y_i, z_i)^T \in \mathcal{V}$.

Let $\mathbf{c} = (\bar{x}, \bar{y}, \bar{z})^T$ be the centroid of the triangle mesh, that is \mathbf{c} is the center of the minimal enclosing sphere of the mesh vertices \mathcal{V} . We define the $m \times 3$ centered vertex matrix as

$$\begin{aligned} V_{\mathbf{c}} &= (\mathbf{p}_1 - \mathbf{c} \ \mathbf{p}_2 - \mathbf{c} \ \dots \ \mathbf{p}_m - \mathbf{c})^T \\ &= \begin{pmatrix} x_1 - \bar{x} & y_1 - \bar{y} & z_1 - \bar{z} \\ x_2 - \bar{x} & y_2 - \bar{y} & z_2 - \bar{z} \\ \vdots & \vdots & \vdots \\ x_m - \bar{x} & y_m - \bar{y} & z_m - \bar{z} \end{pmatrix}. \end{aligned} \quad (3.2)$$

The Euclidean distance function of \mathbb{M} to \mathbf{c} is defined as

$$d_{\mathbf{c}}^{euc} : \mathbb{M} \rightarrow \mathbb{R} \quad \text{such that} \quad d_{\mathbf{c}}^{euc}(\mathbf{p}) = \|\mathbf{p} - \mathbf{c}\|^2, \quad (3.3)$$

and it can be easily shown that it is rotation and translation invariant.

Let $A = m(V_{\mathbf{c}}^T V_{\mathbf{c}})^{-1}$, we define the affine distance function as follows

$$d_{\mathbf{c}}^{aff} : \mathbb{M} \rightarrow \mathbb{R} \quad \text{such that}$$

$$d_{\mathbf{c}}^{aff}(\mathbf{p}) = \|\mathbf{p} - \mathbf{c}\|_A^2 = (\mathbf{p} - \mathbf{c})^T A (\mathbf{p} - \mathbf{c}), \quad (3.4)$$

and it can be shown that it is invariant to affine transformations [52]. It is worth pointing out that A is the covariance matrix of the surface points about their centroid. Thus, the affine distance reduces to the Mahalanobis distance with respect to this matrix. In addition, the matrix A is always well-defined for nondegenerate 3D shapes (i.e. when \mathbb{M} is not a point or a plane).

The level sets of the Euclidean and affine invariant distances are illustrated in Figure 3.1.

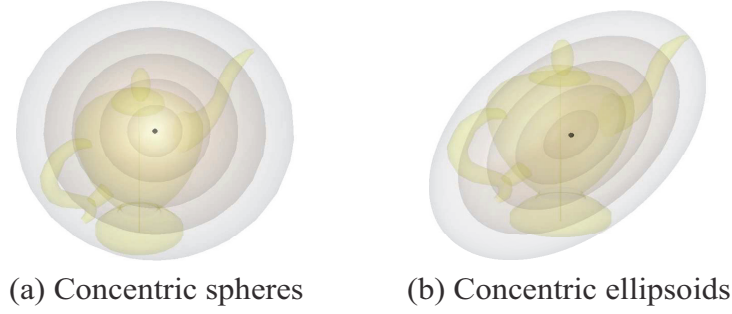


FIGURE 3.1: Level sets of the (a) Euclidean and (b) affine invariant distances.

3.2.1 MIXTURE DISTANCE FUNCTION

We define the mixture distance function as a convex combination of the Euclidean and the affine distance functions:

$d_{\mathbf{c}} : \mathbb{M} \rightarrow \mathbb{R}$ such that

$$d_{\mathbf{c}}(\mathbf{p}) = \lambda \|\mathbf{p} - \mathbf{c}\|^2 + (1 - \lambda) \|\mathbf{p} - \mathbf{c}\|_A^2, \quad (3.5)$$

where $\lambda \in (0, 1)$ is a mixture parameter that needs to be estimated or chosen *a priori*.

From the invariance properties of the Euclidean and affine distance functions, it is easy to verify that the mixture distance function is invariant to orthogonal and translation transformations.

3.2.2 MORSE-THEORETIC ANALYSIS OF THE MIXTURE DISTANCE FUNCTION

A surface \mathbb{M} may be defined locally in parametric form by a Monge patch $\mathbf{r} : \mathbb{M} \rightarrow \mathbb{R}^3$ such that the neighborhood of each point $\mathbf{p} = \mathbf{r}(x, y) \in \mathbb{M}$ may be defined as a graph of a function $u : \Omega \subset \mathbb{R}^2 \rightarrow \mathbb{R}$. In other words, there exists $(x, y) \in \Omega$ such that $\mathbf{p} = \mathbf{r}(x, y) = (x, y, u(x, y))$. Hence the mixture distance function may be expressed as

$$d_{\mathbf{c}}(\mathbf{r}(x, y)) = \lambda \|\mathbf{r}(x, y) - \mathbf{c}\|^2 + (1 - \lambda) \|\mathbf{r}(x, y) - \mathbf{c}\|_A^2. \quad (3.6)$$

Taking the derivatives of $d_{\mathbf{c}}$ with respect to x and y , the first partial derivatives are given by $d_x = \mathbf{r}_x^T B_\lambda (\mathbf{r} - \mathbf{c})$ and $d_y = \mathbf{r}_y^T B_\lambda (\mathbf{r} - \mathbf{c})$, where $B_\lambda = \lambda I_3 + (1 - \lambda)(A + A^T)$, and I_3 is the 3×3 identity matrix. Thus $d_{\mathbf{c}}$ has a critical point at $\mathbf{p} = \mathbf{r}(x, y)$ if and only if $B_\lambda (\mathbf{p} - \mathbf{c})$ is orthogonal to \mathbb{M} at \mathbf{p} , or equivalently $\mathbf{c} - \mathbf{r}(x, y)$ is parallel to the surface normal \mathbf{N} . Therefore

$$\mathbf{c} = \mathbf{p} + \alpha B_\lambda^{-1} \mathbf{N} = \mathbf{r}(x, y) + \alpha B_\lambda^{-1} \mathbf{N}, \quad (3.7)$$

where α is a constant.

On the other hand, the second order partial derivatives of $d_{\mathcal{C}}$ at a critical point are given by

$$\begin{aligned} d_{xx} &= \mathbf{r}_x^T B_\lambda \mathbf{r}_x + \mathbf{r}_{xx}^T B_\lambda (\mathbf{r} - \mathbf{c}) = \mathbf{r}_x^T B_\lambda \mathbf{r}_x - \alpha \mathbf{r}_{xx}^T \mathbf{N} \\ d_{yy} &= \mathbf{r}_y^T B_\lambda \mathbf{r}_y + \mathbf{r}_{yy}^T B_\lambda (\mathbf{r} - \mathbf{c}) = \mathbf{r}_y^T B_\lambda \mathbf{r}_y - \alpha \mathbf{r}_{yy}^T \mathbf{N} \\ d_{xy} &= \mathbf{r}_x^T B_\lambda \mathbf{r}_y + \mathbf{r}_{xy}^T B_\lambda (\mathbf{r} - \mathbf{c}) = \mathbf{r}_x^T B_\lambda \mathbf{r}_y - \alpha \mathbf{r}_{xy}^T \mathbf{N}. \end{aligned}$$

Hence, the Hessian matrix is given by $\nabla^2 d = \mathbf{I} - \alpha \mathbf{II}$, where \mathbf{I} and \mathbf{II} denote the first and second fundamental forms [5] with respect to the orthogonal basis

$$\{\sqrt{B_\lambda} \mathbf{r}_x, \sqrt{B_\lambda} \mathbf{r}_y\}.$$

A degenerate critical point of the mixture distance function satisfies $\det(\nabla^2 d_{\mathcal{C}}) = 0$ if and only if

$$\det(\nabla^2 d_{\mathcal{C}}) = 1/\alpha^2 = \kappa_1 \kappa_2, \quad (3.8)$$

where κ_1 and κ_2 are the principal curvatures [5]. A point $\mathbf{p} \in \mathbb{M}$ is therefore a degenerate critical point of the mixture distance function $d_{\mathcal{C}}$ if and only if \mathbf{c} is a focal point of (\mathbb{M}, \mathbf{p}) , that is $\mathbf{c} = \mathbf{p} + \kappa_1^{-1} \mathbf{N}$ or $\mathbf{c} = \mathbf{p} + \kappa_2^{-1} \mathbf{N}$. If \mathbf{c} is the origin of the coordinate system, then it is clear that \mathbf{c} is not a focal point and hence $d_{\mathcal{C}}$ has no degenerate critical points. In addition, the Morse index of a nondegenerate critical point of the mixture distance function $d_{\mathcal{C}}$ is equal to the number of focal points of (\mathbb{M}, \mathbf{p}) which lie on the segment from \mathbf{p} to \mathbf{c} . This can be shown using the Hessian matrix $\nabla^2 d_{\mathcal{C}}$ since the number of its negative eigenvalues is equal to the number of eigenvalues of the second fundamental form matrix \mathbf{II} (assuming that the first fundamental form \mathbf{I} is the identity matrix) which are $\geq 1/\alpha$.

3.2.3 PROPERTIES OF THE MIXTURE DISTANCE FUNCTION

For simplicity we consider the centroid \mathbf{c} of the surface \mathbb{M} to be the origin of the Euclidean coordinate system. Hence the mixture distance function becomes

$$d(\mathbf{p}) = \lambda \|\mathbf{p}\|^2 + (1 - \lambda) \|\mathbf{p}\|_A^2. \quad (3.9)$$

Note that for $\ell > 0$, the level sets $\{\mathbf{p} \in \mathbb{M} : d(\mathbf{p}) = \ell\}$ of the mixture distance function are concentric convex combination of quadrics. The key idea behind using the mixture distance function is to track the changes in topology as we cross a surface singularity. In the first step, we start with a convex combination of quadrics having a sufficiently small level value ℓ , and centered as the barycenter of the underlying surface, then we evolve this convex combination of quadrics by increasing the level value so that we will have a set

of concentric convex combination of quadrics covering the entire surface. The most important properties of the mixture distance function are:

- (i) the level sets $\{\mathbf{p} \in \mathbb{M} : d(\mathbf{p}) = \ell\}$ of the distance function are concentric convex combination of quadrics.
- (ii) a 3D object can be reconstructed if we know its intersections with these concentric convex combination of quadrics.
- (iii) the mixture distance function is rotation and translation invariant and can be easily normalized to achieve scale invariance as shown next.

3.2.4 NORMALIZED MIXTURE DISTANCE FUNCTION

We define the normalized mixture distance function as

$$\tilde{d}(\mathbf{p}) = \frac{d(\mathbf{p}) - d_{\min}}{d_{\max} - d_{\min}}, \quad \forall \mathbf{p} \in \mathcal{V}, \quad (3.10)$$

where $d_{\min} = \min d(\mathbf{p})$ and $d_{\max} = \max d(\mathbf{p})$.

It can easily be shown that the normalized mixture distance function is scale-invariant, that is $\tilde{d}(s\mathbf{p}) = \tilde{d}(\mathbf{p})$, where $s \in \mathbb{R}$. Even with the normalized form, calculating the mixture distance function for a given surface point is simple and computationally inexpensive.

3.2.5 PROPOSED SKELETONIZATION ALGORITHM

The main algorithmic steps of the mixture distance-based Reeb graph are described in Algorithm 4. In Figure 3.2 the work flow of the proposed skeletonization algorithm is shown at selected steps to illustrate the skeletal graph extraction, where the VerticesSet and NodeSet are marked as green and red points respectively.

The complexity of the proposed skeletonization algorithm can be determined as follows. Computing the centroid and the normalized mixture distance function for a 3D triangle mesh with m vertices takes $\mathcal{O}(m)$ time. Constructing the nodes and edges of the skeletal graph requires calculating the connected component of triangles and hence also takes $\mathcal{O}(m)$ time. The overall complexity is, therefore, $\mathcal{O}(m)$, which shows an improvement over geodesic function based Reeb graphs with complexity $\mathcal{O}(m \log m)$. This computational cost can be further improved [29] using Patane *et al.*'s Reeb-graph extraction algorithm [48], which has

Algorithm 1 Proposed skeletonization approach

```
1: Find the centroid of  $c$  of the 3D mesh  $\mathbb{M} = (\mathcal{V}, \mathcal{T})$ 
2: Find the maximum distance  $d_{\max} = \max d_{\mathbf{c}}(\mathbf{p}), \forall \mathbf{p} \in \mathcal{V}$ 
3: for ( $k = 1$  to  $R$ )
4:    $d(k) = k * d_{\max}/R$ ;  $\Leftarrow R$  is the resolution parameter
5:  $\text{VerticesSet}_p[0,1] = \text{setIntersect}(\mathbb{M}, 1)$ ;  $\Leftarrow$  Find vertices subset of  $\mathbb{M}$  from  $c$  to  $d(1)$ 
6:  $\text{NodeSet}_p = \text{centroid}(\text{VerticesSet}_p[0,1](n))$ ;  $\Leftarrow$  Assign a node to each connected component at its centroid.
7: Connect  $c$  and  $\text{NodeSet}_p$ 
8: for  $k = 2$  to  $R$  do
9:    $\text{VerticesSet}_c[k-1, k] = \text{setIntersect}(\mathbb{M}, k-1, k)$ ;  $\Leftarrow$  Find intersection of  $\mathbb{M}$  from distance  $d(k-1)$  to  $d(k)$ 
10:  for each component  $\text{VerticesSet}_c[k-1, k](n)$  do
11:     $\text{NodeSet}_c = \text{centroid}(\text{VerticesSet}_c[k-1, k](n))$ 
12:    for each connected portion do
13:      Connect  $\text{NodeSet}_c$  and  $\text{NodeSet}_p$ 
14:    end for
15:  end for
16:   $\text{NodeSet}_p = \text{NodeSet}_c$ 
17:   $\text{VerticesSet}_p = \text{VerticesSet}_c$ 
18: end for
```

a computational complexity of $\mathcal{O}(sm)$, where s is the number of saddle points of the underlying Morse function. Thus, a considerable computational improvement is expected when $s < \log m$.

It is important to understand how the mixture distance function relates to topology and Morse theory. The intersection of a 3D object with a growing convex combination of quadrics results in connected components on the object surface (see Figure 3.3(a)). The critical points of the surface, which define its topology, correspond to distance levels, at which there is a change in number of connected components (see Figure 3.3(b)). This change in the number of connected components reflects the changes in topology of a 3D shape, particularly, branching and merging or holes within as shown in Figure 3.3(b).

3.3 REEB GRAPH MATCHING

In this section, we extend to 3D the idea of path similarity skeleton graph matching by comparing the relative shortest paths between the skeleton endpoints [55]. Bai *et al.* [55] algorithm uses the similarity of the shortest paths between each pair of skeleton endpoints to establish a correspondence relation of the endpoints in different graphs. These shortest path-based methods, however, were essentially proposed to tackle the problem of 2D shape matching. Our proposed approach, which only considers the shortest skeletal paths between skeleton endpoints, is focused on skeletal graph matching for 3D objects. The proposed

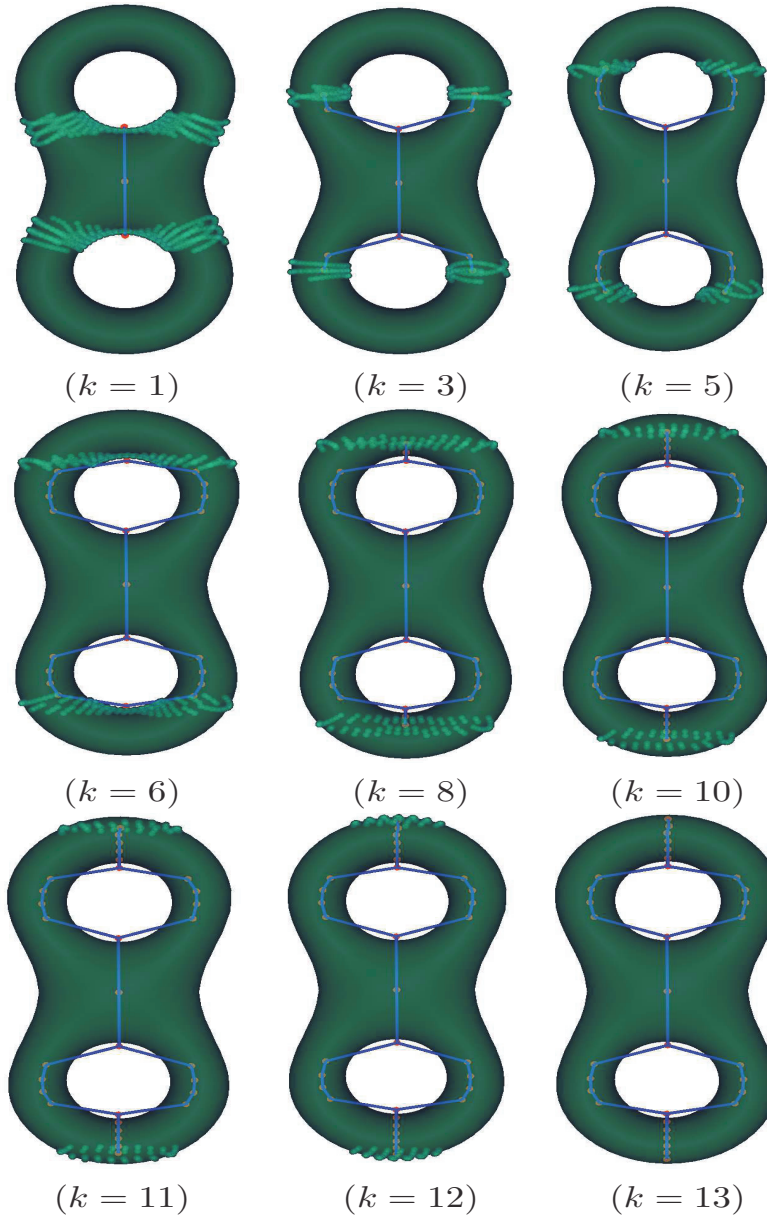


FIGURE 3.2: Mixture distance-based Reeb graph extraction at various steps $k = 1, \dots, 13$.

skeleton graph matching is based on the dissimilarity of the shortest paths between the endpoints of the skeletal Reeb graph. A skeleton endpoint refers to the skeleton node that is connected by only one edge as shown in Figure 3.4. It is worth pointing out that endpoints are the salient points of the skeleton and can be seen as visual parts of the original 3D shape [55]. In the same vein as [55], considering only the shortest skeletal paths between endpoints would help avoid the instability problem of the skeleton junction points (i.e. points having three or more adjacent points) and also to make our proposed method more robust

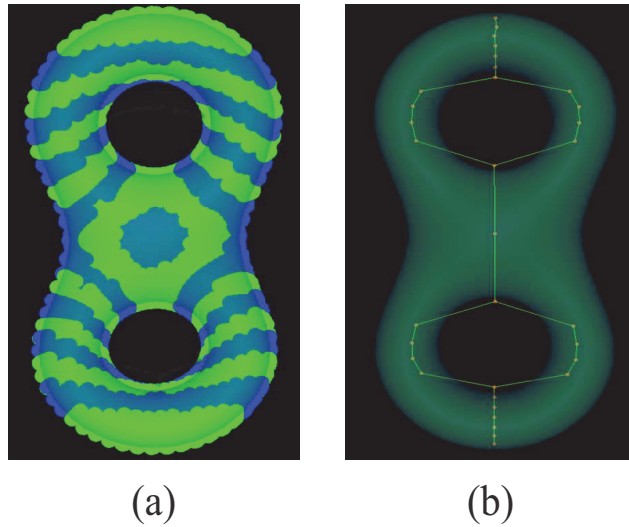


FIGURE 3.3: (a) Connected components and (b) skeletal graph of a double torus.

to shape deformation. The shortest path between each endpoint and all other endpoints of the skeleton provides an important endpoint feature that will be incorporated into our matching dissimilarity measure.

Our proposed skeleton graph matching approach is based on the assumption that similar skeletons have a similar structure of their endpoints. It is common that the skeletons of similar 3D shapes may have different structures of junction nodes. Similar to [55], one of the major advantages of the proposed method is that it does not require that the graphs be converted to trees prior to finding the correspondence, as this conversion may result in the loss of important structural information and, consequently, negatively influence the 3D object recognition result.

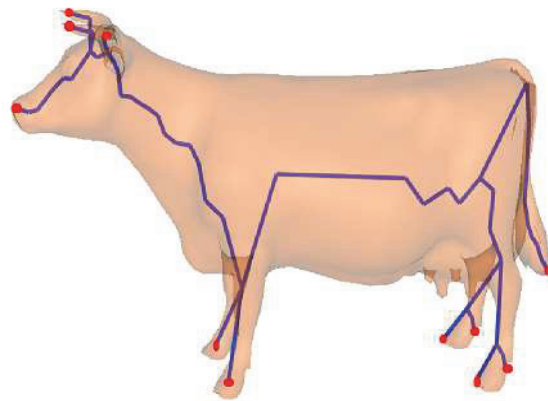


FIGURE 3.4: The 3D cow's Reeb graph and its skeleton endpoints (red color).

In contrast to existing methods for skeleton matching, our proposed approach focuses on the dissimilarity between the shortest paths connecting the skeleton endpoints. We use the shortest paths between endpoints to establish a correspondence relation of the endpoints in different skeletal Reeb graphs. It is worth noting that the idea of using of shortest paths in skeletal graph matching and classification has been previously explored in the literature. For example, Demirci *et al.* [53] proposed transforming the graphs into points in a low-dimensional geometric space using low-distortion graph embedding techniques. Each point in the embedding space corresponds to a node in the original graphs. The distance in the embedding space reflects the shortest-path distance in the original graphs in order to keep topological relations. Ling *et al.* [54] proposed using the inner-distance to build shape descriptors that are robust to articulation and capture part structure. The inner-distance is defined as the length of the shortest path between landmark points within the shape silhouette.

After generating the 3D shape skeleton, our next step is to develop a robust approach for skeletal graph matching. To this end, we match any two Reeb graphs by establishing a correspondence of their endpoints. Then, we apply a pruning algorithm [56] to remove non-salient nodes from the skeleton graph. The proposed matching method consists of two main steps. The first step, which we refer to as indexing, reduces the number of skeletons to be compared with. In the second step, we match the Reeb graphs by applying a dissimilarity measure to retrieve the closest 3D model. These two steps are explained in more details in the following subsections.

3.3.1 INDEXING

A linear search through a database of 3D models is inefficient for large databases, as it requires comparing the query object to each model in the database and selecting the closest one [32]. Therefore, the goal is to apply an efficient indexing mechanism to narrow the search scope in a small set of objects that are most probably similar to the query object. Using our skeletonization algorithm, we may formulate the indexing problem as finding skeletons whose topological structures are similar to the query skeleton. It is important to note that similar shapes will have the same skeleton even if they are subject to some deformation or transformation. Moreover, these skeletons will have the same number of endpoints.

Thus, in our indexing mechanism we use the number of skeleton endpoints as the base for indexing, with an error rate of 2 or 3 nodes, meaning that for two skeletons to be in the same index group they should have the same number of endpoints. However, due to noise there might be a difference of 1 or 2 nodes at most, as a result of the pruning process.

3.3.2 ENDPOINTS CORRESPONDENCE

After applying the indexing mechanism, the next step is to match the skeletons. Our proposed matching method considers both topological and geometrical features of the matched 3D models. We assign to each endpoint in the Reeb graph (query or model) some features that may help identify the closet endpoint in the other skeletal graph. Thus, our skeleton graph matching problem may be reduced to finding the best correspondence between the endpoints in the query and the endpoints in the model. This can be achieved by minimum weight matching of the two sets of endpoints. A dissimilarity measure between the set of endpoints in both query and model skeletons is used. Therefore, the matching problem aims at finding the best correspondence between the query skeleton endpoints and the database skeletons endpoints. Two endpoints are said to be in close correspondence if the dissimilarity measure between their endpoints has a smaller value. In other words, the matching problem is now reduced to finding the maximum correspondence, minimum weight matching of the two sets of endpoints. The endpoints correspondence process is shown in Algorithm 2.

Algorithm 2 Endpoints correspondence

Let $E = (\mathbf{v}_i)_{i=1,\dots,n_1}$ and $\tilde{E} = (\tilde{\mathbf{v}}_j)_{j=1,\dots,n_2}$ be two sets of endpoints.

For each endpoint $\mathbf{v}_i \in E$:

- 1: Compute a dissimilarity measure between \mathbf{v}_i and all the nodes in \tilde{E}
- 2: Find the node $\tilde{\mathbf{v}}_j$ with the minimum dissimilarity and assign its correspondence to \mathbf{v}_i
- 3: Delete \mathbf{v}_i and $\tilde{\mathbf{v}}_j$ from the list of nodes in E and \tilde{E} , respectively

Repeat steps 1-3 for all nodes in E until one of the node sets E or \tilde{E} is empty

3.3.3 MATCHING ENDPOINTS USING SKELETON PATHS

Endpoint Features

When generating the skeletal Reeb graph of a 3D shape we assign three features to each endpoint of the skeleton. The first feature is the relative node area, which is equal to the area of the neighboring triangles of the endpoint divided by the total area of the 3D model. This feature provides important information about the endpoint as sometimes the skeletons of two models may look similar, albeit their shapes are completely different. Thus, adding this feature to an endpoint will help discriminate between endpoints based on the original 3D shape and not just its skeleton. The reason behind using the relative area is due to its invariance to scaling. The second feature assigned to an endpoint is the relative node path, which is equal to the sum of shortest path distances from each endpoint to all other endpoints of the skeleton (see Figure 3.5(b)) divided

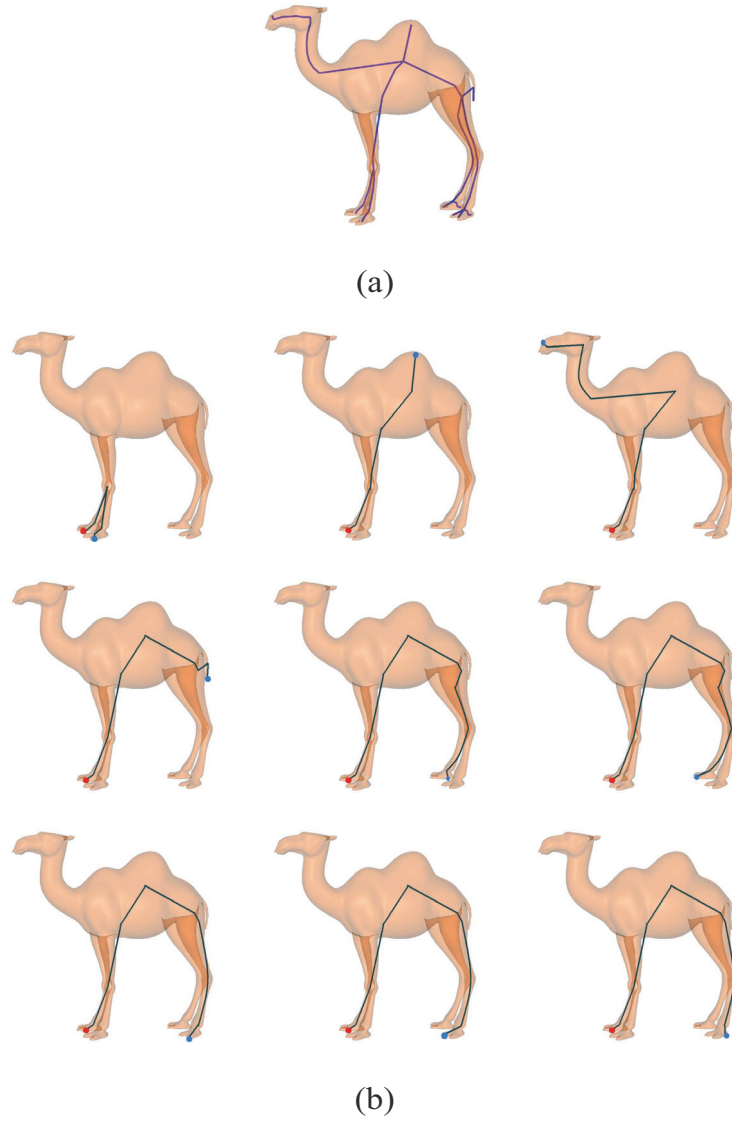


FIGURE 3.5: (a) Camel's Reeb graph. (b) Shortest paths between pairs of endpoints on the skeleton.

by the sum of the shortest paths from the mesh centroid (root node) to each endpoint. And the third feature is the relative centroid path, which is the shortest path distance from the mesh centroid to each endpoint (see Figure 3.6), divided by the sum of the shortest paths from the mesh centroid to all endpoints.

Endpoints dissimilarity

Let \mathbb{M} and $\tilde{\mathbb{M}}$ be two 3D objects with skeletal Reeb graphs G and \tilde{G} , respectively. And denote by $E = (v_i)_{i=1, \dots, n_1}$ and $\tilde{E} = (\tilde{v}_j)_{j=1, \dots, n_2}$ the skeleton endpoints sets of G and \tilde{G} , respectively. We define the

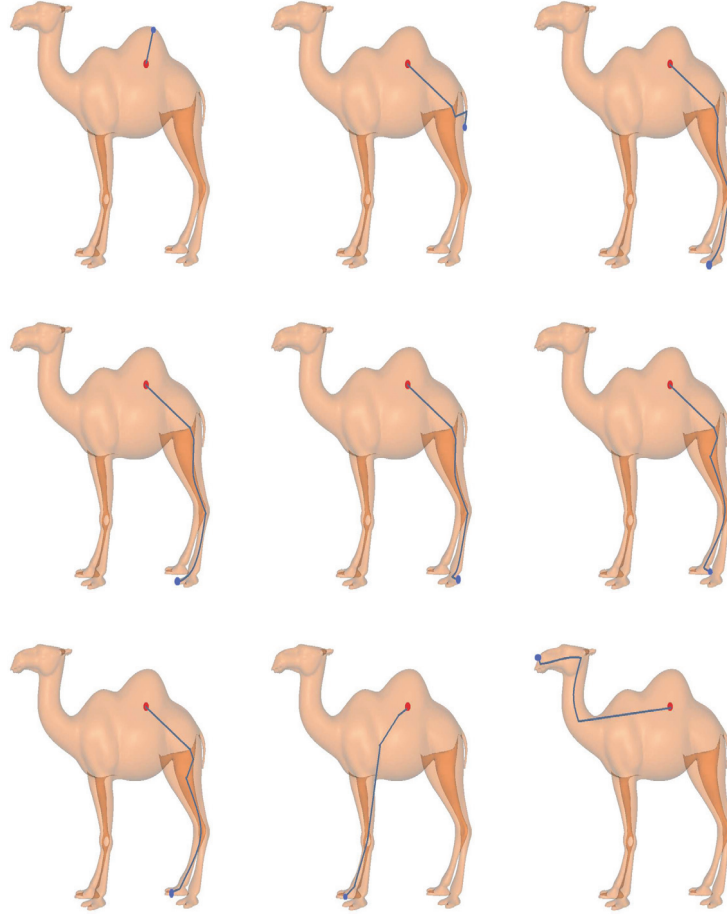


FIGURE 3.6: Shortest paths between the mesh centroid and an endpoint on the skeleton.

dissimilarity measure between two endpoints \mathbf{v}_i and $\tilde{\mathbf{v}}_j$ as follows:

$$\Phi(\mathbf{v}_i, \tilde{\mathbf{v}}_j) = [(a_i - \tilde{a}_j)^2 + (d\mathbf{v}_i - d\tilde{\mathbf{v}}_j)^2 + (d\mathbf{c}_i - d\tilde{\mathbf{c}}_j)^2]^{1/2}, \quad (3.11)$$

where

- a_i and \tilde{a}_j are the relative node areas of \mathbf{v}_i and $\tilde{\mathbf{v}}_j$
- $d\mathbf{v}_i = \sum_{k=1}^{n_1} \text{dist}(\mathbf{v}_i, \mathbf{v}_k) / \sum_{k=1}^{n_1} \text{dist}(\mathbf{c}, \mathbf{v}_k)$ and $d\tilde{\mathbf{v}}_j = \sum_{k=1}^{n_2} \text{dist}(\tilde{\mathbf{v}}_j, \tilde{\mathbf{v}}_k) / \sum_{k=1}^{n_2} \text{dist}(\tilde{\mathbf{c}}, \tilde{\mathbf{v}}_k)$ are the relative node paths of \mathbf{v}_i and $\tilde{\mathbf{v}}_j$
- $d\mathbf{c}_i = \text{dist}(\mathbf{c}, \mathbf{v}_i) / \sum_{k=1}^{n_1} \text{dist}(\mathbf{c}, \mathbf{v}_k)$ and $d\tilde{\mathbf{c}}_j = \text{dist}(\tilde{\mathbf{c}}, \tilde{\mathbf{v}}_j) / \sum_{k=1}^{n_2} \text{dist}(\tilde{\mathbf{c}}, \tilde{\mathbf{v}}_k)$ are the relative centroid paths of \mathbf{v}_i and $\tilde{\mathbf{v}}_j$
- \mathbf{c} and $\tilde{\mathbf{c}}$ are the centroids of \mathbb{M} and $\tilde{\mathbb{M}}$, respectively

- $dist(\cdot, \cdot)$ denotes the Dijkstra’s shortest path distance.

Therefore, the dissimilarity between two skeletal Reeb graphs may be defined as:

$$\mathcal{D}(G, \tilde{G}) = \sum_{i=1}^{n_1} \sum_{j=1}^{n_2} \Phi(\mathbf{v}_i, \tilde{\mathbf{v}}_j). \quad (3.12)$$

The main algorithmic steps of the proposed graph matching approach are described in more details in Algorithm 3.

Algorithm 3 Proposed graph matching approach

Given two 3D objects \mathbb{M} and $\tilde{\mathbb{M}}$

- 1: Generate the skeletal Reeb graphs G and \tilde{G} of \mathbb{M} and $\tilde{\mathbb{M}}$, respectively
 - 2: Apply graph pruning to remove non-salient nodes
 - 3: Find the skeleton endpoints sets $E = (\mathbf{v}_i)_{i=1, \dots, n_1}$ and $\tilde{E} = (\tilde{\mathbf{v}}_j)_{j=1, \dots, n_2}$ of G and \tilde{G} , respectively
 - 4: **for** all endpoints (\mathbf{v}_i) and $(\tilde{\mathbf{v}}_j)$ **do**
 - 5: Compute the relative node areas a_i and \tilde{a}_j of \mathbf{v}_i and $\tilde{\mathbf{v}}_j$, respectively
 - 6: Compute the relative node paths $d\mathbf{v}_i$ and $d\tilde{\mathbf{v}}_j$
 - 7: Compute the relative centroid paths $d\mathbf{c}_i$ and $d\tilde{\mathbf{c}}_j$
 - 8: **end for**
 - 9: Apply Algorithm 2 to find the correspondence between G and \tilde{G}
 - 10: Compute the dissimilarity $\mathcal{D}(G, \tilde{G})$ given by Eq. (3.12).
-

It is important to point out that our matching algorithm is largely motivated by [55]. However, a significant difference with our algorithm is the novel choice of features that we assigned to the skeleton endpoints as well as the dissimilarity measure between these endpoints. More precisely, steps 4-to-10 of Algorithm 3 show a major difference between our proposed approach and Bai *et al.*’s algorithm [55].

Let ℓ denote the number of skeleton endpoints. Using Patane *et al.*’s Reeb-graph extraction algorithm [48], the computational complexity of our approach may be reduced to $\mathcal{O}(sm + \ell^2)$ when $s < \log m$. In addition, the number of skeleton endpoints ℓ is relatively small.

3.4 EXPERIMENTAL RESULTS

The results of the proposed Reeb graph path dissimilarity method are presented in this section. We start by presenting examples of mixture distance-based Reeb graphs for 3D shapes using the proposed skeletonization algorithm. In all the experimental results, we used a data-dependent mixture distance parameter λ given by:

$$\lambda = \max(\|\mathbf{p}_i\|^2 / (\|\mathbf{p}_i\|^2 + \|\mathbf{p}_i\|_A^2)).$$

In other words, the value of λ is computed automatically from all the vertices of the 3D shape. Also, The resolution parameter R was set to $R = 22$. To justify the purpose of introducing a weighted distance, Figure 3.7 shows the skeletonization results using the affine and mixture distance. As can be seen, the mixture distance function-based approach provides more accurate results while preserving topology.

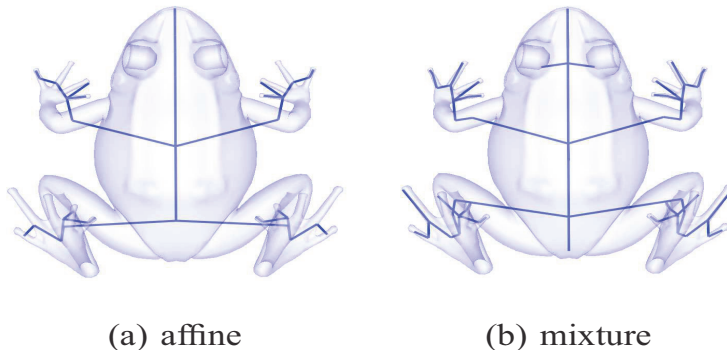


FIGURE 3.7: Skeletal graphs using affine and mixture distance functions.

Using the skeletonization algorithm described in Section 3, we constructed the Reeb graphs of several 3D models as shown in Figure 3.8. The results clearly indicate the robustness of the proposed of the skeletonization algorithm in extracting skeletal Reeb graphs of 3D objects.

Next, we show the robustness of the proposed skeletal graph to noise and to mesh decimation as well as its invariance to Euclidean transformations.

3.4.1 ROBUSTNESS TO NOISE

To test the performance of the proposed skeletonization algorithm in the presence of noise, we generated the noisy 3D model by adding artificial noise to each coordinate of the mesh vertices according to the noise model given by $\bar{\mathbf{p}}_i = \mathbf{p}_i + \sigma \mathbf{N}$, where \mathbf{p}_i and $\bar{\mathbf{p}}_i$ are the original and noisy mesh vertices respectively, \mathbf{N} is a Gaussian noise process with zero mean and unit variance, and σ is a variable parameter that specifies the amount of noise to be added and it is usually chosen experimentally. For the noisy double torus shown in Figure 3.9(a), we used a value of σ equal to $\sigma = 3.5 \min(\max(\|\mathbf{p}_i - \mathbf{p}_j\|)), \forall i, j = 1, \dots, m$.

Figure 3.9(b) depicts the extracted mixture distance-based Reeb graph using the proposed algorithm, and it evidently shows a good preservation of the mesh topological structure. The result is very similar to what one would expect in the case of the skeleton graph of the noise-free double torus shown in Figure 3.3(b).

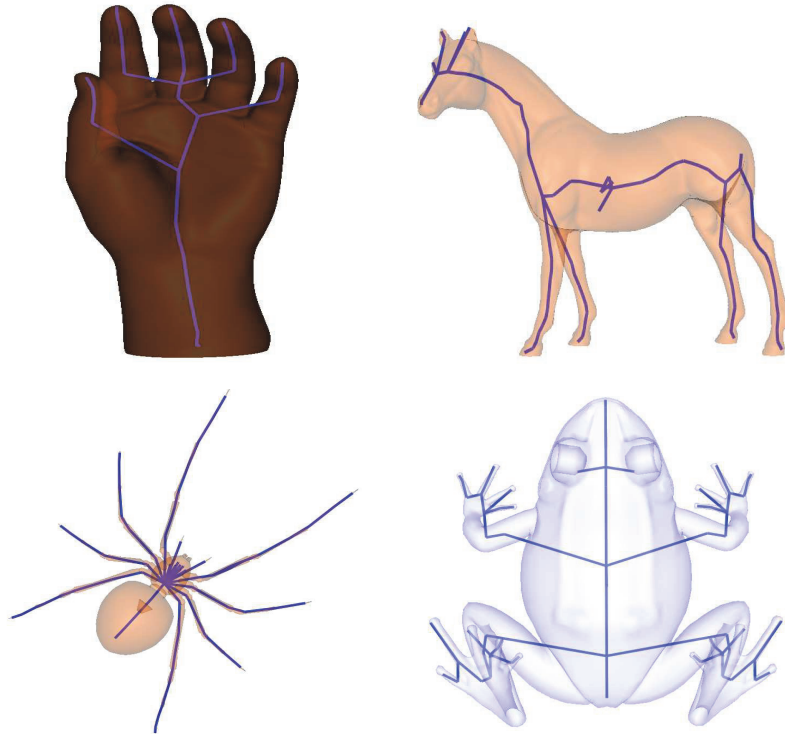


FIGURE 3.8: Mixture distance-based Reeb graphs of different 3D models.

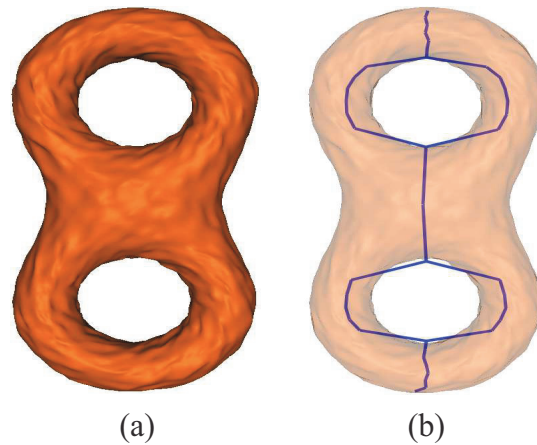


FIGURE 3.9: (a) Noisy double torus and its (b) mixture distance-based Reeb graph.

3.4.2 ROBUSTNESS TO MESH DECIMATION

The goal of mesh decimation is to reduce the total number of mesh faces while closely approximating the original surface. The original model shown in Figure 3.10(a) contains 25600 triangles. The two decimated heart meshes shown in Figure 3.10(b) and Figure 3.10(c) contain 6400 and 1600 triangular faces, respec-

tively. Note that the skeletal Reeb graphs of the decimated meshes are excellent approximations of the original model graph.

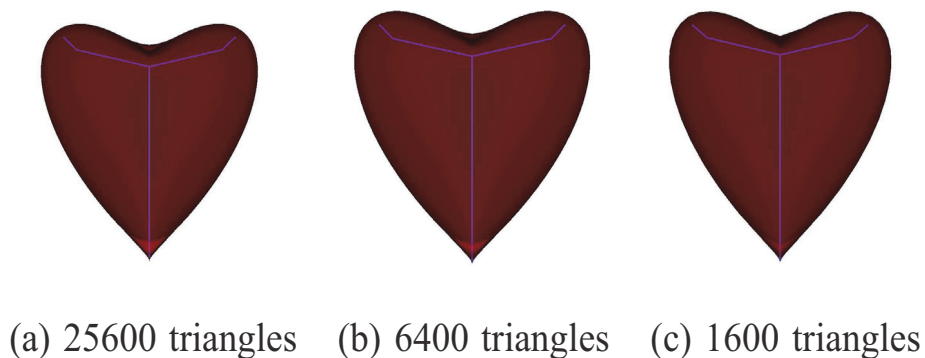


FIGURE 3.10: Mixture distance-based Reeb graph under mesh decimation.

3.4.3 INVARIANCE TO ROTATION, TRANSLATION, AND SCALING

Figure 3.11(a) and Figure 3.11(b) shows that rotating a 3D spider model, prior to the construction of the skeletal graph, does not change the critical points of the mixture distance function. Their corresponding mixture distance-based Reeb graphs are identical. Moreover, by introducing the normalized mixture distance function, we guarantee that different dimensions of the same object are modeled with the same skeletal graph. Figure 3.11(c) shows the skeletal graph of the 3D spider model scaled by a factor of 2 but at the same resolution as Figure 3.11(a).

3.4.4 MATCHING AND RETRIEVAL RESULTS

We tested the performance of the proposed matching algorithm using the McGill Shape Benchmark [71]. This publicly available benchmark database provides a 3D shape repository, which contains 255 objects that are divided into ten categories, namely, ‘Ants’, ‘Crabs’, ‘Spectacles’, ‘Hands’, ‘Humans’, ‘Octopuses’, ‘Pliers’, ‘Snakes’, ‘Spiders’, and ‘Teddy Bears’. Sample models from this database are shown in Figure 3.12.

The McGill’s database objects are represented by voxel grids as well as by triangle meshes. Table 3.1 shows that the proposed approach yields correct matching results, where a low value (displayed in boldface for emphasis) of the dissimilarity measure indicates that the objects are more similar.

We also compared our approach with spherical harmonics (SH) [40] and medial surfaces (MS) [32]. The results show that our method achieve better retrieval results than the spherical harmonic approach as

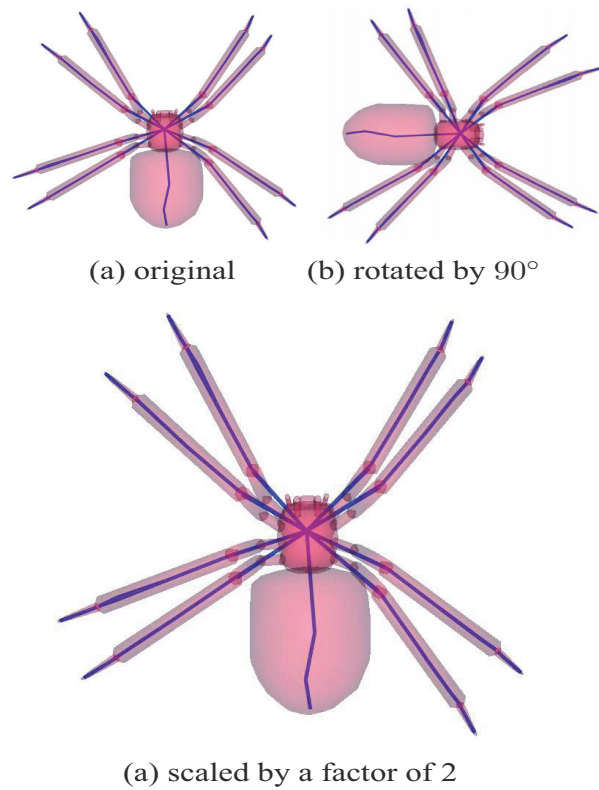


FIGURE 3.11: Illustration of skeletal Reeb graph invariance to rotation and scaling.

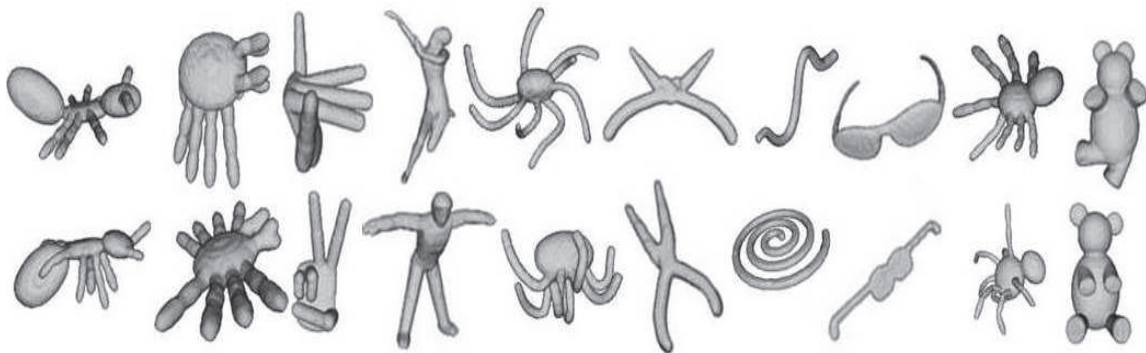


FIGURE 3.12: Sample shapes from McGill Articulated Shape Database. Only two shapes for each of the 10 classes are shown.

shown in Table 3.2, where the top ten retrieved 3D objects are displayed (top-to-bottom). As can be seen in Table 3.2, the proposed approach returns correct results whereas the spherical harmonics method yields poor retrieval results (columns 2, 4, and 6).

To carry out comparison experiments on the entire benchmark of articulated 3D objects, we evaluated the

retrieval performance of the proposed approach using the standard information retrieval evaluation measure of precision *versus* recall curve, where

$$\text{precision} = \frac{\text{No. relevant objects retrieved}}{\text{Total No. objects retrieved}}$$

and

$$\text{recall} = \frac{\text{No. relevant objects retrieved}}{\text{Total No. relevant objects in the collection}}.$$

A precision-recall curve that is shifted upwards and to the right indicates superior performance. It is evident from Figure 3.13 that our method significantly outperforms spherical harmonics and medial surfaces.

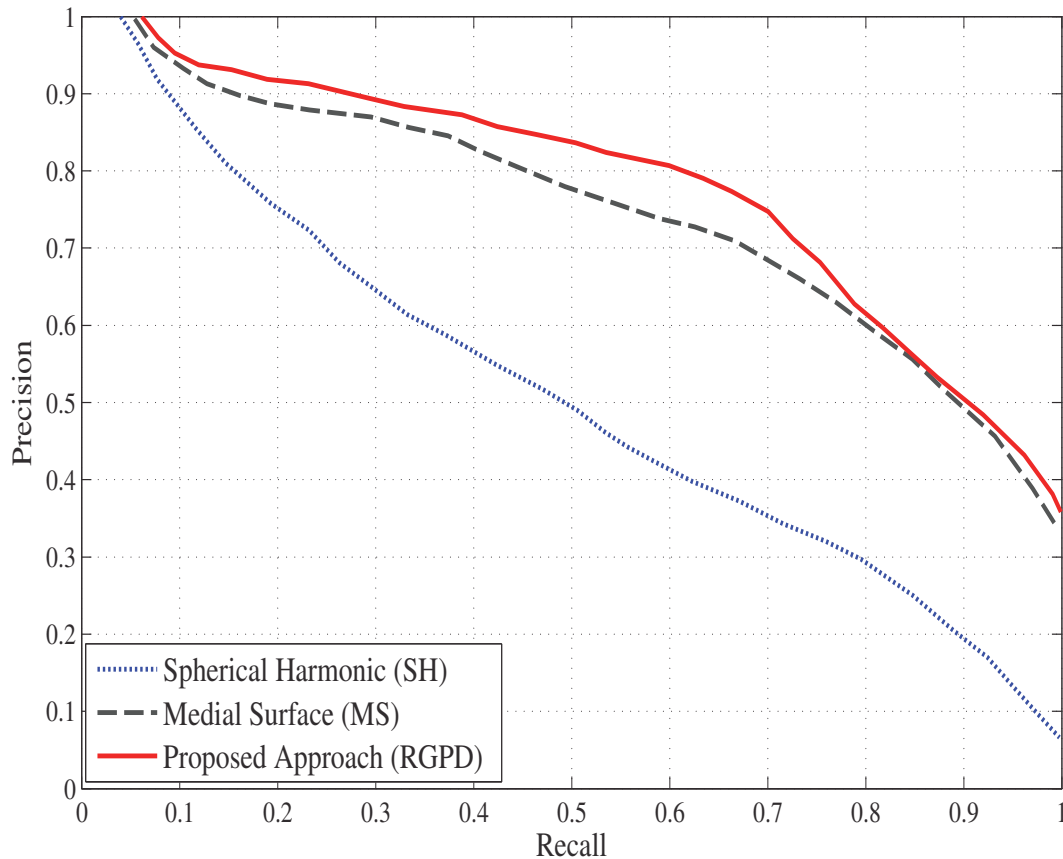


FIGURE 3.13: Precision vs. Recall curves for spherical harmonics (SH), medial surfaces (MS), and proposed RGPD approach using the McGill Shape Benchmark [71].

Finally, we tested the performance of the proposed algorithm on the Princeton Shape Benchmark [72]. As can be seen in Table 3.3, the proposed approach shows superior performance over spherical harmonics, where the top five retrieved 3D objects are displayed (top-to-bottom).

$\mathcal{D}(M, \tilde{M})$							
	0.0275	0.1130	0.1216	0.0278	0.1583	0.1146	0.1137
	0.1103	0.0025	0.1131	0.1156	0.1255	0.1632	0.1522
	0.1231	0.1143	0.0123	0.0355	0.1137	0.1223	0.1312
	0.0187	0.1167	0.1332	0.0169	0.1136	0.1174	0.1225
	0.1333	0.1244	0.1141	0.1335	0.0077	0.1158	0.1623
	0.1135	0.1463	0.1311	0.1624	0.1243	0.0041	0.1473
	0.1145	0.1247	0.1445	0.1193	0.1533	0.1776	0.0093

TABLE 3.1: Matching results using proposed Reeb graph path dissimilarity (RGPD). Each object in the database is matched against all the other objects in the database. Each cell shows the dissimilarity measure between two objects selected from the database. The smallest value corresponds to the correct match.

Query					
					
Retrieved Objects					
RGPD	SH	RGPD	SH	RGPD	SH
					
					
					
					
					
					
					
					
					
					

TABLE 3.2: Retrieval results using the McGill Shape Benchmark. The query shapes are shown in the second row. The top ten retrieved objects (top-to-bottom) using spherical harmonics (SH) and our proposed Reeb graph path dissimilarity (RGPD) are shown in rows 5 to 14.

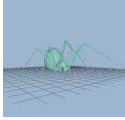
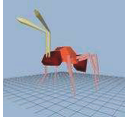
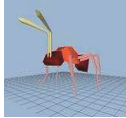
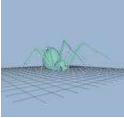
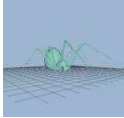
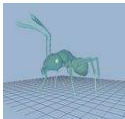
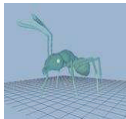
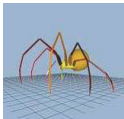
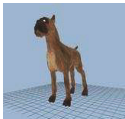
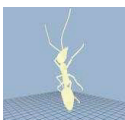
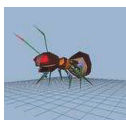
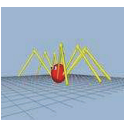
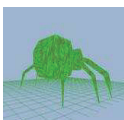
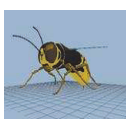
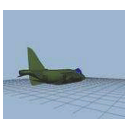
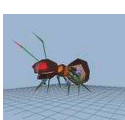
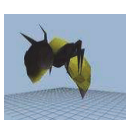
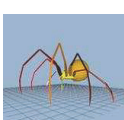
Query					
					
Retrieved Objects					
RGPD	SH	RGPD	SH	RGPD	SH
					
					
					
					
					

TABLE 3.3: Retrieval results using the Princeton Shape Benchmark. The query shapes are shown in the second row. The top five retrieved objects (top-to-bottom) using spherical harmonics (SH) and our proposed Reeb graph path dissimilarity (RGPD) are shown in rows 5 to 9.

SPECTRAL SKELETON FOR 3D OBJECT MATCHING AND RETRIEVAL

In this Chapter, we describe a skeletal graph for 3D object matching and retrieval. This skeleton is constructed from the second eigenfunction of the Laplace-Beltrami operator defined on the surface of the 3D object. Using the generalized eigenvalue decomposition, a matrix computational framework based on the finite element method is presented to compute the spectrum of the Laplace-Beltrami operator. We also introduce a robust matching method by comparing the shortest paths between the skeleton endpoints. The experimental results demonstrate the feasibility of the spectral skeleton in 3D object matching and retrieval.

4.1 INTRODUCTION

In light of the latest software, hardware and computing advancements, 3D technology has grown beyond being a buzzword. Today, 3D technology has become an essential part of the modern lifestyle and is gaining momentum rapidly, from consumer demand for in-home 3D television experiences to far-reaching positive implications for healthcare through the use of advanced 3D medical imaging systems aimed at improving patient outcomes and expanding their clinical practice.

The importance of 3D shape recognition is irrupting due to the difficulty in processing information expeditiously without its recognition. With the increasing use of 3D scanners and as a result of emerging multimedia computing technologies, vast databases of 3D models are distributed freely or commercially on the World Wide Web. The availability and widespread usage of such large databases coupled with the need to explore 3D models in depth as well as in breadth has sparked the need to organize and search these

vast data collections, retrieve the most relevant selections, and permit them to be effectively reused. 3D objects consist of geometric and topological information, and their compact representation is an important step towards a variety of computer vision applications, particularly matching and retrieval in a database of 3D models. The first step in 3D object matching usually involves finding a reliable shape descriptor or skeletal graph, which will encode efficiently the 3D shape information. Skeletonization aims at reducing the dimensionality of a 3D shape while preserving its topology [7, 27]. Unlike text documents, 3D models are not easily retrieved due to the variability of their shapes. Attempting to find a 3D model using textual annotation and a conventional text-based search engine would not work properly in many cases [57]. The annotations added by users depend on various factors, including language, culture, age, and gender. In contrast, content-based 3D shape retrieval methods, which typically use the shape properties of the 3D models to search for similar models, perform better than text-based methods [57].

The vast majority of 3D shape representation techniques proposed in the literature of computer graphics and computer vision are based on geometric and topological representations which represent the features of an object [30, 28, 29]. For example, Siddiqi *et al.* [28] introduced a shock detection approach based on singularity theory to generate a skeletal shape model. Also, Siddiqi *et al.* [32] proposed a directed acyclic graph representation for 3D retrieval using medial surfaces. This approach uses the geometric information associated with each graph node along with an eigenvalue labeling of the adjacency matrix of the subgraph rooted at that node. Cornea *et al.* [35] devised a 3D matching framework for 3D volumetric objects using a many-to-many matching algorithm. This algorithm is based on establishing correspondences among two skeletal representations via distribution-based matching in metric spaces. Hassouna *et al.* [36] proposed a level set based framework for robust centerline extraction of 2D shapes and 3D volumetric objects. This approach is based on the gradient vector flow and uses a wave propagation technique, which identifies the curve skeletons as the wave points of maximum positive curvatures. Tagliasacchi *et al.* [37] introduced a curve skeleton extraction algorithm from imperfect point clouds. A major drawback of curve skeletons is that they cannot capture general shape features, such as surface ridges, and are essentially restricted to objects which resemble connected tubular forms.

An alternative to feature-based representations is global methods, which represent a 3D object by a global measure or shape distribution defined on the surface of the object [38, 39, 40, 58]. Ankerst *et al.* [38] uses shape histograms to analyze the similarity of 3D molecular surfaces. These histograms are built from uniformly distributed surface points taken from the molecular surfaces, and are defined on concentric shells and sectors around the centroid of the surface. Osada *et al.* [39] proposed a global approach for comput-

ing shape signatures of arbitrary 3D models. The key idea is to represent an object by a global histogram based on the Euclidean distance defined on the surface of an object. More recently, Ion *et al.* [59] proposed an articulation-insensitive shape matching approach by constructing histograms from the eccentricity transform using geodesic distances. Kazhdan *et al.* [40] proposed a rotation invariant spherical harmonic representation that transforms rotation dependent shape descriptors into rotation independent ones. Chen *et al.* [41] presented a lightfield descriptor for 3D object retrieval by comparing ten silhouettes of the 3D shape obtained from ten viewing angles distributed uniformly on the viewing enclosing sphere. The dissimilarity of two shapes is computed as the minimal distance obtained by rotating the viewing sphere of one lightfield descriptor relative to the other lightfield descriptor. The computation of this descriptor is, however, significantly time consuming compared to spherical harmonics [42].

In this chapter, we describe a spectral skeletonization approach that aims at representing 3D objects with topological coding, which we refer to as *Spectral Reeb Graph* (SRG). Topology represents the connectedness of a shape and enables parts of shapes, which are connected, to be mapped and drawn equivalently. One of the key mathematical tools used to study the topology of spaces is *Morse theory*, which is the study of the relationship between functions on a space and the shape of the space. Morse theory studies the properties of a Morse function which has only nondegenerate singular points [6, 7], and it describes the topology changes of the level sets of this function at those singularities. Regular or noncritical points do not affect the number or genus of the components of the level sets. It can be shown that Morse functions are dense and stable in the set of all smooth functions, that is the structure of nondegenerate singularities does not change under small perturbations [6, 7]. A Morse theoretic representation that captures topological properties of objects is the so-called *Reeb graph* representation proposed in [30], which is based on the Morse height function. The vertices of the Reeb graph are the singular points of a Morse function defined on the surface of a 3D object [7, 30]. The height function-based approach may lead to the extraction of an unbounded number of critical points, except in the case of triangle meshes where the number of critical points is bounded by the number of mesh vertices. This limitation has been addressed in [60] by introducing a fair Morse function that produces the least possible number of critical points. Since the level sets of the height function are horizontal planes perpendicular to the height axis, the weakness of such Reeb graphs is that they are not invariant to rotation. Hilaga *et al.* [29] used the geodesic distance from point to point on a surface to overcome the problem of automatic extraction of the source point. The geodesic integral is, however, computed using a selected (typically small) random subset of points on the surface, which may lead to inaccuracies in terms of effectively capturing the topological structure of the surface. Moreover, another disadvantage of using the

geodesic distance is its sensitivity to topological changes. That is, modifying the shape connectivity may significantly alter the shortest paths between feature points, resulting in significant changes of the geodesic distance. Tierny *et al.* [61] presented a structural oriented Reeb graph based method for partial 3D shape retrieval. Partial similarity between two shapes is then evaluated by computing a variant of their maximum common sub-graph. Gebal *et al.* [44] proposed a surface signature based on the heat kernel and applied it to mesh skeletonization and segmentation. Aouada *et al.* [45] proposed a topological Reeb graph skeleton using an intrinsic global geodesic function defined on the surface of a 3D object. This approach decomposes a shape into primitives, and then detailed geometric information is added by tracking the evolution of Morse's function level curves along each primitive. A detailed overview of the mathematical properties of Reeb graphs and their applications to shape analysis is presented in [46]. Pascucci *et al.* [47] introduced a robust method for fast Reeb graph computation that is able to handle non-manifold meshes. Also, Patane *et al.* [48] proposed an efficient Reeb graph computation algorithm by studying the evolution of the level sets only at the saddle points of a Morse function.

More recently, there has been a surge of interest in the spectral analysis of the Laplace-Beltrami operator, resulting in many applications to object recognition and in particular manifold learning [62] and shape analysis [63, 64, 65, 66]. It is worth pointing out that spherical harmonics [40] are nothing but the Laplace-Beltrami eigenfunctions on the sphere. Reuter [64] introduced a Morse-theoretic method for shape segmentation and registration using the topological features of Laplace-Beltrami eigenfunctions. These eigenfunctions are computed via a cubic finite element method on triangular meshes, and are arranged in increasing order of their associated eigenvalues. Shi *et al.* [67] used the level curves of the second eigenfunction to construct the spectral Reeb graph of 3D neuroanatomical structures. In addition to having a nice geometric property of following the pattern of the overall shape of a 3D object, the second eigenfunction of the Laplace-Beltrami operator can capture the intrinsic structure of elongated shapes (e.g. hippocampus) and it is also invariant to isometric transformations. Moreover, the spectral Reeb graph is invariant to the pose of the shape [67].

Motivated by the aforementioned invariance properties of the second eigenfunction of the Laplace-Beltrami operator, we propose to use the spectral Reeb graph to construct the shape skeleton of a 3D object. The key idea is to identify and encode regions of topological interest of a 3D object in the Morse-theoretic framework. That is, the level sets (curves) of the second eigenfunction are computed (identified), then each level set (curve) is encoded as a skeleton node representing the centroid of the curve.

The rest of this chapter is organized as follows. In Section 4.2, we delineate the spectral Reeb graph of

a 3D object using the second eigenfunction of the Laplace-Beltrami operator, which is the intrinsic surface Laplacian. Section 4.3 briefly describes the path dissimilarity skeleton graph matching method by comparing the relative shortest paths between the skeleton endpoints. In Section 4.4, we present experimental results for topological coding using the spectral Reeb graph and we demonstrate the feasibility of this skeletal graph as a shape descriptor for 3D object matching and retrieval.

4.2 SPECTRAL REEB GRAPH

4.2.1 LAPLACE-BELTRAMI OPERATOR

Let \mathbb{M} be a smooth orientable 2-manifold embedded in \mathbb{R}^3 . A parametric representation of \mathbb{M} is a vector-valued function \mathbf{r} defined from a connected open set $\Omega \subseteq \mathbb{R}^2$ to \mathbb{R}^3 such that

$$\mathbf{r}(\mathbf{u}) = \begin{pmatrix} x_1(\mathbf{u}) \\ x_2(\mathbf{u}) \\ x_3(\mathbf{u}) \end{pmatrix} \quad (4.1)$$

where $\mathbf{u} = (u_1, u_2) \in \Omega$. At each point $\mathbf{p} = \mathbf{r}(\mathbf{u}) \in \mathbb{M}$, the coordinate vector fields (partial derivatives) $\mathbf{r}_1 = \partial\mathbf{r}/\partial u_1$ and $\mathbf{r}_2 = \partial\mathbf{r}/\partial u_2$ span the tangent space $T_{\mathbf{p}}\mathbb{M}$, that is $T_{\mathbf{p}}\mathbb{M} = \text{span}\{\mathbf{r}_1, \mathbf{r}_2\}$.

For each pair $\{\mathbf{r}_i, \mathbf{r}_j\}$ in the tangent space $T_{\mathbf{p}}\mathbb{M}$, the real-valued functions $g_{ij} : \Omega \rightarrow \mathbb{R}$ defined by the inner (dot) products $g_{ij} = \langle \mathbf{r}_i, \mathbf{r}_j \rangle$ form a Riemannian metric tensor $g = (g_{ij})$ on \mathbb{M} (called the usual metric on \mathbb{M}). That is, g is a symmetric 2×2 matrix given by

$$g = (g_{ij}) = \begin{pmatrix} g_{11} & g_{12} \\ g_{12} & g_{22} \end{pmatrix}, \quad (4.2)$$

which is also denoted as $ds^2 = \sum_{i,j=1}^2 g_{ij} du_i du_j$. The geometry obtained from such dot products is called Riemannian geometry. The Riemannian metric g makes it possible to define various geometric notions on a Riemannian manifold (\mathbb{M}, g) , such as angles, lengths of curves, geodesics, areas (or volumes), curvature, gradients of functions and divergence of vector fields. The metric tensor g is the analogous of the speed in the case of space curves, and determines all the intrinsic properties of the surface \mathbb{M} . These properties depend on the surface and do not depend on its embedding in space. Furthermore, the tensor g is invariant to rotation of the surface in space because it is defined in terms of inner products that are rotation invariant. The area of the manifold \mathbb{M} is given by

$$\text{area}(\mathbb{M}) = \int_{\mathbb{M}} d\mathbb{M} = \int_{\Omega} \sqrt{\det g(\mathbf{u})} d\mathbf{u} \quad (4.3)$$

where $\sqrt{\det g} = \sqrt{g_{11}g_{22} - g_{12}^2} = \|\mathbf{r}_1 \times \mathbf{r}_2\|$.

Given a twice-differentiable function $f : \mathbb{M} \rightarrow \mathbb{R}$, the Laplace-Beltrami operator is defined as

$$\Delta_{\mathbb{M}}f = -\operatorname{div}(\nabla_{\mathbb{M}}f) \quad (4.4)$$

where $\nabla_{\mathbb{M}}f$ is the intrinsic gradient vector field given by

$$\nabla_{\mathbb{M}}f = \sum_{i,j=1}^2 g^{ij} \frac{\partial f}{\partial u_j} \frac{\partial \mathbf{r}}{\partial u_i} \quad (4.5)$$

and g^{ij} denote the elements of the inverse of the metric tensor, that is $g^{-1} = (g^{ij})$.

Thus, the Laplace-Beltrami may be expressed as

$$\Delta_{\mathbb{M}}f = -\frac{1}{\sqrt{\det g}} \sum_{i,j=1}^2 \frac{\partial}{\partial u_i} \left(\sqrt{\det g} g^{ij} \frac{\partial f}{\partial u_j} \right). \quad (4.6)$$

Using the divergence theorem under the assumption of Neumann boundary conditions yields

$$\begin{aligned} \int_{\mathbb{M}} f_1(\mathbf{p}) \Delta_{\mathbb{M}}f_2(\mathbf{p}) d\mathbb{M} &= - \int_{\mathbb{M}} f_1(\mathbf{p}) \operatorname{div}(\nabla_{\mathbb{M}}f_2) d\mathbb{M} \\ &= \int_{\mathbb{M}} \langle \nabla_{\mathbb{M}}f_1(\mathbf{p}), \nabla_{\mathbb{M}}f_2(\mathbf{p}) \rangle d\mathbb{M} \end{aligned} \quad (4.7)$$

for any two differentiable functions f_1 and f_2 , where the dot product is taken in the tangent space of the manifold.

Let $L^2(\mathbb{M})$ be the space of square integrable functions on the manifold \mathbb{M} . The space $L^2(\mathbb{M})$ is endowed with inner product

$$\langle f_1, f_2 \rangle = \int_{\mathbb{M}} f_1(\mathbf{p}) f_2(\mathbf{p}) d\mathbb{M}. \quad (4.8)$$

An eigenfunction f of the Laplace-Beltrami operator satisfies $\Delta_{\mathbb{M}}f = \lambda f$, where λ is the corresponding eigenvalue. Moreover, the eigenfunctions of the Laplace-Beltrami operator are the critical points (vectors) of the Rayleigh-Ritz quotient, which is an energy functional defined as

$$\mathcal{R}(f) = \frac{\int_{\mathbb{M}} \|\nabla_{\mathbb{M}}f\|^2 d\mathbb{M}}{\int_{\mathbb{M}} \|f\|^2 d\mathbb{M}} \quad (4.9)$$

and the eigenvalues are the values of the functional \mathcal{R} at such critical points. Obviously, the infimum value $\lambda_1 = 0$ of $\mathcal{R}(f)$ is achieved for a constant function $f = \varphi_1$. Since $\Delta_{\mathbb{M}}$ is a Hermitian operator, the set of eigenvalues (spectrum) $\{\lambda_i, i = 1, 2, \dots, \infty\}$ of $\Delta_{\mathbb{M}}$ is an infinite discrete subset of \mathbb{R}^+ . These eigenvalues may be written in increasing order as $0 = \lambda_1 < \lambda_2 \leq \lambda_3 \leq \dots$, with corresponding eigenfunctions $\{\varphi_i, i = 1, \dots, \infty\}$. Moreover, the eigenfunctions of the Laplace-Beltrami operator form an orthogonal basis for the the space $L^2(\mathbb{M})$. That is, $\langle \varphi_i, \varphi_j \rangle = 0$ for $i \neq j$.

The second eigenvalue is given by

$$\lambda_2 = \inf_{f \perp \varphi_1} \mathcal{R}(f) \quad (4.10)$$

and φ_2 is its corresponding eigenfunction. Note that since φ_1 is a constant function, $f \perp \varphi_1$ implies $\langle f, \varphi_1 \rangle = 0$, which yields $\int_{\mathbb{M}} f d\mathbb{M} = 0$.

4.2.2 DISCRETIZATION USING FINITE ELEMENT METHOD

Let \mathbb{M} be a triangle mesh represented as $\mathbb{M} = (\mathcal{V}, \mathcal{E})$ or $\mathbb{M} = (\mathcal{V}, \mathcal{T})$, where $\mathcal{V} = \{v_1, \dots, v_m\}$ is the set of vertices, $\mathcal{E} = \{e_{ij}\}$ is the set of edges, and $\mathcal{T} = \{t_1, \dots, t_n\}$ is the set of triangles. Each edge e_{ij} (denoted by $[v_i, v_j]$ or simply $[i, j]$) connects a pair of vertices $\{v_i, v_j\}$. Two distinct vertices $v_i, v_j \in \mathcal{V}$ are adjacent (denoted by $v_i \sim v_j$ or simply $i \sim j$) if they are connected by an edge, i.e. $e_{ij} \in \mathcal{E}$. The neighborhood of a vertex v_i is the set $v_i^* = \{v_j \in \mathcal{V} : i \sim j\}$ as shown in Figure 4.1.

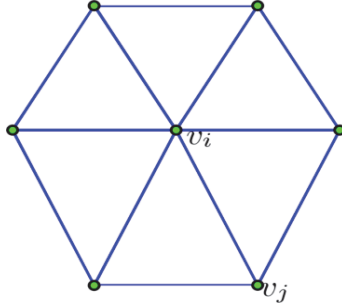


FIGURE 4.1: Illustration of a vertex neighborhood v_i^* .

Consider a triangle $t \in \mathcal{T}$ with vertices v_i, v_j and v_k , angles α, β and γ and sides a, b and c as illustrated in Figure 4.2. Then, according to Heron's formula, $\text{area}(t)$ is equal to

$$\text{area}(t) = \frac{1}{4} \sqrt{(a + (b + c))(a + (b - c))(c + (a - b))(c - (a - b))}, \quad (4.11)$$

where the length of the sides are arranged such that $a \geq b \geq c$.

We denote by $t_{[i,j]}^*$ the set of triangles sharing the edge $e_{ij} = [i, j]$, and by $\theta_k^{[i,j]}$ the angle in the triangle t_k opposite to the edge $[i, j]$.

Using the finite element method on triangle meshes [68, 69], it can be shown that the energy functional given in Eq. (4.9) may be expressed in matrix form as follows

$$\mathcal{R}(f) = \frac{f' Q f}{f' K f} \quad (4.12)$$

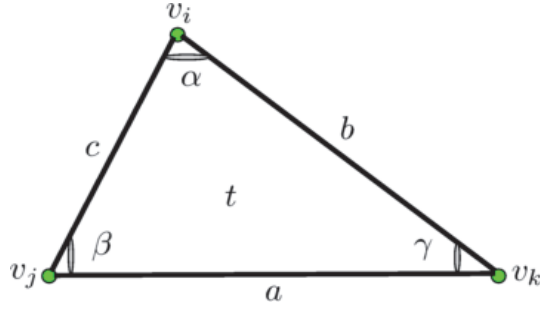


FIGURE 4.2: Illustration of $\text{area}(t)$ and $n(t)$.

where Q is an $m \times m$ matrix representing $\int_{\mathbb{M}} \|\nabla f\|^2 d\mathbb{M}$ is given by

$$Q = (Q_{ij}) = \begin{cases} \frac{1}{2} \sum_{\mathbf{v}_j \in \mathbf{v}_i^*} \sum_{\mathbf{t}_k \in \mathbf{t}_{[i,j]}^*} \cot \theta_k^{[i,j]} & \text{if } i = j \\ -\frac{1}{2} \sum_{\mathbf{t}_k \in \mathbf{t}_{[i,j]}^*} \cot \theta_k^{[i,j]} & \text{if } i \sim j \\ 0 & \text{otherwise} \end{cases} \quad (4.13)$$

and K is an $m \times m$ matrix representing $\int_{\mathbb{M}} \|f\|^2 d\mathbb{M}$ is given by

$$K = (K_{ij}) = \begin{cases} \frac{1}{12} \sum_{\mathbf{v}_j \in \mathbf{v}_i^*} \sum_{\mathbf{t}_k \in \mathbf{t}_{[i,j]}^*} \text{area}(\mathbf{t}_k) & \text{if } i = j \\ \frac{1}{12} \sum_{\mathbf{t}_k \in \mathbf{t}_{[i,j]}^*} \text{area}(\mathbf{t}_k) & \text{if } i \sim j \\ 0 & \text{otherwise.} \end{cases} \quad (4.14)$$

Both matrices Q and K are sparse. We refer to Q as the cotangent matrix, and K as the area matrix. Figure 4.3 shows a 3D tooth model and its sparse area and cotangent matrices Q and K .

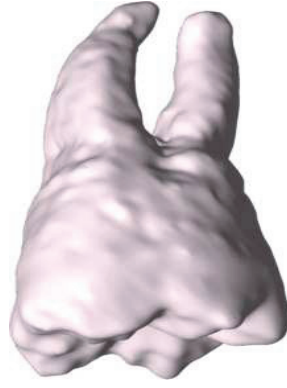
4.2.3 SPECTRAL SKELETON

The eigenvalues λ_i and corresponding eigenfunctions φ_i of the Laplace-Beltrami operator can be computed by solving the generalized eigenvalue problem:

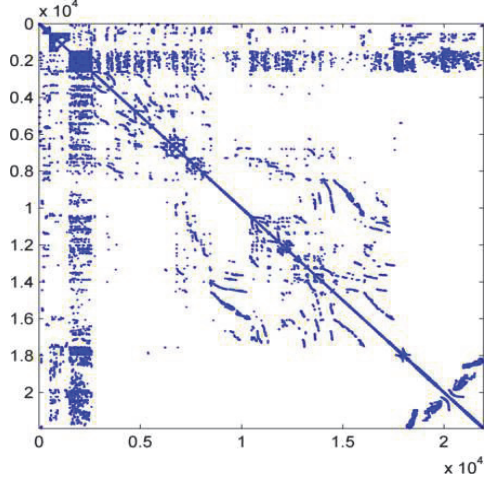
$$Q\varphi_i = \lambda_i K\varphi_i, \quad i = 1, 2, \dots, m \quad (4.15)$$

where φ_i is the unknown eigenfunction evaluated at m mesh vertices. That is, φ_i is an m -dimensional vector.

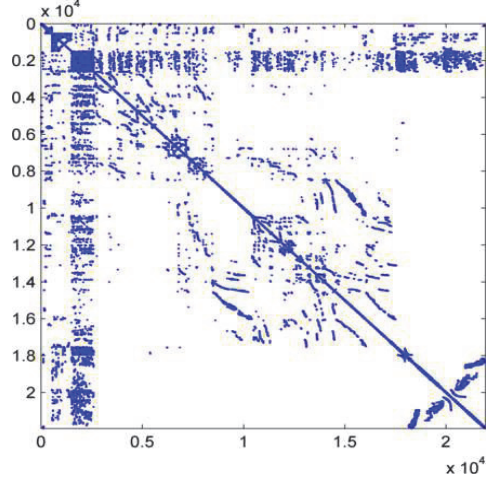
We may sort the eigenvalues in ascending order as $0 = \lambda_1 < \lambda_2 \leq \dots \leq \lambda_m$ and their corresponding eigenfunctions as $\varphi_1, \varphi_2, \dots, \varphi_m$, where each eigenfunction $\varphi_i = (\varphi_i(\mathbf{v}_1), \dots, \varphi_i(\mathbf{v}_m))'$ is an m -dimensional vector. Moreover, these eigenfunctions are orthogonal $\langle \varphi_i, \varphi_j \rangle_K = 0, \quad \forall i \neq j$, where



(a)



(b)



(c)

FIGURE 4.3: (a) 3D tooth model; (b) sparsity pattern plot of the cotangent matrix Q ; (c) sparsity pattern plot of the area matrix K

the orthogonality is defined in terms of the K -inner product. That is, $\langle \varphi_i, \varphi_j \rangle_K = \varphi_i' K \varphi_j$. We may normalize each eigenfunction φ_i by dividing each of its components with the K -norm $\|\varphi_i\|_K = \sqrt{\varphi_i' K \varphi_i}$, so that the eigenfunctions of the Laplace-Beltrami operator form an orthonormal basis. Thus, any function $f : \mathcal{V} \rightarrow \mathbb{R}$ (viewed as a column-vector of length m) on the triangle mesh $\mathbb{M} = (\mathcal{V}, \mathcal{T})$ can be expressed in terms of the eigenfunctions as follows

$$f = \sum_{i=1}^m \alpha_i \varphi_i, \quad \text{where} \quad \alpha_i = \langle f, \varphi_i \rangle \quad (4.16)$$

and the squared norm of f is given by $\|f\|^2 = \sum_{i=1}^m \alpha_i^2$.

Note that since the sum of each row in the matrix Q equals zero, the first eigenvalue λ_1 is zero and the corresponding eigenfunction φ_1 is a constant m -dimensional vector, that is $\varphi_1(v_i)$ is equal to a constant c for all $i = 1, \dots, m$. This constant eigenfunction is depicted in Figure 4.4(a), where each vertex v_i is

colored by a constant $c = \varphi_1(\mathbf{v}_i)$.

The second eigenvalue is given by

$$\lambda_2 = \inf_{f \perp \varphi_1} \frac{f'Qf}{f'Kf} \quad (4.17)$$

and $\varphi_2 = (\varphi_2(\mathbf{v}_1), \dots, \varphi_2(\mathbf{v}_m))'$ is its corresponding eigenfunction. This eigenfunction is displayed in Figure 4.4(b), where each vertex \mathbf{v}_i is colored by $\varphi_2(\mathbf{v}_i)$. The level curves of φ_2 are shown in Figure 4.4(c).

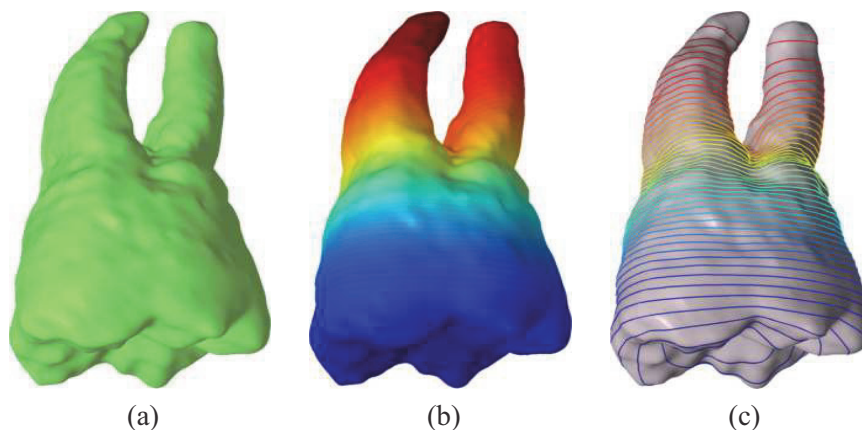


FIGURE 4.4: (a) 3D tooth model colored by φ_1 ; (b) tooth model colored by φ_2 ; (c) level sets of φ_2 .

On the other hand, Uhlenbeck [70] showed that the eigenfunctions of the Laplace-Beltrami operator are Morse functions on the interior of the domain of the operator. Consequently, this generic property of the eigenfunctions gives rise to constructing their associated Reeb graphs.

As shown in Figure 4.4(b) and Figure 4.5(a), the second eigenfunction of the Laplace-Beltrami operator captures well the overall shape of 3D objects. Motivated by the invariance properties of the second eigenfunction of the Laplace-Beltrami operator and also by its generic property as a Morse function, we propose to use the spectral Reeb graph to construct the shape skeleton of a 3D object as follows: First, the level sets (curves) of the second eigenfunction are computed (identified); then each level set (curve) is encoded as a skeleton node representing the centroid of the curve, as shown in Figure 4.5(c). The main algorithmic steps for computing the spectral Reeb graph are described in Algorithm 4.

4.3 SPECTRAL REEB GRAPH MATCHING

In this section, we use the same graph matching approach discussed in Chapter 3, which is based on the dissimilarity of the shortest paths between the endpoints of the skeletal Reeb graph. Recall that a skeleton

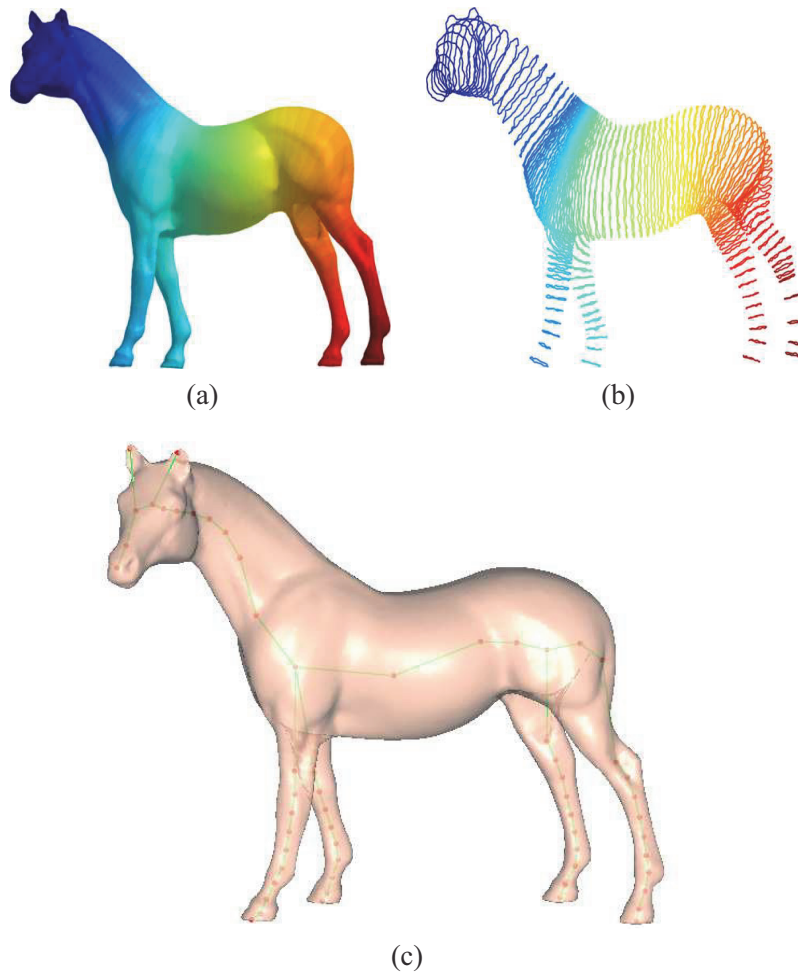


FIGURE 4.5: (a) 3D horse model colored by φ_2 ; (b) level sets of φ_2 ; (c) spectral Reeb graph.

endpoint is the skeleton node that is connected by only one edge as shown in Figure 4.6.

Similar to the previous chapter, we also assign three features to each endpoint of the skeleton. The first feature is the relative node area, which is equal to the area of the neighboring triangles of the endpoint divided by the total area of the 3D model. This feature provides important information about the endpoint as sometimes the skeletons of two models may look similar, albeit their shapes are completely different. Thus, adding this feature to an endpoint will help discriminate between endpoints based on the original 3D shape and not just its skeleton. The reason behind using the relative area is due to its invariance to scaling. The second feature assigned to an endpoint is the relative node path, which is equal to the sum of shortest path distances from each endpoint to all other endpoints of the skeleton (see Figure 4.7(b)) divided by the sum of the shortest paths from the mesh centroid (root node) to each endpoint. And the third feature is the relative centroid path, which is the shortest path distance from the mesh centroid to each endpoint (see Figure 4.8),

Algorithm 4 Proposed skeletonization approach

- 1: Compute the second eigenfunction φ_2 of the Laplace-Beltrami operator by solving the sparse generalized eigenvalue problem $Q\varphi_i = \lambda_i K\varphi_i$.
 - 2: Compute N level sets L_k ($k = 1, \dots, N$) of φ_2
 - 3: **for** each level set L_k ($k = 1$ to N)
 - 4: $\text{VerticesSet}_p[0,1] = \text{setIntersect}(\mathbb{M}, 1)$; \Leftarrow Find vertices (subset of the 3D mesh \mathbb{M}) of level set L_k
 - 5: $\text{NodeSet}_p = \text{centroid}(\text{VerticesSet}_p[0,1](n))$; \Leftarrow Assign a node to each connected component at its centroid.
 - 6: **for** $k = 2$ to N **do**
 - 7: $\text{VerticesSet}_c[k - 1, k] = \text{setIntersect}(\mathbb{M}, k - 1, k)$; \Leftarrow Find intersection of \mathbb{M} from region L_{k-1} to L_k
 - 8: **for** each component $\text{VerticesSet}_c[k - 1, k](n)$ **do**
 - 9: $\text{NodeSet}_c = \text{centroid}(\text{VerticesSet}_c[k - 1, k](n))$
 - 10: **for** each connected portion **do**
 - 11: Connect NodeSet_c and NodeSet_p
 - 12: **end for**
 - 13: **end for**
 - 14: $\text{NodeSet}_p = \text{NodeSet}_c$
 - 15: $\text{VerticesSet}_p = \text{VerticesSet}_c$
 - 16: **end for**
-

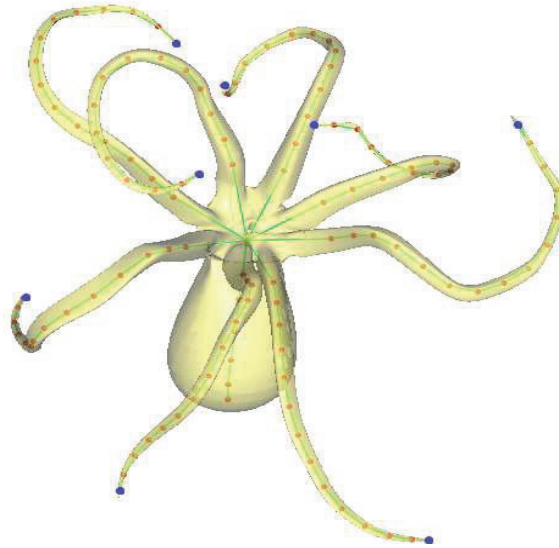


FIGURE 4.6: Spectral Reeb graph of 3D Octopus model and its skeleton endpoints shown in blue color.

divided by the sum of the shortest paths from the mesh centroid to all endpoints.

4.4 EXPERIMENTAL RESULTS

The results of the proposed framework are presented in this section. We start by demonstrating the robustness of the proposed skeletonization algorithm to noise. Figure 4.9 depicts the extracted skeletal Reeb graphs of a noise-free model and its noisy version using the proposed algorithm. It is evident the spectral skeletonization algorithm shows a good preservation of the mesh topological structure.

The results of the proposed spectral Reeb graph approach are presented in this section. We tested the performance of the proposed matching algorithm using the McGill Shape Benchmark [71]. Table 4.1 shows that the proposed approach yields correct matching results, where a low value (displayed in boldface for emphasis) of the dissimilarity measure indicates that the objects are more similar.

We also compared our approach with spherical harmonics (SH) [40], medial surfaces (MS) [32], and Reeb graph patch dissimilarity (RGPD) approach [80]. The results show that our method achieve better retrieval results than the spherical harmonics and medial surfaces as shown in Table 4.2, where the top ten retrieved 3D objects are displayed (top-to-bottom). As can be seen in Table 4.2, the proposed approach returns correct results whereas the spherical harmonics method yields poor retrieval results (columns 2, 4, and 6). Also, the proposed algorithm performs slightly better than the RGPD approach.

To carry out comparison experiments on the entire benchmark of articulated 3D objects, we evaluated the retrieval performance of the proposed approach using the standard information retrieval evaluation measure of precision *versus* recall curve. A precision-recall curve that is shifted upwards and to the right indicates superior performance. It is evident from Figure 4.10 that our method significantly outperforms spherical harmonics, medial surfaces, and the Reeb graph path dissimilarity approach.

Finally, we tested the performance of the proposed algorithm on the Princeton Shape Benchmark [72]. As can be seen in Table 4.3, the proposed approach shows superior performance over spherical harmonics, where the top five retrieved 3D objects are displayed (top-to-bottom).

$D(M, \tilde{M})$							
	0.0124	0.1127	0.1216	0.1258	0.1131	0.1344	0.1257
	0.1116	0.0073	0.1136	0.1297	0.1227	0.1124	0.1131
	0.1311	0.1142	0.0653	0.1356	0.1315	0.1171	0.1137
	0.1146	0.1329	0.1113	0.0055	0.1332	0.1621	0.1552
	0.1193	0.1248	0.1342	0.1421	0.1131	0.1572	0.1592
	0.1327	0.1109	0.1152	0.1474	0.11719	0.1021	0.1116
	0.1223	0.1128	0.1175	0.1453	0.1623	0.1121	0.0042

TABLE 4.1: Matching results using proposed approach. Each database object is matched against all the other objects in the database. Each cell shows the dissimilarity measure between two objects selected from the database. The smallest value corresponds to the correct match.

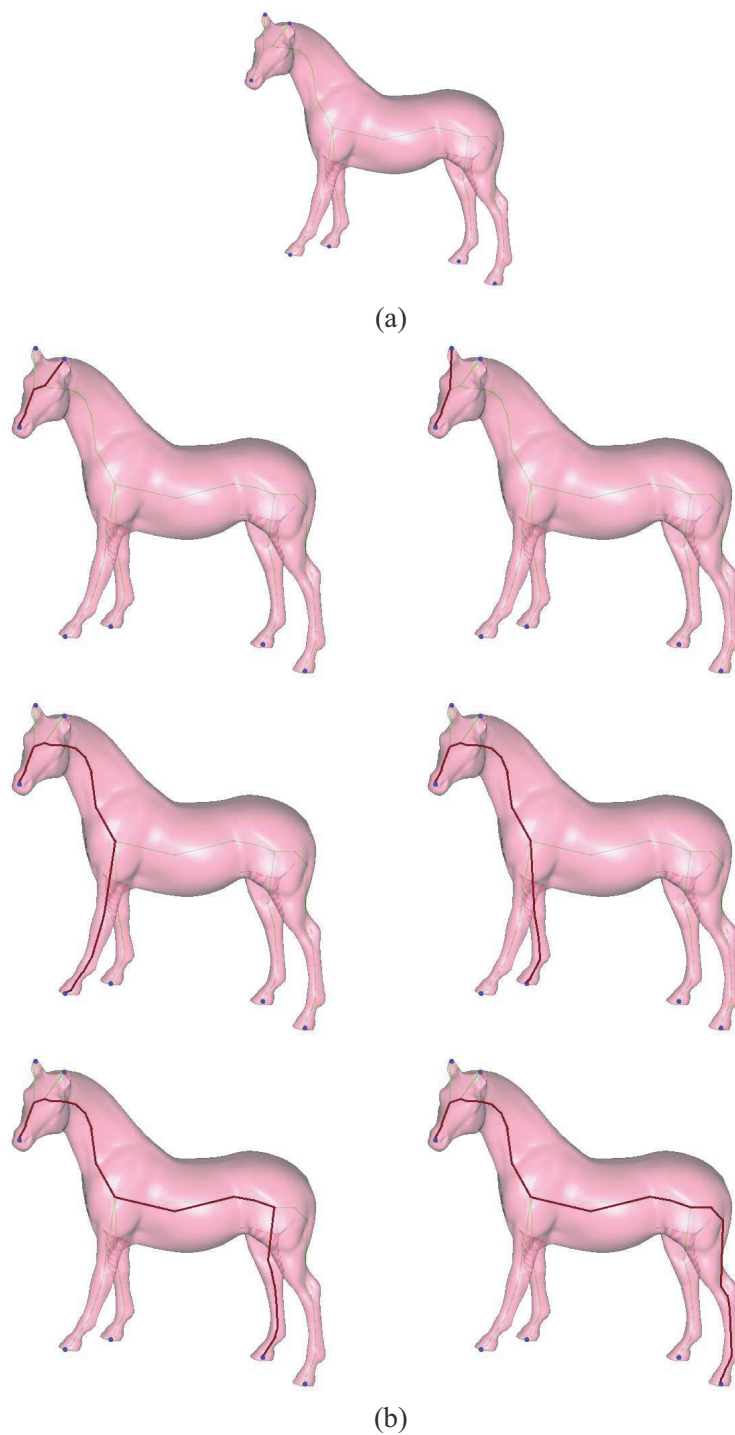


FIGURE 4.7: (a) Horse's Reeb graph. (b) Shortest paths between pairs of endpoints on the spectral skeleton.

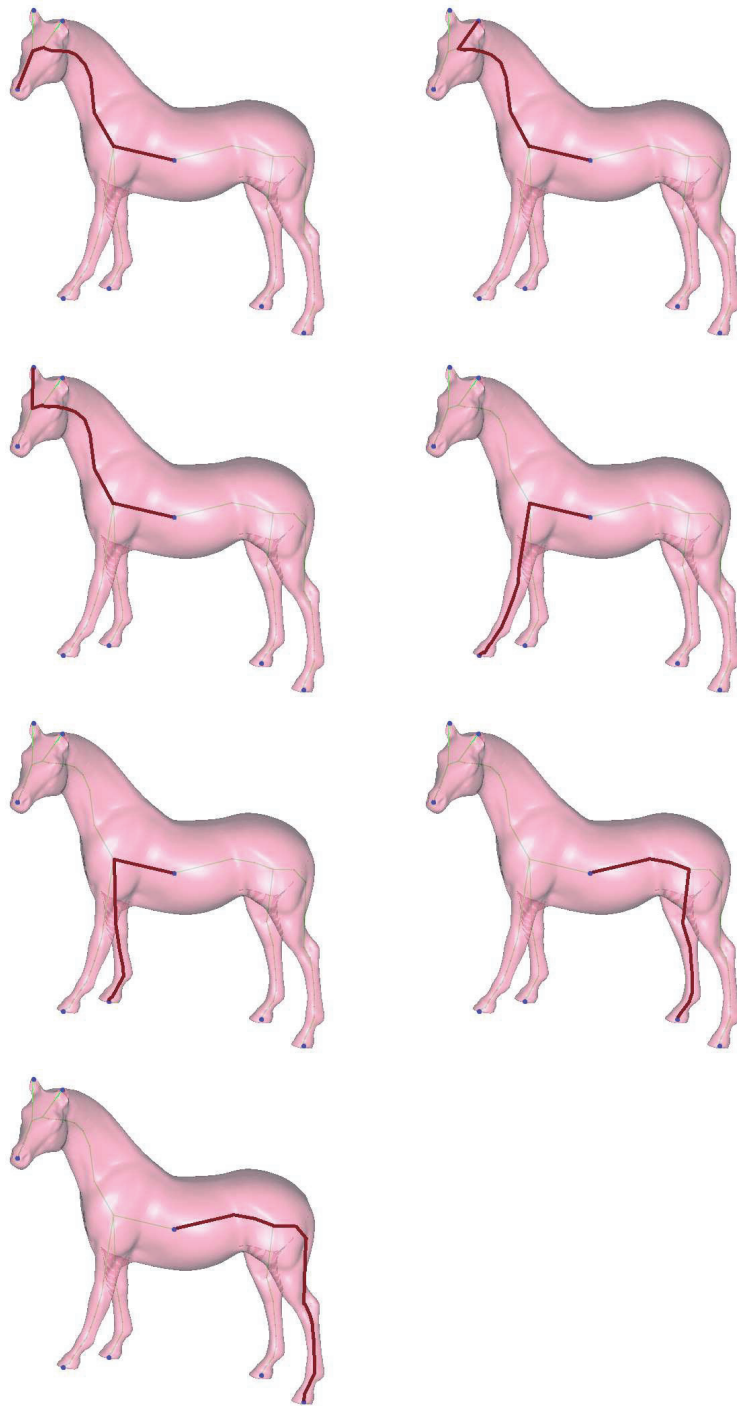


FIGURE 4.8: Shortest paths between the mesh centroid and an endpoint on the spectral skeleton.

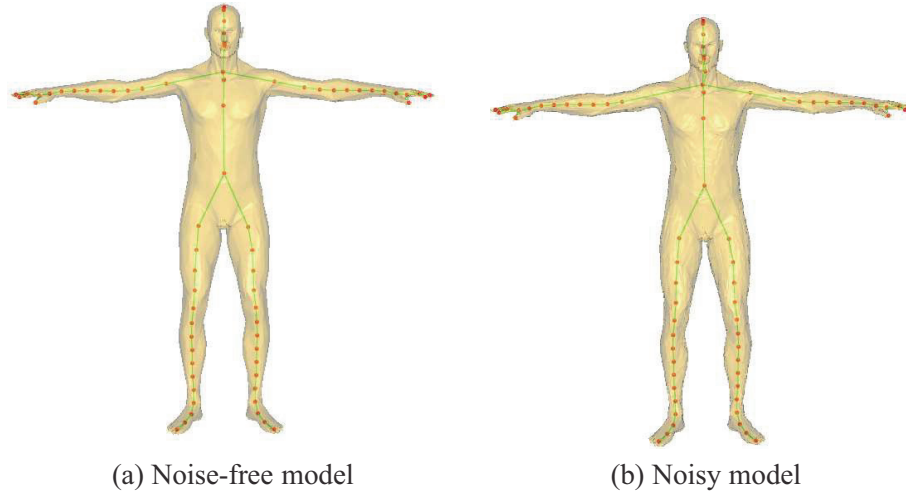


FIGURE 4.9: Robustness of spectral Reeb graph to noise.

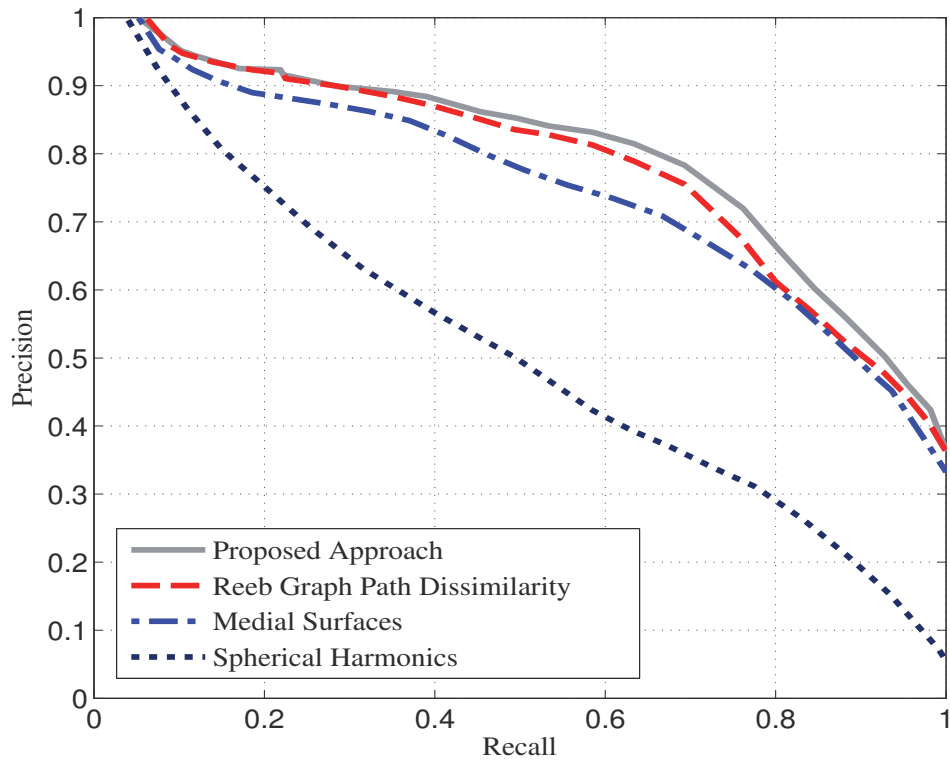


FIGURE 4.10: Precision vs. Recall curves for Reeb graph path dissimilarity, spherical harmonics, medial surfaces, Reeb graph path dissimilarity, and proposed approach using the McGill Shape Benchmark [71].

Query								
								
Retrieved Objects								
SRG	RGPD	SH	SRG	RGPD	SH	SRG	RGPD	SH
								
								
								
								
								
								
								
								
								
								

TABLE 4.2: Retrieval results using the McGill Shape Benchmark. The query shapes are shown in the second row. The top ten retrieved objects (top-to-bottom) using spherical harmonics (SH), Reeb graph path dissimilarity (RGPD), and our proposed approach (SRG) are shown in rows 5 to 14.

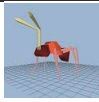
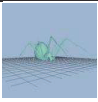
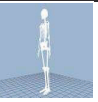
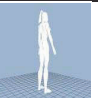
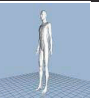
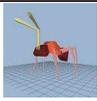
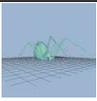
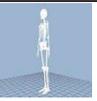
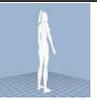
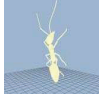
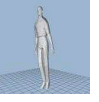
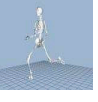
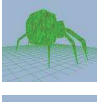
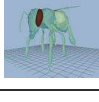
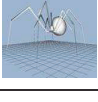
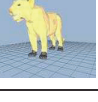
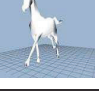
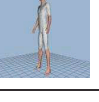
Query						
						
Retrieved Objects						
						
						
						
						
						
						

TABLE 4.3: Retrieval results using Princeton 3D dataset Benchmark. The query shapes are shown in the second row. The top five retrieved objects (top-to-bottom) of our proposed approach (SRG).

CONCLUSIONS AND FUTURE WORK

This chapter briefly concludes the thesis and highlights the major contributions of this research.

This thesis presented a medical image registration technique in the information-theoretic setting, a distance-based 3D object recognition approach in the Morse-theoretic framework, and a spectral 3D object recognition method using the Laplace-Beltrami operator. We have demonstrated the effectiveness of the proposed methods through numerical experiments on a variety of medical images and 3D benchmarks.

In the next section, the contributions made in each of the previous chapters and the concluding results drawn from the associated research work are presented. Suggestions for future research directions related to this thesis are provided in Section 5.2.

5.1 THESIS CONTRIBUTIONS

5.1.1 IMAGE REGISTRATION USING STOCHASTIC OPTIMIZATION

In Chapter 2, we proposed an entropic image alignment method by optimizing a generalized divergence measure using a modified simultaneous perturbation stochastic approximation algorithm. The registration is achieved by finding the optimal Euclidean transformation parameters that maximize the Jensen-Tsallis divergence. The main advantages of the proposed approach are: (i) Jensen-Tsallis divergence is symmetric, convex, theoretically upper-bounded, and quantifies efficiently the statistical dissimilarity between the reference image and the transformed target image, and (ii) the experimental results provide accurate registration results in comparison with existing techniques.

5.1.2 REEB GRAPH PATH DISSIMILARITY FOR 3D OBJECT MATCHING AND RETRIEVAL

In Chapter 3, we presented a normalized mixture distance function-based approach to topological modeling of 3D objects in the Morse-theoretic framework. The proposed algorithm preserves well the topology of 3D shapes, and it is robust, accurate, and has a low computational complexity. The main attractive properties of the proposed approach are: invariance to rotation, translation, and scaling; and robustness to noise and mesh decimation. The experimental results on 3D shape benchmark databases indicate the feasibility of the proposed approach and a much better performance compared to spherical harmonics and medial surfaces.

5.1.3 SPECTRAL SKELETON FOR 3D OBJECT MATCHING AND RETRIEVAL

In Chapter 4, we proposed the use of shortest path distance matching algorithm of the shape skeletons constructed from the second eigenfunction of the Laplace-Beltrami operator. The better performance of proposed algorithm was demonstrated on McGill's articulated shape database compared to spherical harmonics, medial surfaces, and Reeb graph path dissimilarity. We also tested the algorithm on Princeton's shape dataset and we showed that the proposed approach gives also satisfactory results for non-articulated shape models.

5.2 FUTURE RESEARCH DIRECTIONS

Several interesting research directions motivated by this thesis are discussed next. In addition to focusing on further improving the results of Reeb graph-based approaches by appropriately choosing more discriminatory endpoint features, we also intend to accomplish the following projects in the near future:

5.2.1 3D PARTIAL SHAPE MATCHING

Our ongoing efforts are focused on exploring the use of the Reeb graph path dissimilarity for 3D partial shape matching. Also, theoretically we hope to develop more rigorous way of finding the optimal resolution parameter of the skeletonization algorithm.

5.2.2 STOCHASTIC ANALYSIS OF LAPLACE-BELTRAMI SPECTRA

Another possible future work direction is the stochastic analysis of the second eigenfunction of Laplace-Beltrami operator and its application to 3D object matching and retrieval. Also, it would be of interest to

incorporate topology into the proposed methodology through Morse singularities of the second eigenfunction of the Laplace-Beltrami operator.

5.2.3 IMAGE REGISTRATION USING PRIORS

Another future work direction is to incorporate prior information on the joint intensity histogram between the images being registered for a more robust image alignment.

REFERENCES

- [1] I. Bankman, *Handbook of Medical Image Processing and Analysis*, Academic Press, 2008.
- [2] J.V. Hajnal, D.L.G. Hill, D.J. Hawkes, *Medical Image Registration*, CRC Press, 2001.
- [3] A.A. Goshtasby, *2-D and 3-D Image Registration for Medical, Remote Sensing, and Industrial Applications*, Wiley Publishers, 2005.
- [4] V. Guillemin and A. Pollack, *Differential topology*, Prentice-Hall, Englewood Cliffs, New Jersey 1974.
- [5] M. do Carmo, *Differential geometry of curves and surfaces*, Prentice-Hall, New Jersey, 1976.
- [6] J. Milnor, *Morse theory*, Princeton University Press, New Jersey, 1963.
- [7] A.T. Fomenko and T.L. Kunii, *Topological modeling for visualization*, Springer-Verlag Tokyo, 1997.
- [8] P. Viola and W.M. Wells, "Alignment by maximization of mutual information," *International Journal of Computer Vision*, vol. 24, no. 2, pp. 173-154, 1997.
- [9] F. Maes, A. Collignon, D. Vandermeulen, G. Marchal, and P. Suetens, "Multimodality image registration by maximization of mutual information," *IEEE Trans. on Medical Imaging*, vol. 16, no. 2, pp. 187-198, 1997.
- [10] A.O. Hero, B. Ma, O. Michel, and J. Gorman, "Applications of entropic spanning graphs," *IEEE Signal Processing Magazine*, vol. 19, no. 5, pp. 85-95, 2002.
- [11] J.P.W. Pluim, J.B.A. Maintz, and M.A. Viergever, "f-information measures in medical image registration," *IEEE Trans. on Medical Imaging*, vol. 23, no. 12, pp. 1508-1516, 2004.
- [12] Y. He, A. Ben Hamza, and H. Krim, "A generalized divergence measure for robust image registration," *IEEE Trans. on Signal Processing*, vol. 51, no. 5, pp. 1211-1220, 2003.

- [13] D. Corici and J. Astola, "Segmentation of DNA into coding and noncoding regions based on recursive entropic segmentation and stop-codon statistics," *EURASIP Journal on Advances in Signal Processing*, vol. 1, pp. 81-91, 2004.
- [14] L.S. Hibbard, "Region segmentation using information divergence measures," *Medical Image Analysis*, vol. 8, no. 3, pp. 233-244, 2004.
- [15] M-C. Chiang, R.A. Dutton, K.M. Hayashi, O.L. Lopez, H.J. Aizenstein, A.W. Toga, J.T. Becker, and P.M. Thompson, "3D pattern of brain atrophy in HIV/AIDS visualized using tensor-based morphometry," *NeuroImage*, vol. 34, no. 1, pp. 44-60, 2007.
- [16] D. Karakos, S. Khudanpur, J. Eisner, and C. E. Priebe, "Iterative denoising using Jensen-Rényi divergences with an application to unsupervised document categorization," *Proc. IEEE International Conference on Acoustics, Speech and Signal Processing*, Honolulu, Hawaii, 2007.
- [17] C. Tsallis, "Possible generalization of Boltzmann-Gibbs statistics," *Journal of Statistical Physics*, vol. 52, pp. 479-487, 1988.
- [18] S. Martin, G. Morison, W. Nailon, and T. Durrani, "Fast and accurate image registration using Tsallis entropy and simultaneous perturbation stochastic approximation," *Electronic Letters*, vol. 40, no. 10, pp. 595-597, 2004.
- [19] M. Aguilera and A. Ben Hamza, "An information-theoretic approach to georegistration of digital elevation maps," *Proc. IEEE Conference on Computer and Robot Vision*, Quebec City, Canada, 2006.
- [20] J.C. Spall, "Multivariate stochastic approximation using a simultaneous perturbation gradient approximation," *IEEE Trans. on Automatic Control*, vol. 37, no. 3, pp. 332-341, 1992.
- [21] A. Rényi, *On measures of entropy and information*, Selected Papers of Alfréd Rényi, vol. 2, pp. 525-580, 1961.
- [22] M.E. Havrda and F. Charvát, "Quantification method of classification processes: concept of structural α -entropy," *Kybernetika*, vol. 3, pp. 30-35, 1967.
- [23] J. Burbea and C.R. Rao, "On the convexity of some divergence measures based on entropy functions," *IEEE Trans. on Information Theory*, vol. 28, no. 3, pp. 489-495, 1982.
- [24] J. Lin, "Divergence measures based on the Shannon entropy," *IEEE Trans. on Information Theory*, vol. 37, no. 1, pp. 145-151, 1991.
- [25] A.W. Marshall and I. Olkin, *Inequalities: Theory of Majorization and Its Applications*, Academic Press, 1979.
- [26] J.C. Spall, "Implementation of the simultaneous perturbation algorithm for stochastic optimization," *IEEE Trans. on Aerospace and Electronic Systems*, vol. 34, no. 3, pp. 817-823, 1998.

- [27] T. Grigorishin, G. Abdel-Hamid, Y.H. Yang, "Skeletonization: an electrostatic field-based approach," *Pattern Analysis and Applications*, pp. 163-177, 1998.
- [28] K. Siddiqi, A. Shokoufandeh, S. J. Dickinson, and S.W. Zucker, "Shock graphs and shape matching," *Int. Jour. Computer Vision*, vol. 35, no. 1, pp. 13-32, 1999.
- [29] M. Hilaga, Y. Shinagawa, T. Komura, and T.L. Kunii, "Topology matching for fully automatic similarity estimation of 3D shapes," *Proc. SIGGRAPH*, pp. 203-212, 2001.
- [30] Y. Shinagawa, T.L. Kunii, and Y.L. Kergosien, "Surface coding based on Morse theory," *IEEE Computer Graphics and Applications*, vol. 11, no. 5, pp. 66-78, 1991.
- [31] F. Lazarus and A. Verroust, "Level set diagrams of polyhedral objects," *Proc. ACM Sympo. Solid Modeling and Applications*, pp. 130-140, 1999.
- [32] K. Siddiqi, J. Zhang, D. Macrini, A. Shokoufandeh, S. Bouix, and S. Dickinson, "Retrieving articulated 3-D models using medial surfaces," *Machine Vision and Applications*, vol. 19, no. 4, pp. 261-275, 2008.
- [33] J. Damon, "Tree structure for contractible regions in \mathbb{R}^3 ," *Int. Jour. Computer Vision*, vol. 74, no. 2, pp. 103-116, 2007.
- [34] K. Siddiqi and S. Pizer, *Medial Representations: Mathematics, Algorithms and Applications*, Springer, Heidelberg, 2008.
- [35] N.D. Cornea, M.F. Demirci, D. Silver, A. Shokoufandeh, S. Dickinson, and P.B. Kantor, "3D object retrieval using many-to-many matching of curve skeletons," *Proc. Int. Conf. Shape Modeling and Applications*, pp. 368-373, 2005.
- [36] M.S. Hassouna and A.A. Farag, "Variational curve skeletons using gradient vector flow," *IEEE Trans. Pattern Analysis and Machine Intelligence*, vol. 31, no. 12, pp. 2257-2274, 2009.
- [37] A. Tagliasacchi, H. Zhang, and D. Cohen-Or, "Curve skeleton extraction from incomplete point cloud," *ACM Trans. Graphics*, vol. 28, no. 3, 2009.
- [38] M. Ankerst, G. Kastenmüller, H. Kriegel, and T. Seidl, "3D shape histograms for similarity search and classification in spatial databases," *Proc. Int. Sympo. Advances in Spatial Databases*, pp. 207-226, 1999.
- [39] R. Osada, T. Funkhouser, B. Chazelle, and D. Dobkin, "Shape distributions," *ACM Trans. Graphics*, vol. 21, no. 4, pp. 807-832, 2002.
- [40] M. Kazhdan, T. Funkhouser, and S. Rusinkiewicz, "Rotation invariant spherical harmonic representation of 3D shape descriptors," *Proc. ACM Sympo. Geometry Processing*, pp. 156-164, 2003.

- [41] D-Y. Chen, X-P. Tian, Y-T. Shen, M. Ouhyoung, "On visual similarity based 3D model retrieval," *Computer Graphics Forum*, vol. 22, no. 3, pp. 223-232, 2003.
- [42] P. Shilane, P. Min, M. Kazhdan, and T. Funkhouser, "The princeton shape benchmark," *Proc. Shape Modeling International*, pp. 167-178, 2004.
- [43] J. Tierny, J-P. Vandeborre, and M. Daoudi, "Partial 3D shape retrieval by Reeb pattern unfolding," *Computer Graphics Forum*, vol. 28, no. 1, pp. 41-55, 2008.
- [44] K. Gebal, A. Baerentzen, H. Aans, and R. Larsen, "Shape analysis using the auto diffusion function," *Computer Graphics Forum*, vol. 28, no. 5, pp. 1405-1413, 2009.
- [45] D. Aouada and H. Krim, "Squigraphs for fine and compact modeling of 3-D shapes," *IEEE Trans. Image Processing*, vol. 19, no. 2, pp. 306-321, 2010.
- [46] S. Biasotti, D. Giorgi, M. Spagnuolo, and B. Falcidieno, "Reeb graphs for shape analysis and applications," *Theoretical Computer Science*, vol. 392, no. 1-3, pp. 5-22, 2007.
- [47] V. Pascucci, G. Scorzelli, P.T. Bremer, and Ajith Mascarenhas, "Robust on-line computation of Reeb graphs: simplicity and speed," *ACM Trans. Graphics*, vol. 26, no. 3, 2007.
- [48] G. Patane, M. Spagnuolo, and B. Falcidieno, "A minimal contouring approach to the computation of the Reeb Graph," *IEEE Trans. on Visualization and Computer Graphics*, vol 15, no. 4, pp. 583-595, 2009.
- [49] M. Reuter, "Hierarchical shape segmentation and registration via topological features of Laplace-Beltrami eigenfunctions," *Int. Jour. Computer Vision*, vol. 89, no. 2, pp. 287-308, 2010.
- [50] X. Ni, M. Garland, and J.C. Hart, "Fair morse functions for extracting the topological structure of a surface mesh," *Proc. Int. Conf. Computer Graphics and Interactive Techniques*, pp. 613-622, 2004.
- [51] H. Edelsbrunner, J. Harer, and A. Zomorodian, "Hierarchical Morse complexes for piecewise linear 2-manifolds," *Proc. Sympo. Computational geometry*, pp. 70-79, 2001.
- [52] G.M. Nielson and T.A. Foley, "A survey of applications of an affine invariant norm," *Mathematical Methods in Computer Aided Geometric Design*, Academic Press, Boston, pp. 445-467, 1989.
- [53] M.F. Demirci, A. Shokoufandeh, Y. Keselman, L. Bretzner, and S. Dickinson, "Object recognition as many-to-many feature matching," *Int. Jour. Computer Vision*, vol. 69, no. 2, pp. 203-222, 2006.
- [54] H. Ling and D.W. Jacobs, "Shape classification using inner-distance," *IEEE Trans. Pattern Analysis and Machine Intelligence*, vol. 29, no. 2, pp. 286-299, 2007.

- [55] X. Bai and L.J. Latecki, "Path similarity skeleton graph matching," *IEEE Trans. Pattern Analysis and Machine Intelligence*, vol. 30, no. 7, pp. 1282-1292, 2008.
- [56] X. Bai, L.J. Latecki, and W.-Y. Liu, "Skeleton pruning by contour partitioning with discrete curve evolution," *IEEE Trans. Pattern Analysis and Machine Intelligence*, vol. 29, no. 3, pp. 449-462, 2007.
- [57] P. Min, M. Kazhdan, and T. Funkhouser, "SA comparison of text and shape matching for retrieval of online 3D models," *Proc. ECDL*, pp. 209-220, 2004.
- [58] A. Ben Hamza and H. Krim, "Geodesic matching of triangulated surfaces," *IEEE Trans. Image Processing*, vol. 15, no. 8, pp. 2249-2258, 2006.
- [59] A. Ion, N.M. Artner, G. Peyré, W.G. Kropatsch, L.D. Cohen, "Matching 2D and 3D articulated shapes using the eccentricity transform," *Computer Vision and Image Understanding*, vol. 115, pp. 817-834, 2011.
- [60] X. Ni, M. Garland, and J.C. Hart, "Fair morse functions for extracting the topological structure of a surface mesh," *Proc. Int. Conf. Computer Graphics and Interactive Techniques*, pp. 613-622, 2004.
- [61] J. Tierny, J-P. Vandeborre, and M. Daoudi, "Partial 3D shape retrieval by Reeb pattern unfolding," *Computer Graphics Forum*, vol. 28, no. 1, pp. 41-55, 2008.
- [62] M. Belkin, P. Niyogi, and V. Sindhvani, "Manifold regularization: a geometric framework for learning from labeled and unlabeled examples," *Journal of Machine Learning Research*, vol. 7, pp. 2399-2434, 2006.
- [63] B. Lévy, "Laplace-Beltrami eigenfunctions: Towards an algorithm that "understands" geometry," *Proc. Conf. Shape Modeling and Applications*, 2006.
- [64] M. Reuter, "Hierarchical shape segmentation and registration via topological features of Laplace-Beltrami eigenfunctions," *Int. Jour. Computer Vision*, vol. 89, no. 2, pp. 287-308, 2010.
- [65] A.M. Bronstein, M.M. Bronstein, L.J. Guibas, and M. Ovsjanikov, "Shape Google: Geometric words and expressions for invariant shape retrieval," *ACM Trans. Graphics*, vol. 30, no. 1, 2011.
- [66] R.M. Rustamov, "Interpolated eigenfunctions for volumetric shape processing," *The Visual Computer*, vol. 27, pp. 951-961, 2011.
- [67] Y. Shi, R. Lai, S. Krishna, N. Sicotte, I. Dinov, A.W. Toga, "Anisotropic Laplace-Beltrami eigenmaps: Bridging Reeb graphs and skeletons," *Proc. CVPR Workshops*, pp. 23-28, 2008.
- [68] M.K. Chung and J. Taylor, "Diffusion smoothing on brain surface via finite element method," *Proc. IEEE Int. Sympo. Biomedical Imaging: Nano to Macro*, pp. 432-435, 2004.

- [69] A. Qiu, D. Bitouk, and M.I. Miller, "Smooth functional and structural maps on the neocortex via orthonormal Bases of the LaplaceBeltrami operator," *IEEE Trans. Medical Imaging*, vol. 25, no. 10, pp. 1296-1306, 2006.
- [70] K. Uhlenbeck, "Generic properties of eigenfunctions," *American Journal of Mathematics*, vol. 98, no. 4, pp. 1059-1078, 1976.
- [71] [Online]. <http://www.cim.McGill.ca/shape/benchmark>
- [72] [Online]: <http://shape.cs.princeton.edu/benchmark>
- [73] W. Mohamed, Y. Zhang, A. Ben Hamza, N. Bouguila, "Stochastic optimization approach for entropic image alignment," *Proc. IEEE Int. Symp. Information Theory*, Toronto, Canada, 2008.
- [74] W. Mohamed, A. Ben Hamza, "Nonextensive entropic image registration," *Proc. Int. Conf. Image Analysis and Recognition – Lecture Notes in Computer Science*, vol. 5627, pp. 116-125, 2009.
- [75] W. Mohamed, A. Ben Hamza, "Medical image registration using stochastic optimization," *Optics and Lasers in Engineering*, Elsevier Journal, vol. 48, no. 12, pp. 1213-1223, 2010.
- [76] W. Mohamed, A. Ben Hamza, "Stochastic approximation approach to image registration," *International Journal of Mathematics and Statistics*, vol. 7, no. 10, pp. 32-39, 2010.
- [77] W. Mohamed, A. Ben Hamza, "Retrieving articulated 3D objects using normalized distance function," *Proc. Conf. Articulated Motion and Deformable Objects – Lecture Notes in Computer Science*, vol. 6169, pp. 21-30, 2010.
- [78] W. Mohamed, A. Ben Hamza, K. Gharaibeh, "Graph-theoretic image alignment using topological features," *Proc. Int. Symp. Computational Modeling of Objects Presented in Images – Lecture Notes in Computer Science*, vol. 6026, pp. 199-209, 2010.
- [79] W. Mohamed and A. Ben Hamza, "Skeleton graph matching and retrieval of 3D objects," *Computer Graphics International*, Ottawa, 2011.
- [80] W. Mohamed and A. Ben Hamza, "Reeb graph path dissimilarity for 3D object matching and retrieval," *The Visual Computer*, vol. 28, no. 3, pp. 305-318, 2012.